STRUCTURE AND PROPERTY CALCULATIONS OF AMORPHOUS CERAMICS AND GLASSES USING DENSITY FUNCTIONAL THEORY CALCULATIONS AND EMPIRICAL POTENTIAL MOLECULAR DYNAMIC SIMULATIONS

by

Atreyi Dasmahapatra

DISSERTATION

Submitted in partial fulfillment of the requirements for the degree of Doctor of Philosophy at The University of Texas at Arlington

December, 2017

Arlington, Texas

Supervising Committee:

Peter Kroll, Supervising Professor

Brad Pierce

Kevin Schug

Kwangho Nam

Efstathios Meletis

Acknowledgements

Rome was not built in a single day. Neither is this work in my Ph.D. thesis. I deeply acknowledge the contributions of the following people – both in my professional and personal life who have helped me achieve this goal.

First and foremost, I am indebted to my advisor Dr. Peter Kroll. He mentored me, funded my research and instilled in me the necessary skills to be an independent researcher. I will forever be grateful to him for teaching me the habit of meticulous documentation my work, which time and again, has saved me from many catastrophes.

Next I would like to thank my committee members - Dr. Brad Pierce, Dr. Kevin Schug and Dr. E. Meletis for being accommodating. I am also grateful to Dr. Nam for agreeing to be a part of my committee at such a short notice. A special thank you to Dr. Dasgupta for being a part of my proposal defense and update committee and for providing constructive criticism about my work.

I am also lucky to have so many amazing colleagues at work – those who have graduated – Munuve Mwania and John Paul Nimmo II and those still continuing on – Susana Aguirre-Medel, Ilia Ponomarev, Poroshat Taheri and Shariq Haseen. I am thankful for your support and friendship in the past few years. My thoughts reach out to Gregory Monson with whom I shared a valuable friendship. A heartfelt thanks is due to Apparao Bokka for always being there in time of need. Lastly, I am greatly obliged to Michael Wey. For countless discussions and memorable coffee breaks, I thank you Michael, for making graduate school fun.

Thank you to the chemistry department support staff – Jill Howard and Debbie Cooke for always being kind and accommodating for various office works. I thank you Dr. W. Cleaver for making teaching duties fun.

The last section of my acknowledgements goes out to personal relationships. Thank you Arindam Das for teaching me how to code in Python, C++ and whatever *language* I demanded to know. I also appreciate the efforts you took to read my scientific manuscripts and providing

valuable comments. Above all, I thank my parents and didibhai (elder sister) for believing in me. Without your love and support I would not be here today.

LIST OF FIGURES

Introduction

Chapter 1

Appendix 1

Chapter 2

Appendix 2

Chapter 3:

Chapter 3: Summary:

Chapter 4

LIST OF TABLES

Chapter 1:

Appendix 1:

Chapter 2:

Appendix 2:

Chapter 3:

Appendix 3

Chapter 4:

Chapter 5

Appendix 5

LIST OF ABBREVIATIONS

Glas Transition temperature ..... T_g

Density Functional theory ..... DFT

Molecular Dynamics ..... MD

Central Processing Unit ..... CPU

Local Density Approximation ..... LDA

Generalized Gradient Approximation ..... GGA

Ultra High Temperature Ceramics ..... UHTCs

ab inito Molecular Dynamics ..... aiMD

Vienna Ab Initio Simulation Package ..... VASP

Projector Augmented Wave ..... PAW

Density Functional Perturbation Theory ..... DFPT

Enthalpy of mixing ..... ΔH_{mix}

Entropy of mixing ..... ΔS_{mix}

Phonon Density of States ..... phDOS, DOS

Partial Phonon Density of States ..... PDOS

Infra Red ..... IR

Heat Capacity at Constant Volume Cv

Difference between normalized PhDOS(ν) ..... dDOS(ν)

Integration of dDOS(ν) ..... IdDOS(ν)

Equation of State ..... EOS

Giga Pascal ..... GPa

Voigt-Reuss-Hill ..... V-R-H

Continuous Random Network ..... CRN

Large-scale Atomic/Molecular Massively Parallel Simulator ..... LAMMPS

General Utility Lattice Program ..... GULP

Pair-Correlation functions ..... PCFs

Radial Distribution function ..... RDF

under-coordinated ..... UC

Over-coordinated ..... OC

defective sphalerite ..... dsph

Heat Current auto-correlation Function ..... HCACF

Amorphous silicon boron nitride ..... a-SiBN

Green-Kubo ..... G-K

Marian Gastriech two-body MG2

Marian Gastrich 3 body MG3

Brito-Mota ..... BM

Matsunaga ..... mat

TABLE OF CONTENTS

Introduction:

Discovery of new materials has always been a precursor to progress throughout history. Various era in human evolution are marked by metals, e.g. the Copper age (4200 BCE), Bronze age (2300 – 700 BCE), the Iron age (1500 BCE) etc. Besides this, ceramic engineering in the form of pottery and glass manufacturing forms the oldest industry known to mankind. Excavations from the Indus valley civilization (3300 – 1300 BCE) sites have revealed distinctive examples of pottery and tiles. The concept of glasses was known to ancient Egyptians in 8000 BCE who used soda-lime glass to glaze their pottery. Ceramics are deeply ingrained in our modern life as well. Silica (SiO_2) glass windows in our homes, ceramic engine parts (Si_3N_4) in automobiles, micro-electronics such as integrated circuits in computers, silica (SiO_2) fibre optics in telecommunications or ceramic orthopaedic prostheses for biomedical applications – the ceramic materials are ubiquitous.

Ceramics are broadly defined as inorganic, non-metallic materials with ionic or covalent bonds. [1] They can be crystalline – where the atoms are ordered and the unit cell (primary building block) repeats periodically in all dimensions; or amorphous – where the atoms are placed randomly in a non-periodic manner. Glasses form a special case of amorphous material that have a *glass-transition temperature* (T_g). The glass-liquid transition temperature (T_g) (or simply glass transition temperature) is the temperature at which a material changes from the liquid phase into the *glassy* phase. (See Figure 1) In the glassy phase, the viscosity is so great that it does not allow for the diffusion of atoms/molecules. Unlike the transition of liquid to solid, transition of a liquid to a glass is not associated with a drastic change in volume, energy or viscosity. This indicates a second order transition. This glassy state, is notably, much more brittle compared to a crystalline solid. Definitions of T_g based on thermodynamic properties are arbitrary and not consolidated. In particular, heat capacity and thermal expansion most commonly used to determine T_g as both properties show drastic changes at the glass transition temperature.

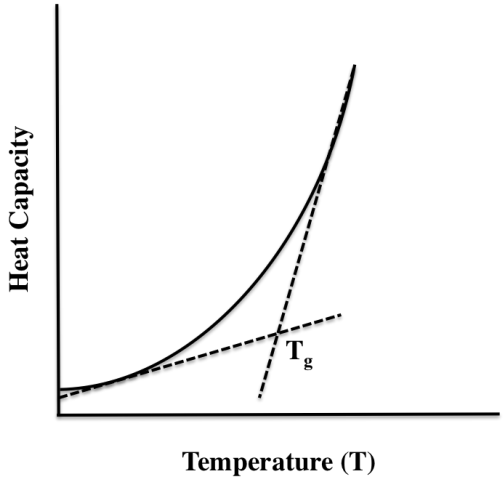

Figure 1: Schematic diagram illustrating glass transition temperature for an amorphous solid

Computational modeling of amorphous ceramics and glasses is relatively a new field of research. Before the advent of computers the only way to predict properties of a system was to build mechanical models using ball-bearings. The use of computer simulations as an *exploratory* tool was first applied to dense liquids. The first reported simulation of *real* material was published in 1960. [2] Few years later, the first data for liquid Argon was published that used a simple two-body Lennard-Jones potential to describe the interaction between atoms. [3] Since the last 60 years, computers have undergone a vast change in processing power– from 100 mega flops per processor in the 1960s to 93 peta flops per second in 2017. [4] Computational simulations now range from approximate methods like molecular dynamics (MD) that depend on Newtonian mechanics to accurate methods like Density Functional Theory (DFT) that is based on quantum mechanics.

Molecular dynamics simulations involve the numerical solution of the classical equations of motion. [5] The basic algorithm is outlined in Figure 2. An empirical potential descibes the inter-atomic interaction. The total time of simulation is divided into many small discrete time-steps (typically 10^{-12} or 10^{-15} s). At each time-step, forces are computed and atom positions updated based on Newton's laws of motion. With parallization across multiple CPU's, MD calculations are fast and enables us to compute properties of a system consisting of a few thousand atoms

easily. However, force fields or empirical potentials implemented in MD simulations are inherently approximations and thus needs to be used with caution.

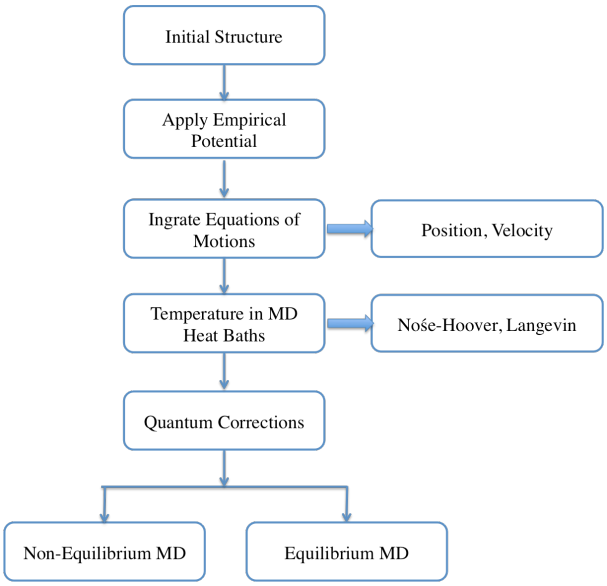

Figure 2: Flow-chart of a Molecular Dynamics simulation

Density functional theory (DFT) is based on Hohenburg-Kohn theorem that states that the total ground state energy, E, of a system is a functional of it's electron density, ρ. [6] However, this ground state energy E[ρ], includes a term for electron exchange and correlation – E_{XC}, that is realized via many approximations. One such example is the Local Density Approximation (LDA) that assumes that E_{XC} density at every position in space for the molecule is the same as it would be for the homogeneous electron gas (HEG) having the same density as found at that position. DFT is undoubtedly one of the most promising and accurate approaches to compute the electronic structure of matter. Yet DFT has it's limitations: 1) Approximation of E_{XC} 2) works best for systems consisting of < 1000 atoms within realistic time scales and 3) fails for strongly correlated systems. [7, 8]

The work in this thesis involves modeling amorphous ceramics and glasses using the tools of DFT and classical MD. Systems investigated include: metal-silicate glasses (in particular HfO_2-SiO_2), composite coatings (comprising of Zr-Si-B-C-N), and the refractory materials amorphous silicon nitride (a-Si_3N_4) and amorphous silicon boron nitride (a-SiBN). Modeling techniques

include traditional "melt-and-quench" simulations combined with simulated annealing. Structures are further investigated for their physical and chemical properties. A brief overview of each chapter is given below:

Hafnia-silica glasses (HfO_2-SiO_2) find applications in microelectronics and optical waveguides. I did a computational study of the thermochemistry of these compounds exploring enthalpy of mixing and solubility. Additional analysis of vibrational modes in mixed glasses highlighted that adding a heavy Hafnium (Hf) atom will reduce thermal conductivity in these glasses. [9]

Zirconium borides, carbides, and nitrides are Ultra High Temperature Ceramics (UTHCs) and candidates for thermal protective coatings in hypersonic vehicles. At elevated temperatures these materials have poor oxidation resistance. Adding silicon nitride promoted formation of a protective silica glass layer upon oxidation. With this goal in mind, I modeled Zr-Si-B-C-N ceramics, mixtures of ZrB_2, ZrN, ZrC and Si_3N_4 with different composition and analyzed the impact of Si_3N_4 on their mechanical properties. [10] This project is a part of the "Materials Genome Initiative" which aims to accelerate advanced materials discovery. [11]

Amorphous silicon nitride (Si_3N_4) and silicon boron nitride (SiBN) ceramics exhibit outstanding thermal and mechanical properties and are used as high-temperature protective coatings in extreme environments. I provided a comparative study of empirical potentials for modeling Si_3N_4 and outlined quality – and failure – of seven different approaches. My study also highlights the capabilities of one "forgotten" potential, which should receive more credit in research. [12] For a-SiBN, I study the impact of composition, density and temperature on the thermal conductivity of the material. The dispersion of segregated boron nitride (BN) domains inside a-SiBN structure impact the thermal transport in these materials. [13, 14]

References

[1] R. Pampuch, Ceramic materials: an introduction to their properties, Elsevier Scientific Pub. Co.1976.

[2] N. Metropolis, A.W. Rosenbluth, M.N. Rosenbluth, A.H. Teller, E. Teller, Equation of State Calculations by Fast Computing Machines, J Chem Phys 21(6) (1953) 1087-1092.

[3] A. Rahman, Correlations in the Motion of Atoms in Liquid Argon, Phys Rev 136(2A) (1964) A405-A411.

[4] <https://www.top500.org/project/linpack/>).

[5] D.C. Rapaport, The Art of Molecular Dynamics Simulation, Cambridge University Press2004.

[6] J.F. Stanton, A Chemist's Guide to Density Functional Theory By Wolfram Koch (German Chemical Society, Frankfurt am Main) and Max C. Holthausen (Humbolt University Berlin). Wiley-VCH: Weinheim. 2000. xiv + 294 pp. $79.95. ISBN 3-527-29918-1, Journal of the American Chemical Society 123(11) (2001) 2701-2701.

[7] A.J. Cohen, P. Mori-Sanchez, W.T. Yang, Insights into current limitations of density functional theory, Science 321(5890) (2008) 792-794.

[8] K. Burke, Perspective on density functional theory, J Chem Phys 136(15) (2012).

[9] A. Dasmahapatra, P. Kroll, Structure and thermodynamic properties of hafnia-silica glasses with low hafnia content, J Non-Cryst Solids 416 (2015) 14-20.

[10] A. Dasmahapatra, E. Meletis, P. Kroll, First principles modeling and simulation of Zr-Si-B-C-N ceramics: Developing hard and oxidation resistant coatings, Acta Mater 125 (2017) 246-254.

[11] J. Vickers, Materials Genome Initiative, (2015).

[12] A. Dasmahapatra, P. Kroll, Modeling amorphous Silicon Nitride: A comparative study of empirical potentials, Submitted to PRB (2017).

[13] J. Al-Ghalith, A. Dasmahapatra, P. Kroll, E. Meletis, T. Dumitrică, Compositional and Structural Atomistic Study of Amorphous Si–B–N Networks of Interest for High-Performance Coatings, The Journal of Physical Chemistry C 120(42) (2016) 24346-24353.
[14] A. Dasmahapatra, P. Kroll, Thermal Conductivity of Amorphous Silicon Boron Nitride: Studying Impact of Composition, Density, and Temperature using Density Functional Theory Calculations and Empirical Potential Molecular Dynamic Simulations In preparation (2017).

CHAPTER 1

STRUCTURE AND THERMODYNAMIC PROPERTIES OF HAFNIA-SILICA GLASSES WITH LOW HAFNIA CONTENT[1]

Scope and Motivation

[1] This chapter has been published in Journal of Non-Crystalline solids and is being used with the

Based on chemical composition, glasses are broadly classified as either oxide or non-oxide glasses. The most common and historically oldest example of oxide glasses are "silicate" glasses which are primarily composed of silica (SiO_2). Other examples are P_2O_5, GeO_2, B_2O_3 etc. Non-oxide glasses contain chalcogenide (e.g. As_2S_3), halide (e.g. ZrF_4-BaF_2-LaF_3-AlF_3) and metallic (e.g. $Cu_{50}Zr_{50}$) components instead of oxygen. Depending on microstructure, glasses are further classified as as network formers (e.g. SiO_2, B_2O_3), network modifiers (e.g. Na_2O, PbO) and intermediate network formers (e.g. Al_2O_3, TiO_2). Network former glasses such as SiO_2 are often "doped" with transition metal ions for improved functionality. [1] [2] [3]

HfO_2-SiO_2 glasses are an amorphous mixture of silica doped with small amounts (< 10 mol %) of hafnia. Hafnia-silica glasses are formed as a byproduct of oxidation of Ultra-High Temperature Ceramics (UHTCs) e.g. HfB_2. These glasses are generally synthesized via the sol-gel route or by various sputtering methods. [4] Hafnia-silica glasses have major applications in microelectronics and as planar waveguides. [5-7] Recently HfO_2-SiO_2 glasses were used as high refractive index coatings on multilayer mirrors in optical systems including LIGO, the Laser Interferometric Gravitational Wave Observatory. [8] In Chapter 1, I focus on modelling and property calculations of hafnia-silica glasses (HfO_2-SiO_2).

A systematic computational study was done on HfO_2-SiO_2 models with small amounts (3-10 mol %) of hafnia dissolved in silica. Small models of HfO_2-SiO_2 glass with 100 - 112 atoms are studied for their structure and thermochemistry. The focus of the study is to determine the impact of HfO_2 on the network structure of SiO_2. An appendix follows the peer-reviewed article where I include additional data concerning my study with hafnia-silica glass. The data was omitted from the publication as it appeared redundant, however it will be useful for future research in the study of Hafnia-Silica glass.

References:

[1] R.W. Cahn, P. Haasen, E.J. Kramer, J. Zarzycki, Mater. Sci. Tech., Glasses and Amorphous Materials, Wiley 1996.

[2] Glass and Glass-Ceramics, Ceramic Materials: Science and Engineering, Springer New York, 2007, pp. 379-399.

[3] S.D. Stookey, Explorations in Glass: An Autobiography, Wiley-Blackwell, 2000.

[4] C. Armellini, A. Chiappini, A. Chiasera, M. Ferrari, Y. Jestin, M. Mortier, E. Moser, R. Retoux, G.C. Righini, Rare earth-activated silica-based nanocomposites, J. Nanomater. 2007

[5] S. Berneschi, S. Soria, G.C. Righini, G. Alombert-Goget, A. Chiappini, A. Chiasera, Y. Jestin, M. Ferrari, S. Guddala, E. Moser, S.N.B. Bhaktha, B. Boulard, C.D. Arfuso, S. Turrell, Rare-earth-activated glass-ceramic waveguides, Opt. Mater. 32(12) (2010) 1644-1647.

[6] G.C. Righini, S. Berneschi, G.N. Conti, S. Pelli, E. Moser, R. Retoux, P. Feron, R.R. Goncalves, G. Speranza, Y. Jestin, M. Ferrari, A. Chiasera, A. Chiappini, C. Armellini, Er^{3+}-doped silica-hafnia films for optical waveguides and spherical resonators, J. Non-Cryst. Solids 355(37-42) (2009) 1853-1860.

[7] M. Ferrari, G.C. Righini, Glass-Ceramic Materials for Guided-Wave Optics, Int. J. Appl. Glass. Sci. 6(3) (2015) 240-248.

[8] M. Principe, Reflective coating optimization for interferometric detectors of gravitational waves, Opt. Express 23(9) (2015) 10938-10956.

Structure and Thermodynamic Properties of Hafnia-Silica Glasses with Low Hafnia Content

Atreyi Dasmahapatra and Peter Kroll*,

Department of Chemistry and Biochemistry, The University of Texas at Arlington,

700 Planetarium Place, Arlington, Texas 76019, United States.

Abstract

Using density functional calculations we study structural, elastic, vibrational and thermo-chemical properties of hafnia-silica glasses with low hafnia content (≤ 10 mol%). Melt-quench-generated models show a preference for Hf-O-Hf linkages and early formation of HfO_x-clusters. We compute an enthalpy of mixing of HfO_2 in SiO_2 of (0.8 ± 0.3) eV/HfO_2, and estimate a solubility of HfO_2 in SiO_2 of 1.9 [-0.3/+11.6] mol% at 1873 K. Elastic moduli of hafnia-silica glasses are comparable to those of pure silica for the range of compositions addressed here. Heat capacities of mixed glasses follow a simple rule of mixture. Addition of hafnia to silica glass shifts high-frequency modes to lower wave numbers. Our data suggests that Hf atoms and small HfO_x-clusters pin floppy modes in silica glass, visible in a depletion of low-frequency vibrational modes.

1. Introduction

Amorphous alloys of hafnia (HfO_2) and silica (SiO_2) find major applications in optical and microelectronic devices. For example, current demand for new high-k dielectric materials indicate hafnia-silica compounds as leading contenders.[1] Moreover, hafnia-silica glasses are used as planar waveguides with remarkable characteristics.[2] Not at least, hafnia-silica melts occur as oxidation product of hafnia-based ultra-high temperature ceramics (HfC, HfN, HfB_2).[3]

The solubility of hafnia in silica glass has been experimentally investigated more than 40 years ago. Ledneva et al. determined a limit of 3 mol% HfO_2 in SiO_2 at 1873 K.[4] It is possible to produce hafnia-silica compounds with even higher hafnia content, however, by a variety of non-equilibrium methods.[5-7] Goncalves et al. synthesized HfO_2-SiO_2 glasses with up to 30 mol% HfO_2 via the sol-gel route.[5] Neumayer et. al. prepared hafnia-silica films with 15-75 mol% hafnia by spin casting of chemical solutions.[6] These compounds are not necessarily thermodynamically stable, since they undergo phase separation in the amorphous state during annealing prior to crystallization [6]

A few computational studies addressed amorphous hafnia-silica compounds. Using first-principles methods Broqvist et al. studied the evolution of dielectric constants and band gaps in hafnia-silica mixtures.[8, 9] A brief study by Ikeda et. al proposes favorable mixing of amorphous hafnia and silica glass, with an onset of phase separation at 10 mol% HfO_2.[10] Scopel et al. modeled hafnia silica glass with hafnia content larger than 25 mol% using melt-quench techniques and studied structural imperfections and oxygen vacancies.[11] The impact of adding hafnia to silica in low concentrations, towards the dilute limit, remained unexplored.

In this work, we investigate HfO_2-SiO_2 glass with low hafnia content (2.8 – 10.0 mol%) using Density Functional Theory calculations. The paper is organized as follows: in the next section we present computational details for structure generation as well as property calculations of HfO_2-SiO_2 models. Thereafter, we present and discuss our results. We focus on the impact of the metal oxide on glass structure and thermochemistry, and investigate the change of vibrational

and elastic properties upon adding hafnia to silica. We also trace a depletion of low-frequency modes, which appears counterintuitive. Finally, we summarize our results and present our conclusions.

2. Computational Methods

Throughout this work, we perform Density Functional Theory [12] calculations as implemented in the Vienna Ab Initio Simulation Package (VASP).[13-15] We use the Projector Augmented Wave (PAW) [16, 17] method together with the Generalized Gradient Approximation (GGA) of electron exchange and correlation. For optimizations and property calculations we use a cutoff energy of 350 eV for the expansion of the wave function into a plane wave basis. The Brillouin zone was sampled at the Γ-point. We performed selected calculations using "harder" pseudopotentials and a higher cutoff energy (500 eV), but found no significant deviations from trends we report for structure and properties.

Models of HfO_2-SiO_2 glass are generated via ab inito molecular dynamics (aiMD) simulation under periodic boundary conditions using the "melt-quench" approach. In our procedure, an ensemble of atoms is placed into a cubic box of appropriate volume and heated at 5000 K, producing a melt-like structure. After 10 ps at 5000 K all memory of a pre-existing configuration is lost. Subsequently, the system is cooled to 3000 K within 20 ps (cooling rate of 10^{14} Ks^{-1}). At 3000 K we keep the temperature of the system constant for 20 ps. A second cooling step to 2000 K lasts 20 ps (cooling rate of $5 \cdot 10^{13}$ Ks^{-1}) and is followed by a second hold at 2000 K for another 20 ps. We finally quench the system to 300 K within 20 ps (cooling rate of $8.5 \cdot 10^{13}$ Ks^{-1}). To reduce the computational costs, the cutoff energy during aiMD simulations is reduced to 205 eV. We use a time-step of 2 fs for the integration of the equations of motions and adjust the temperature via velocity rescaling throughout the aiMD simulations.

The structure obtained after quenching to 300 K is finally optimized, allowing atomic positions and cell parameters to adjust to a local minimum energy state. Forces are converged to

$5 \cdot 10^{-3}$ eV/Å, which is necessary to avoid spurious negative frequencies in subsequent phonon calculations.

Second-order stiffness coefficients (elastic constants) c_{ij} are computed via the strain-stress relationship given by Hooke's Law. We estimate Bulk modulus B, Young's modulus E, shear modulus G, and Poisson's ratio σ, for each structure within the Reuss-Voigt-Hill approximations.[18-20] The bulk modulus B is confirmed by a Murnaghan fit to volume-energy data obtained from separate calculations.[21]

Vibrational frequencies, infrared (IR) spectra, and thermodynamic properties are computed within Density Functional Perturbation Theory (DFPT) in conjunction with the PHONOPY package.[22] Final spectra are obtained by convoluting the individual frequencies with a Gaussian function of width 50 cm^{-1}. Vibrational frequencies obtained via the finite displacement method agree within 1% with DFPT results. Thermodynamic properties are derived from phonon spectra using the harmonic approximation.[23] Infrared intensities of vibrational modes are calculated using Born effective charges employing the method published by Gianozzi and Baroni.[24]

3. Results and Discussions:

3.1. Structure

We chose mol-ratios HfO_2:SiO_2 of 1:36, 2:36, 3:36, and 4:36 to study the impact of adding small quantities of hafnia to silica glass. The mol ratios correspond to mol% HfO_2 of 2.7, 5.3, 7.7, and 10.0 in the hafnia-silica glass, respectively. The compositions reflect the addition of one or more units of HfO_2 into a system of 36 SiO_2 and facilitate analyzing the impact of mixing HfO_2 into SiO_2, e.g. to compute the enthalpy of mixing. For each composition of the mixed glasses we generated six models via independent melt-quench simulations and compare the results with models of vitreous silica (a-SiO_2, denoted 0:36; six models) and amorphous hafnia (a-HfO_2, one

model), which we created using the same approach. In addition, we computed crystalline structures of α-quartz (α-SiO_2) and monoclinic hafnia (m-HfO_2) for reference.

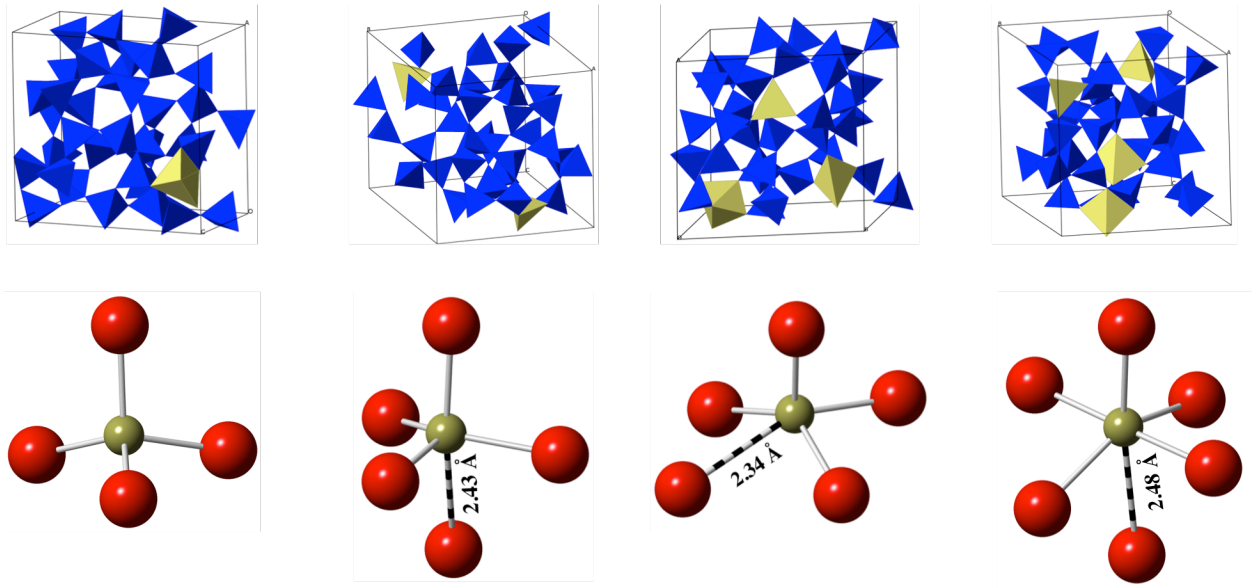

Figure 1: (Top) Representative models of mixed amorphous HfO_2-SiO_2 structures in a polyhedral view. Blue polyhedra represent SiO_4–units while yellow polyhedra represent HfO_n-environments (n = 4, 5, 6). From left to right the mol ratio of HfO_2 to SiO_2 is increasing from 1:36, 2:36, 3:36 to 4:36. (Bottom) Local environments of Hf in amorphous HfO_2-SiO_2 structures displaying different Hf coordination. The typical Hf-O bond length is 1.90-2.10 Å. Examples of extended Hf-O bonds (dashed) occuring in five and six-fold coordinated Hf are shown.

Representative structures for each composition are shown in Figure 1(top). We find – throughout our models – Si being four-fold, approximately tetrahedrally coordinated by O. None of the structures exhibit three-fold coordinated Si, and the distance from Si to a fifth O is always larger than 2.5 Å. The Si-O bonds form a network into which the Hf is embedded. Detailed looks into structures reveal local environments of Hf as shown in Figure 1 at the bottom.

Hf appears four- or five-fold coordinated, only three of 24 models contain a 6-fold coordinated Hf. With four O neighbors Hf adopts an approximately tetrahedral environment (Figure 1). Surrounded by five O, we find coordination environments close to square-pyramids

and trigonal bi-pyramids. Six-fold coordinated Hf is found only in three models of composition 4:36, approximately forming octahedra. For both 5- and 6-fold coordinated Hf we find large variations in bond lengths within the polyhedron. For example, all 5-coordinated Hf exhibit three or four "short" bonds (1.90-2.10 Å) and one or two longer bonds (2.20 - 2.49 Å). Thus, these coordination environments are better described as (4+1) or (3+2) coordination. Such elongated Hf-O bonds for higher coordinated Hf has been reported before.[8, 9] The bond length variation is also visible in the distance pair correlation function g(r) discussed further below. Taking the longer Hf-O bonds into account, the average coordination number (CN) of Hf in 1:36, 2:36, 3:46, and 4:36 models (averaged over Hf sites within the same model as well as over six models for each composition) is 4.6, 4.5, 4.5 and 4.8, respectively. Hence, the CN of Hf is approximately constant in models with low hafnia content. Previously, Broqvist et al. reported a correlation between hafnia content and average CN of Hf in $Hf_xSi_{1-x}O_2$ models (x = 0.3, 0.5, 1.0) with 30-%, 50-% and 100-% HfO_2 in SiO_2.[8, 9]

Nevertheless, the average CN of Hf in our amorphous models is significantly smaller than that in crystalline structures of $HfSiO_4$ (CN=6) and m-HfO_2 (CN=7). This relates, for instance, to the CN of Al in alumina and aluminosilicate glasses.[25-27] While Al adopts six-fold coordination in the crystal structure of corundum α-Al_2O_3, it appears 4-and 5- connected to oxygen in aluminosilicate glasses at ambient pressures.

Oxygen atoms appear two- or three-fold coordinated by cations, never four-fold. Three-fold coordinated O is, with one single exception, always bonded to 5- or 6-fold coordinated Hf. Looking at all 24 HfO_2-SiO_2 glass models, three-fold oxygen is found for 12.7% of O atoms. Neither Hf=O nor Si=O double bonds are present.

Simulated site-site distance pair correlation functions g(r) of two representative models of composition 1:36 and 4:36, respectively, are shown in Figure 2. Each g(r) shows two distinct peaks with maxima at 1.63 Å and at 1.93 Å. These are due to Si-O and Hf-O bonds, respectively. A third peak located at 2.63 Å results from O···O distances in SiO_4-tetrahedra. An O···O correlation originating from HfO_4-tetrahedra shows up at about 3.13 Å. A closer look at the Hf-O

partial pair correlation (Figure 2) shows strong asymmetry of the signal located at 1.93 Å, which tails off to longer distances. This reflects elongated Hf-O bonds in coordination environments highlighted in Figure 1 at the bottom. A tetrahedral environment HfO_4 exhibits Hf-O distances in the range 1.90 to 2.01 Å with the exception of three models which show a Hf-O bond > 2.01 Å. In a (4+1) five-fold coordination, four bonds occur in the range of 1.90 to 2.04 Å, while a fifth bond has a length between 2.20 and 2.49 Å. A (3+2) five fold coordinated hafnium atom shows short Hf-O bond distances between 1.92 and 2.01 Å and long bond distances between 2.08 and 2.43 Å. A six-fold coordination environment is less well defined, with Hf-O bonds as long as 2.50 Å.

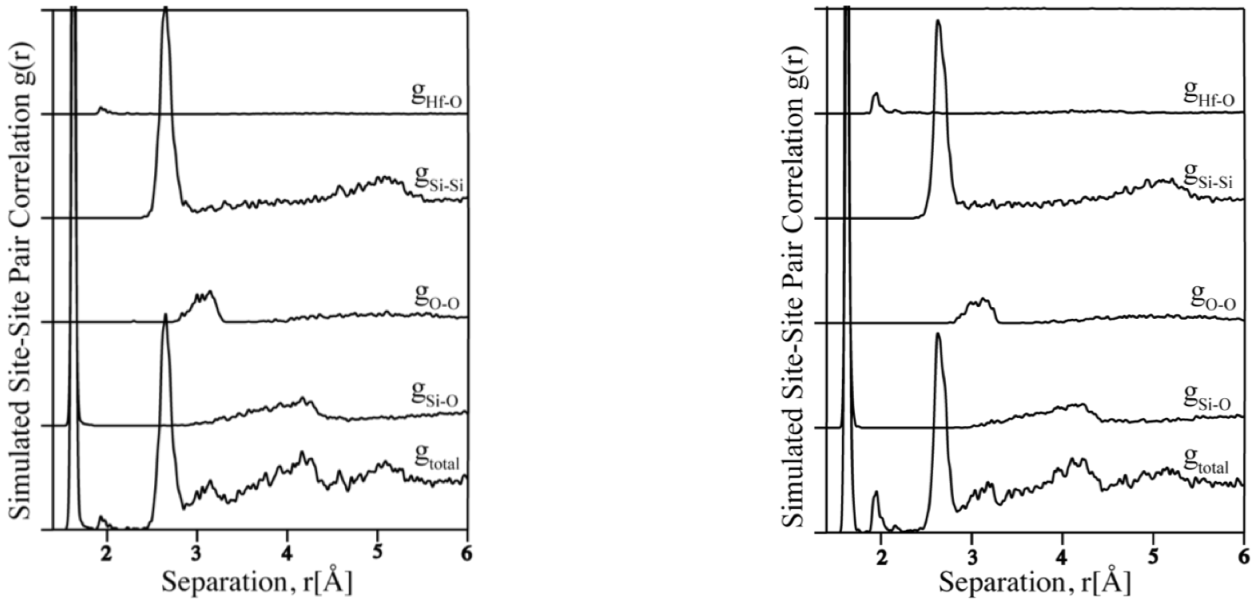

Figure 2: Simulated total and partial site−site pair correlation functions g(r) for representative models of compositions 1:36 (left) and 4:36 (right) HfO_2-SiO_2 glass. Individual entries are convoluted with a Gaussian with FWHM of 3 pm. The functions are drawn to scale and the difference between two ticks on the ordinate is 20. The total g(r) is normalized so that it approaches the value 10 at infinite distance. Its maximum value attained for the first Si-O distance peak is off scale, at 233 and at 213, for 1:36 and 4:36, respectively. Partial g(r)'s are normalized to 1 at infinite distance.

Returning a last time to the details of the atomistic structure, we focus on the presence of Hf-O-Hf linkages that appear in the models. We find no such linkage in any of the six 2:36 models, but

eight Hf-O-Si linkages in 3:36 models (average of 1.3 per model), and 13 linkages in 4:36 models (2.2 per model). Assuming a random network model of tetrahedrally coordinated Si and Hf (thus, neglecting that some Hf are 5- and 6-fold coordinated) the probability of Hf-O-Hf linkages can be computed using a combinatorial approach. The network is topologically equivalent to a 4-connected network (omitting the O atoms) and the probability to find Hf coordinated by (4-k) Hf atoms and k Si atoms (k = 0, 1, 2, 3, 4) is given by $P[Si_k Hf_{4-k}] = \frac{4!}{k!(4-k)!}(P_{Hf-O-Hf})^{4-k} \cdot (P_{Hf-O-Si})^k$, with $P_{Hf-O-Hf} = (P_{O-Hf})^2$ and $P_{Hf-O-Si} = 2 \cdot P_{O-Hf} \cdot P_{O-Si}$. The probabilities to find the bonds $P_{O\text{-}Si}$ and $P_{O\text{-}Hf}$ are set by the molar ratio of Hf and Si. This approach is valid for an infinitely large model, but does not take into account the finite size of models considered here. Such systems will show a higher probability of finding Hf-O-Hf linkages due to periodic boundary conditions. Therefore, we generated about 100,000 random network models with sizes matching those studied here under periodic boundary conditions using our previously published method.[28]

We find that for composition 4:36 the probability of finding a model without any Hf-O-Hf linkages is 57%. The average number of Hf-O-Hf linkages present in a single 4:36 model is 0.53. Hence, the expected total number of Hf-O-Hf linkages in six models with composition 4:36 is 3.2 — which considerably smaller than 13 linkages we count for the models we simulated. While these numbers hold for 4-fold coordinated Hf, modeling 4:36 networks with average coordination of 4.5 or 5 does not alter severly the findings. Therefore, our models exhibit agglomeration of Hf atoms forming Hf-O-Hf bonds and, ultimately, a tendency to form $(HfO)_x$-clusters at these concentrations. Indeed, Hf-O-Hf linkages always occur between 5- and 6-fold coordinated Hf, and we find no less than six instances of Hf with two Hf-O-Hf linkages simultaneously forming Hf-$(OHf)_2(OSi)_n$ (n=3,4) environments. These "clusters" affect vibrational properties of the models and induce non-linear trends, which will be discussed further below. More Hf-O-Hf linkages than expected are also found in 3:36 models, but only one model shows a "clustering" of these linkages. For 2:36 models the probability of finding a model

without Hf-O-Hf linkages is about 89%, and the expected total number of Hf-O-Hf linkages in six models with composition 2:36 is 0.7. Our 2:36 models, which do not exhibit any Hf-O-Hf linkage, may, therefore, still be random.

3.2. Thermochemistry

In Figure 3 (left) we plot the energy of pure silica and of mixed hafnia-silica models as a function of the number of HfO_2 units in the structure. Since the difference in composition between two models is a multiple of HfO_2, our approach allows a facile estimate of the enthalpy associated with incorporating hafnia into silica glass. We choose to plot the lowest energy model obtained for each composition. Taking the average energy of the six different models of a composition yields similar trends.

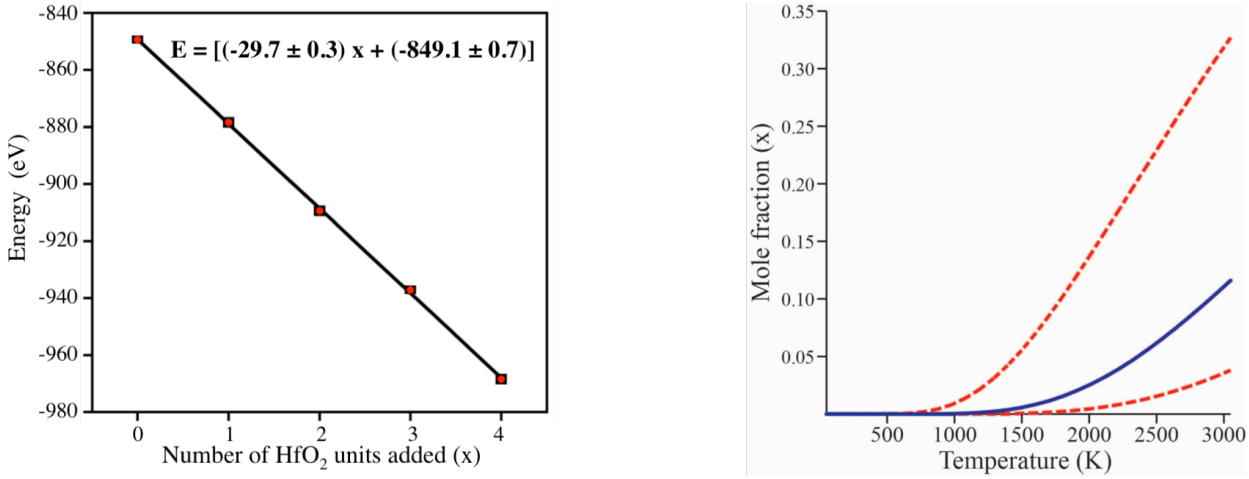

Figure 3: (Left) Energy of HfO_2-SiO_2 as a function of HfO_2 units added to SiO_2 (36 f.u.). A linear fit to the data is included as a line. (Right) Solubility of HfO_2 in SiO_2 as a function of temperature based on a regular mixing model using ΔH_{mix} = (0.8 ± 0.3) eV/HfO_2. Red dashed lines bracketing the blue solubility line mark the upper and lower bounds of uncertainty based on the error in ΔH_{mix}.

A linear fit to the data in Figure 3(left) yields a slope of -29.7± 0.3 eV/HfO_2. This energy, essentially, represents the partial enthalpy of HfO_2 in hafnia silica glass models with low hafnia content obtained via melt-quench ab inito molecular dynamics. With reference to the energy of monoclinic-HfO_2, for which we compute a value of -30.589 eV/HfO_2, we obtain an enthalpy of

mixing ΔH_{mix} of 0.8 eV/HfO_2 (±0.3 eV/HfO_2). While non-linear fits can be used to model the data shown in Figure 3, none of these has – within the error margin – a higher significance than the linear fit. Hence, up to 10 mol% HfO_2 ΔH_{mix} does not depend on concentration itself.

Using the computed ΔH_{mix} we estimate the solubility of HfO_2 in SiO_2 as a function of temperature within the scope of a regular mixing model.[29] We assume that ΔH_{mix} neither depends on temperature nor on concentration. The (ideal) entropy of mixing ΔS_{mix} is given by $\Delta S_{mix} = -R\,(x \cdot \ln(x) + (1-x) \cdot \ln(1-x))$, with x being the mol fraction of HfO_2. Using the equilibrium condition $\Delta G_{mix} = \Delta H_{mix} - T \cdot \Delta S_{mix} = 0$, solubility of HfO_2 in SiO_2 is computed and shown in Figure 3 (right). At the melting point of silica glass (1873 K) we determine a solubilty of 1.9 mol% HfO_2 in SiO_2. Propagating the error estimate of the enthalpy of mixing, we obtain a lower boundary of 0.3 mol% HfO_2 and an upper boundary of 11.6 mol% HfO_2 in hafnia silica glass.

Experimentally, a value of 3 mol% was determined for the solubility of hafnium dioxide in quenched silica glass at 1873 K.[4] Applying the regular mixing model, this value corresponds to $\Delta H_{mix} = 0.73$ eV/HfO_2, which in turn is well within our error margin. Goncalves et al. reported sol-gel synthesis of Erbium-doped HfO_2-SiO_2 glass with 30 mol% HfO_2 in silica.[5] The latter compounds (synthesized at 1173 K) are not in equilibrium according to Figure 3 (right). Ikeda et al. compared the energy of mixed HfO_2-SiO_2 glass structures only relative to amorphous HfO_2 and amorphous SiO_2.[10] They found a negative enthalpy of formation for less than 10 mol% HfO_2 dissolved in SiO_2.

3.3. Elastic properties

For every model, we computed elastic constants (without symmetry there are 21 independent stiffness coefficiets c_{ij}) and derived aggregate bulk modulus (B), shear modulus (G), and Young's modulus (E).[30] Bulk moduli were confirmed via additonal volume-energy calculations. To compare the elastic moduli for different HfO_2-SiO_2 compositions we first estimated a "projected density" for each composition assuming a linear rule of mixture for hafnia silica glasses and molar volumes of 26.94 cm^3 for a-SiO_2 and 22.32 cm^3 for HfO_2. We obtain a

density of 2.23 g/cm^3 for a-SiO_2, and densities of 2.39, 2.54, 2.69 and 2.83 g/cm^3 for mixed HfO_2-SiO_2 glasses of composition 1:36, 2:36, 3:36, and 4:36, repectively. However, we are left with the problem that models simulated with same composition end up with different densities after final optimization, necessitating a "calibration" of the computed moduli to the projected density for that composition. This is achieved through interpolation assuming that, for a given composition, B, G, and E depend linearly on density. Our results are given in Table 1. Experimental data for silica glass is 37, 31 and 73 GPa for B, G and E, respectively.[31] For the range of hafnia content in silica glass studied here, we do not find significant trends of moduli relating to composition. Experimental data of hafnia-silica films with hafnia content of 50-mol% report a Young's Modulus of 68 GPa increasing to 152 GPa with increasing HfO_2 content. [32]

Composition (mol%)	Expected Density [g/cm^3]	Bulk Modulus [GPa]	Shear Modulus [GPa]	Young's Modulus [GPa]
0:36 (0)	2.23	42	33	81
1:36 (2.7)	2.39	46	33	80
2:36 (5.3)	2.54	48	31	77
3:36 (7.6)	2.69	45	32	81
4:36 (10.)	2.83	44	31	75

Table 1 : Computed Bulk Modulus, Shear modulus and Young's modulus of hafnia silica glass for densities expected for the mixed models. We estimate an error of 4 GPa for each elastic modulus.

3.4. Vibrational Properties – Phonon Density of States and IR-Spectrum

Phonon Density of States (phDOS) of hafnia silica glasses with different compositions are shown in Figure 4 (left). Each graph is an average of six models for that composition. We included computed phDOSs of a-SiO_2 and a-HfO_2 into the same figure for comparison .

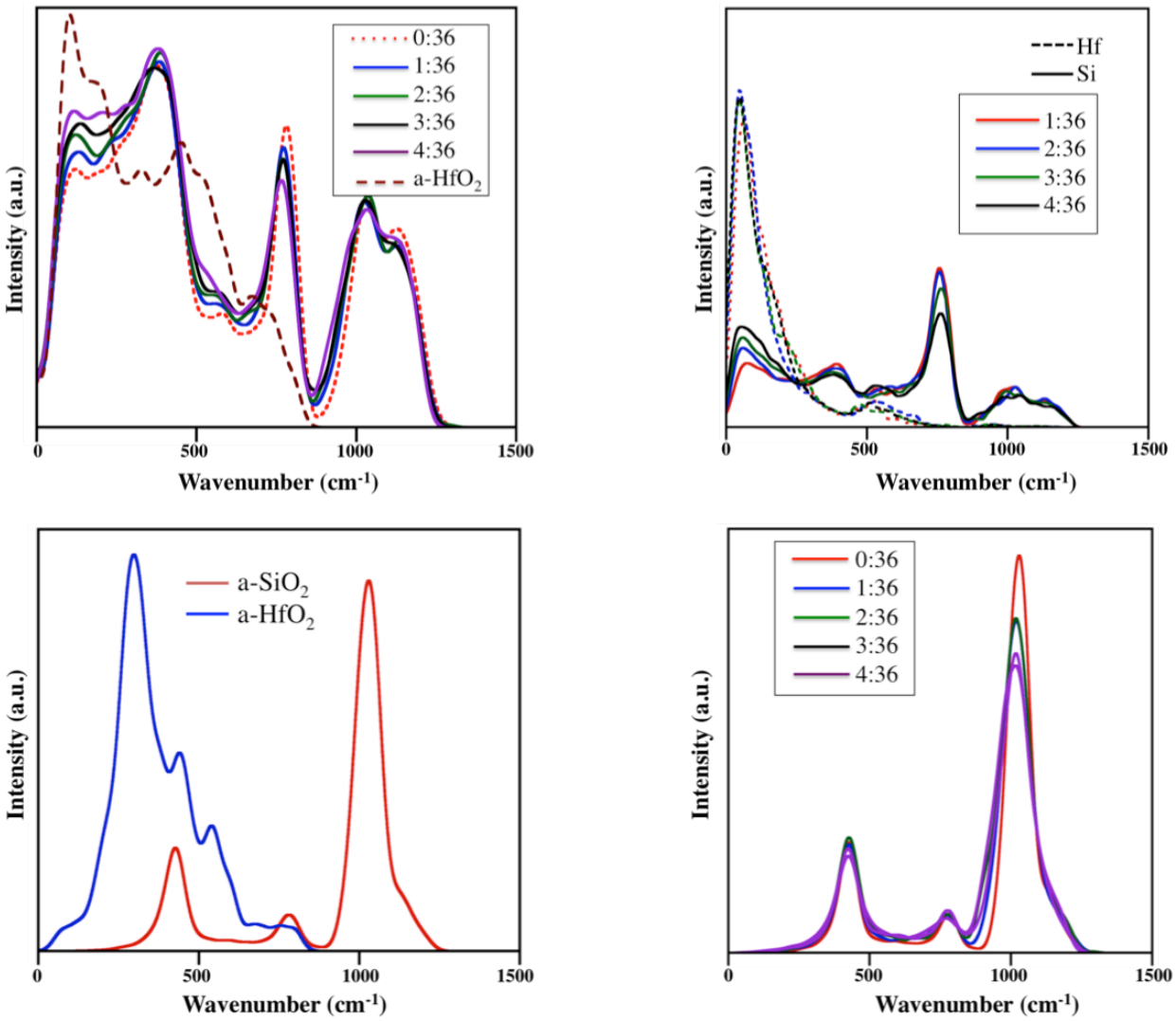

Figure 4: (Top Left) Phonon density of states for various hafnia-silica glasses shown together with those of a-SiO_2 and a-HfO_2 for comparison; (Top Right) Partial phonon density of states (Si and Hf only) of hafnia-silica models; (Bottom Left) IR spectra of a-SiO_2 and a-HfO_2; (Bottom Right) IR spectra of HfO_2-SiO_2 glass. All three spectra are obtained by convoluting individual frequencies with a Gaussian function of width 50 cm^{-1}

The phDOS of a-SiO_2 shows a strong band below 500 cm^{-1}, a peak at 780 cm^{-1}, and a double peak at 1030 and 1130 cm^{-1}. The double peak structure at high wavenumbers is characteristic of a-SiO_2 and has been found in experimental inelastic neutron scattering spectrum.[33, 34] The phDOS of a-HfO_2, in contrast, extends only up to 870 cm^{-1} and exhibits pronounced peaks at 104 cm^{-1} and 450 cm^{-1}. No experimental data is available for the phDOS of a-HfO_2. However, our

computed results agree well with previous DFT calculations.[35] The mixed models show significant changes with increasing hafnia content. Since the atomic mass of Hf is more than six times that of Si, we can expect that low frequencies become more populated with increasing Hf content. Indeed, we find that the region of highest frequencies shifts towards lower wave numbers: its edge is at 890 cm^{-1} in the 4:36 model in comparison to 930 cm^{-1} in a-SiO_2. The pronounced peak at 780 cm^{-1} decreases in intensity with increasing HfO_2 content, while the region at 150 cm^{-1}, characteristic for a-HfO_2, increases in its relative intensity with increasing HfO_2-content.

Partial phonon densities of states for Hf and Si in mixed models (Fig 4, top-right) show similar trends; strong vibrations of Hf at low frequencies (< 200 cm^{-1}) and vibrations of Si predominately at higher frequencies. Our results agree with computed phDOS of $Hf_{1-x}Si_xO_2$ (x = 0, 0.25, 0.50) of Chen et al.[36]

3.5. IR spectra

Computed IR spectra for hafnia silica glasses, shown in Figure 4 (right), underline the impact of hafnia on vibrational properties of the mixed glasses. Most prominent is a shift of the characteristic peak at 1030 cm^{-1} towards lower frequencies (1015 cm^{-1} for 10 mol% HfO_2), accompanied by a shift in the lower frequency-edge of this peak and by a decrease of its intensity. The signal at 470 cm^{-1} does not change significantly when HfO_2 is added to SiO_2. Interestingly, a line at 270 cm^{-1}, which would be characteristic of HfO_2, does not develop even in models containing 10 mol% HfO_2.

3.6. Heat Capacity at Constant Volume (C_v)

Figure 5 shows heat capacities at constant volume (C_v) as a function of temperature for models of silica and hafnia silica glasses. C_v is based on vibrational data and computed using the harmonic approximation.[23] Each curve represents an average over six models. We obtain standard errors for the data for temperatures above 300 K ranging from 1 J/(K·mol) for 0:36

models to 3 J/(K·mol) for 4:36 models. At high temperatures C_v approaches the Dulong-Petit limit. Therefore, values at high temperatures highlight the addition of one unit HfO_2 from one composition to the next; since the number of atoms increases, the number of degrees of freedom increases too. Consequently, at high temperatures C_v appears to increase by a constant amount characteristic of adding one unit of HfO_2. The impact of HfO_2 can, therefore, be analyzed by taking the difference between C_v of different models, approximating a "partial C_v" of a-HfO_2 in mixed hafnia silica glasses (see Figure 5, right). Essentially, we find that the partial C_v of a-HfO_2 in hafnia silica glasses agrees with C_v of pure a-HfO_2. Note that the error of this data is $\sqrt{2}$ times the error of C_v, mentioned above.

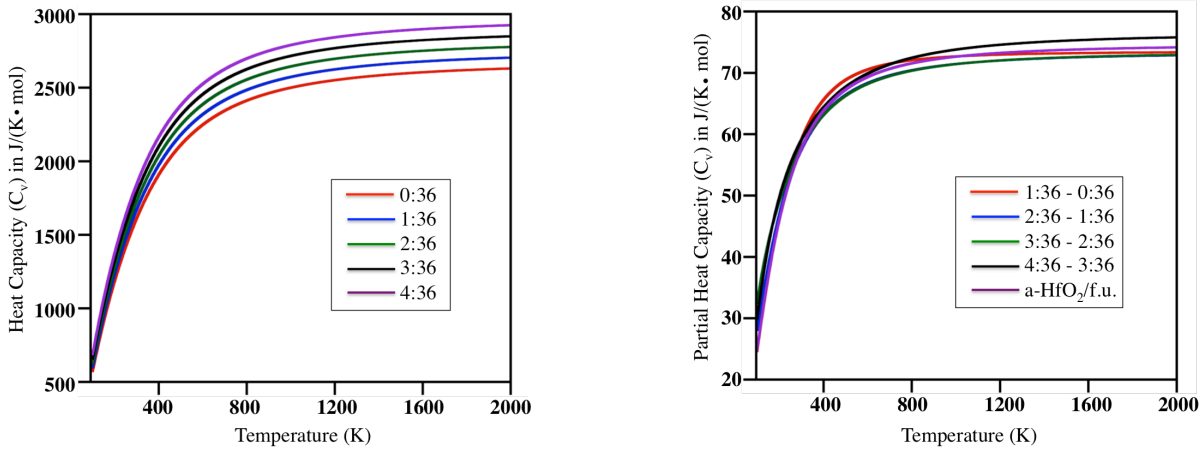

Figure 5: (Left) C_v of HfO_2-SiO_2 glass as a function of temperature (the unit mol refers to the number of atoms in the simulation cell times N_A); (Right) Partial Heat capacity of HfO_2 in SiO_2 obtained by taking differences of C_v from models with different compositions.

3.7. Non-linear changes in the phDOS and a possible rupture of Floppy Modes

A last analysis is devoted to low frequency vibrational modes, in particular the range below 200 cm^{-1}. In a simple one-dimensional chain of atoms, replacement of Si by heavier Hf will increase the population of low-frequency modes.[37] A comparison of the phDOSs of silica and hafnia in Figure 4 indicates that this holds for the overall "center of mass" of the graph, and in particular refers to the modes below 200 cm^{-1}. Figure 4 also indicates growth in relative intensity of the

region at 150 cm^{-1}, characteristic for a-HfO_2. However, the models differ by added units of HfO_2, and for quantifying the relative change per cation, thus studying the effect of replacing Si by Hf, we need to calibrate the data "*per mol of cations*". Evidently, at very high temperatures, in the Dulong-Petit limit, such calibrated phDOS curves of $(HfO_2)_x(SiO_2)_{1-x}$ will look identical, since they have the same number of atoms and degrees of freedom. The difference between phDOSs of models with different composition, thus, will be zero at high temperatures. At intermediate temperatures, however, the difference will reflect the impact of replacing Si by Hf.

We introduce two new quantities to charactertize the impact of HfO_2 in mixed hafnia silica glasses. First dDOS(ν), which is the difference between normalized PhDOS(ν)'s of two different compositions. Since we compare normalized spectra of $(HfO_2)_x(SiO_2)_{1-x}$ with identical number of atoms and degrees of freedom, dDOS(ν) will be zero for low frequencies as well as for high frequencies, but will show positive or negative values at intermediate frequencies. Due to the nature of the frequency data we compute, we find that all dDOS(ν)'s show rapid oscillations making it very difficult to visualize trends. To further the analysis we, therefore, introduce a second quantity, IdDOS(ν), the integration of dDOS(ν): IdDOS(ν) = $\int_0^{\nu} phDOS^{x_2}(\nu') - phDOS^{x_1}(\nu')d\nu'$ where $x_2 > x_1$. Since we study trends with composition, we focus on pairs (x_2,x_1) = (0.027,0), (0.053,0.027), (0.076,0.053), (0.1,0.076), reflecting the successive substitution of Si by Hf. IdDOS(ν) simply counts the accumulated surplus or deficiency in the number of modes per atom (or cation) from zero wavenumber up to a given wavenumber ν. At high wavenumbers IdDOS(ν) will be zero. One may expect that the IdDOS will be positive throughout the frequency range for any pair (x_2,x_1), if only $x_2 > x_1$, since replacement of Si by Hf populates lower frequency modes. Interestingly, regions with negative IdDOS exist even for wavenumbers below 500 cm^{-1} (see Figure 6).

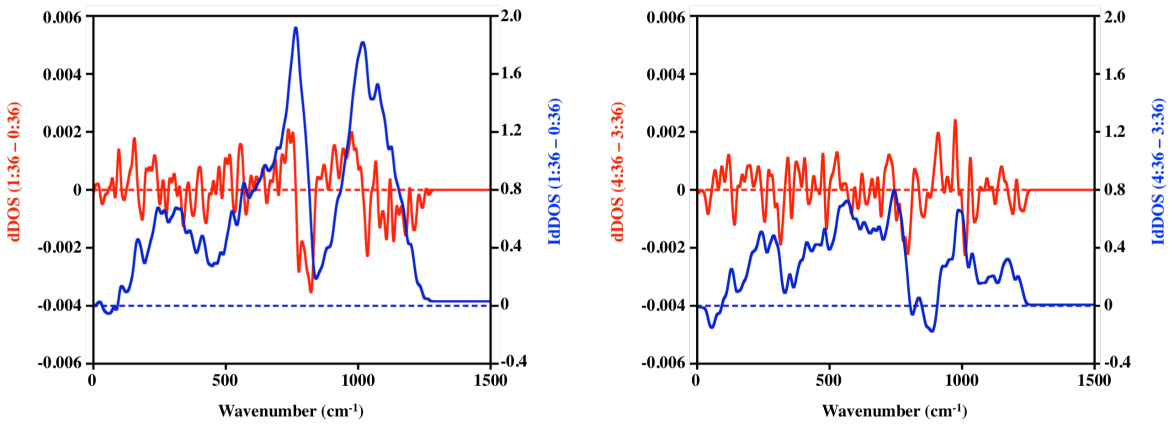

Figure 6: dDOS(ν) (upper curve) and IdDOS(ν) (lower curve) comparing vibrational spectra (normalized phDOS(ν)) of 1:36 and 0:36 (left) and 4:36 and 3:36 (right). Graphs have been stacked to show the relation between dDOS and its integration, IdDOS. The initial data (normalized phDOS) was obtained by convoluting individual frequencies with a Gaussian function of 15 cm^{-1} width. A negative value of IdDOS(ν) implies that the composition with higher Hf content has a deficiency of vibrational modes accumulated up to this wavenumber.

dDOS(ν) and IdDOS(ν) comparing 1:36 and 0:36 models (x=0.027 and x=0) are shown in Figure 6 (left). Large positive values at 970 cm^{-1} and negative values at 1050 cm^{-1} indicate a shift of the high frequency peak towards lower wave numbers upon addition of HfO_2 to the glass (see also Figure 6). A negative value of the dDOS at ~800 cm^{-1} reflects the decrease of frequencies in this region upon adding HfO_2. Unfortunately, despite being averaged over six models, the dDOS varies rapidly and direct inspection does not yield further details. Nonetheless, there are systematic trends in the dDOS which become apparent in the IdDOS. Overall, the IdDOS is positive, as expected. However, negative values at 50 cm^{-1} indicate that the model with higher Hf content is deficient of low-frequency vibrational modes. Hence, replacing SiO_2 partially by HfO_2 de-populates low frequency modes. This effect is barely seen in the dDOS, which has more negative than positive contributions, but oscillates rapidly around zero. Admittedly, the depletion of low-frequency modes in HfO_2-doped SiO_2 is not large, but it is persistent. We observe it comparing models 1:36 and 0:36 and to lesser extend for models 2:36 and 1:36. There is no

depletion comparing models 3:36 and 2:36. Still a pronounced negative IdDOS at 55 cm^{-1} appears comparing 4:36 and 3:36, see Figure 6 (right).

We speculate that the observed depletion relates to "floppy modes" and the extent of collective movements of larger clusters of atoms in SiO_2.[37, 38] Adding a heavy Hf atom into the structure (by replacing Si by Hf) "pins" such modes and, consequently, reduces partially some low-frequency modes. The more pronounced negative IdDOS at 55 cm^{-1} comparing 4:36 and 3:36 then is due to larger $(HfO)_x$–units built by clustering Hf-O-Hf linkages. A focused modeling targeting these effects in larger models may yield more insight into this effect.

4. Conclusion

We present a detailed investigation of the structural, mechanical, vibrational and thermodynamic properties of hafnia-silica glasses with low hafnia content (≤ 10 mol%) using density functional calculations. Models generated by a melt-quench procedure comprise Si in four-fold coordination, while Hf shows four, five and six-fold coordination with oxygen. Network statistics show an excess of Hf-O-Hf linkages indicative of formation of HfO_x-clusters. We compute an enthalpy of mixing of HfO_2 in SiO_2 of (0.8 ± 0.3) eV/HfO_2, and within a regular solution model we predict a solubility of HfO_2 in SiO_2 of 1.9 [-0.3/+11.6] mol% at 1873 K. Elastic moduli for mixed glasses are not significantly different from those of pure silica glass. The heat capacity of mixed glasses is well described by a simple rule of mixture model, adding C_v of a-HfO_2 and a-SiO_2 in appropriate amounts. We detail the impact of hafnia on vibrational modes of the silica glass, notably a down-shift of the high-frequency IR-signal, which should be accessible though experiment. Our data also suggests a depletion of low-frequency vibrational modes, if HfO_2 is added to SiO_2. Heavy Hf atoms and small HfO_x-clusters effectively pin floppy modes in silica glass.

Acknowledgements

This work was supported by the US AFOSR (Dr. Ali Sayir) and NASA (Dr. Anthony Calomino) under the National Hypersonic Science Center for Materials and Structures (AFOSR contract no. FA9550-09-1-0477). Computational work was made possible through generous grants by the Texas Advance Computing Center in Austin, TACC, Texas, and by the High Performance Computing facilities at UTA.

References

[1] J.H. Choi, Y. Mao, J.P. Chang, Mater. Sci. Eng. R-Rep., 72 (2011) 97-136.

[2] S. Berneschi, S. Soria, G.C. Righini, G. Alombert-Goget, A. Chiappini, A. Chiasera, Y. Jestin, M. Ferrari, S. Guddala, E. Moser, S.N.B. Bhaktha, B. Boulard, C.D. Arfuso, S. Turrell, Opt. Mater., 32 (2010) 1644-1647.

[3] E. Wuchina, E. Opila, M. Opeka, W. Fahrenholtz, I. Talmy, The Electrochemical Society Interface, 16 (2007) 30-36.

[4] T.P. Ledneva, K.A. Bryukhova, Steklo, 2 (1973) 84-87.

[5] R.R. Gonçalves, G. Carturan, L. Zampedri, M. Ferrari, M. Montagna, A. Chiasera, G.C. Righini, S. Pelli, S.J.L. Ribeiro, Y. Messaddeq, Appl. Phys. Lett., 81 (2002) 28-30.

[6] D.A. Neumayer, E. Cartier, J Appl. Phys., 90 (2001) 1801-1808.

[7] T.P. Smirnova, V.V. Kaichev, L.V. Yakovkina, V.I. Kosyakov, S.A. Beloshapkin, F.A. Kuznetsov, M.S. Lebedev, V.A. Gritsenko, Inorg. Mater., 44 (2008) 965-970.

[8] P. Broqvist, A. Pasquarello, Appl. Phys. Lett., 90 (2007) 082907.

[9] P. Broqvist, A. Pasquarello, Microelectron. Eng., 84 (2007) 2416-2419.

[10] M. Ikeda, G. Kresse, T. Nabatame, A. Toriumi, Mater. Sci-Poland, 23 (2005) 401-406.

[11] W.L. Scopel, A.J.R. da Silva, A. Fazzio, Phys. Rev. B, 77 (2008) 172101.

[12] P. Hohenberg, W. Kohn, Phys. Rev. B, 136 (1964) B864-B871.

[13] G. Kresse, J. Non-Cryst. Solids, 193 (1995) 222-229.

[14] G. Kresse, J. Hafner, Phys. Rev. B, 49 (1994) 14251-14269.

[15] G. Kresse, J. Furthmuller, Phys. Rev. B, 54 (1996) 11169-11186.

[16] P.E. Blochl, Phys. Rev. B, 50 (1994) 17953-17979.

[17] G. Kresse, D. Joubert, Phys. Rev. B, 59 (1999) 1758-1775.

[18] R. Hill, P Phys. Soc. Lond. B, 65 (1952) 396-396.

[19] A. Reuss, ZAMM - J. Appl. Math. Mech. / Z Angew MATH MECH, 9 (1929) 49-58.

[20] W. Voigt, Lehrbuch der kristallphysik (mit ausschluss der kristalloptik), B.G. Teubner J.W. Edwards, Leipzig; Berlin; Ann Arbor, Mich., (1946).

[21] F.D. Murnaghan, Proc. Natl. Acad. Sci. U.S.A., 30 (1944) 244-247.

[22] A. Togo, F. Oba, I. Tanaka, Phys. Rev. B, 78 (2008) 134106.

[23] C. Kittel, Introduction to Solid State Physics, Wiley, New York, (1985).

[24] P. Giannozzi, S. Baroni, Journal of Chemical Physics, 100 (1994) 8537-8539.

[25] K.E. Kelsey, J.F. Stebbins, J.L. Mosenfelder, P.D. Asimow, Am. Mineral., 94 (2009) 1205-1215.

[26] J.R. Allwardt, B.T. Poe, J.F. Stebbins, Am. Mineral., 90 (2005) 1453-1457.

[27] D.R. Neuville, L. Cormier, D. Massiot, Chem. Geol., 229 (2006) 173-185.

[28] P. Kroll, Ceramics Science and Technology, in: R. Riedel, I.-W. Chen (Eds.) Structures, Wiley-VCH, Weinheim, (2008), pp. 41.

[29] J.H. Hildebrand, Nature, 168 (1951) 868-868.

[30] J.F. Nye, Physical Properties of crystals: their representation by tensors and matrices, Clarendon Press, (1972).

[31] W. Pabst, E. Gregorova, Ceram-Silikaty, 57 (2013) 167-184.

[32] D.K. Venkatachalam, J.E. Bradby, M.N. Saleh, S. Ruffell, R.G. Elliman, J. Appl. Phys., 110 (2011) 043527.

[33] J.M. Carpenter, D.L. Price, Phys. Rev. Lett., 54 (1985) 441-443.

[34] A. Lehmann, L. Schumann, K. Hubner, Phys. Status Solidi B-Basic Research, 117 (1983) 689-698.

[35] X. Luo, in, University of Texas at Austin, (2010).

[36] T.J. Chen, C.L. Kuo, J. Appl. Phys., 110 (2011).

[37] M.F. Thorpe, EEERS. Electr. Mat. Ser., 1 (1995) 185-196.

[38] Y. Cai, M.F. Thorpe, Phys. Rev. B, 40 (1989) 10535-10542.

Appendix 1:

In this section, I include supplementary data related to the HfO_2-SiO_2 project.

A1) Fitting Equation of State to volume-energy data for HfO_2-SiO_2 models to extract Bulk Modulus:

Bulk modulus is defined as the ratio of the infinitesimal pressure increase to the resulting decrease of the volume. In thermodynamic terms,

$$B = -V\frac{dP}{dV}; where\ B = Bulk\ modulus, V = volume\ and\ P = pressure$$

Hence B is the inverse of compressibility. A typical way to calculate bulk modulus of solid systems is to fit a thermodynamic equation of state (EOS) to a plot of total energy of the system as a function of system volume. There are different equations of states for the matter. I choose the Murnaghan equation to 4 representative HfO_2-SiO_2 models with varying composition. [1] The Murnaghan EOS assumes that B varies linearly with pressure, P. Thus:

$$E(V) = \left(\frac{B_0 V}{B_0'}\right)\left[\frac{\left(\frac{V_0}{V}\right)^{B_0'}}{B_0' - 1} + 1\right] - \left(\frac{B_0 V_0}{B_0' - 1}\right) + E_0$$

Where: B_0, V_0 and E_0 is the zero-pressure bulk modulus, volume and energy respectively. The pressure derivative of zero-pressure bulk modulus is B_0'. The Murnaghan EOS works very well for small compressions. All my computations increase/decrease the cell parameters no greater than 3 % of it's original values.

The curve-fittings for representative models for all compositions of a-HfSiO are included in Figure A1.1. Recall that I used 6 models for each composition of a-HfSiO. An average B_0 calculated over these 6 models are in agreement, except for a-SiO_2, with values calculated from elastic stiffness matrix. (See table A1)

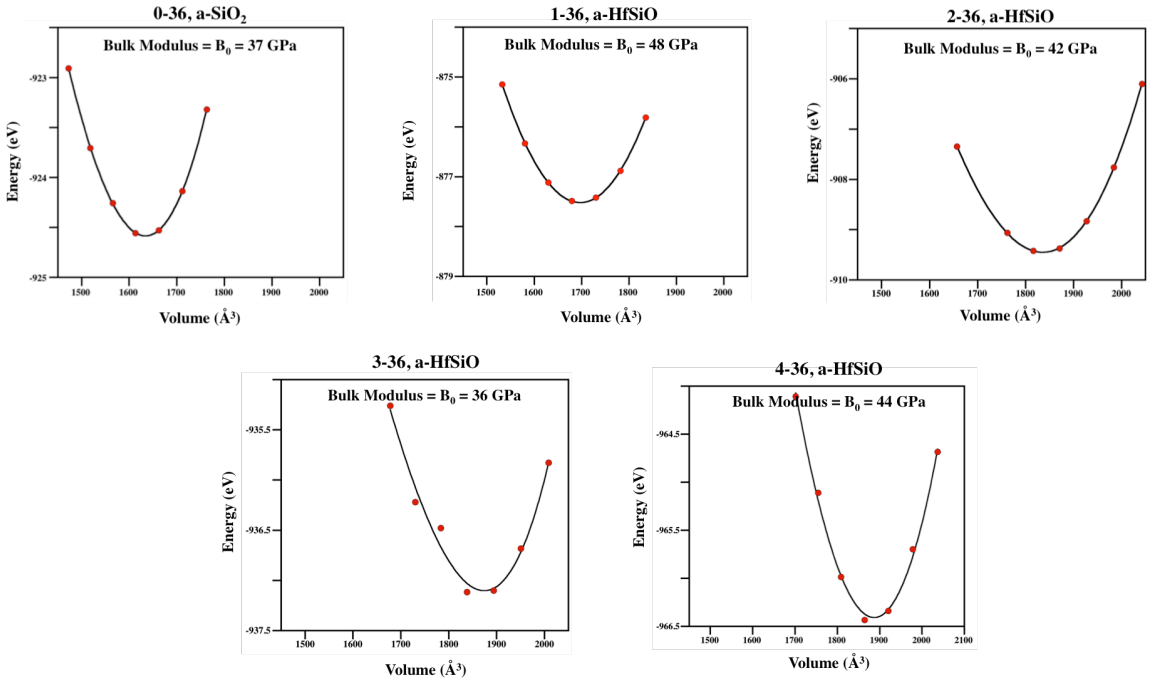

Figure A1.1: Murnaghan EOS fitting to Energy-Volume data of HfO_2: SiO2 amorphous models. Top row: far left - 0:36; middle – 1:36 and far right – 2:36; Bottom row: left and right – 3:36 and 4:36 respectively. The zero-pressure Bulk modulus for 0:36, 1:36, 2:36. 3:36 and 4:36 is 37 GPa, 48 GPa, 42 GPa, 36 GPa and 44 GPa, respectively.

Composition (mol%)	Density ($g \cdot cm^{-3}$)	B_0 from E-V fitting (GPa)	B from stiffness matrix (GPa)
0:36 (0)	2.01	37 ± 1	42 ± 1
1:36 (2.7)	2.31	46 ± 2	46 ± 2
2:36 (5.3)	2.47	47 ± 2	48 ± 2
3:36 (7.6)	2.52	44 ± 3	43 ± 2
4:36 (10.)	2.68	42 ± 2	46 ± 3

Table A1.1: Computed Bulk modulus of hafnia silica glass from 1) EOS fitting to E-V data 2) Calculated from elastic stiffness matrix. All values are an average over 6 models with standard error between 1-3 GPa. Densities listed are actual average densities of models, and not those calculated from a rule of mixing (as in Table 1 of published manuscript)

A2) Linear dependence of B, G and E on the mol fraction of HfO_2 in a-HfSiO models

In this section, I include plots (See Fig. A1.2) of elastic moduli – B, G and E for a given composition as a function of the average density of the 6 models generated for that composition. This data is crucial, as an assumption is made in the manuscript that for a given composition, B, G, and E depend linearly on density. Linear fits to the data demonstrate that B, G and E depend very weakly on the average model density for any composition. However, this trend is sufficient to extrapolate the moduli values for the expected density of HfO_2-SiO_2 glass from a simple rule of mixture.

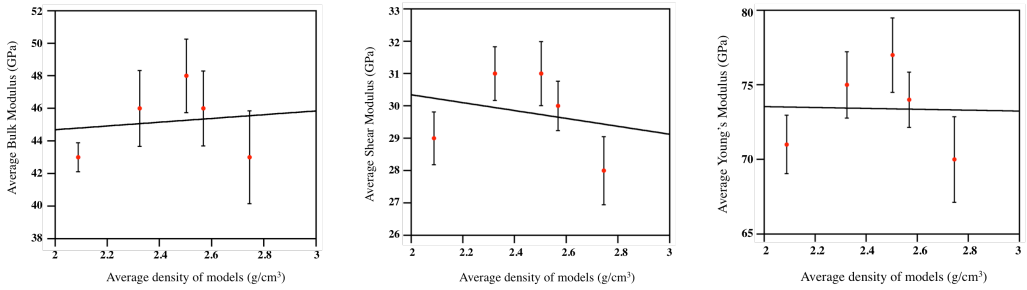

Figure A1.2: Average elastic moduli – bulk moduli B (left), shear moduli G (middle) E (right) of HfO_2-SiO_2 models plotted as a function of the average density of the models. The lines in each diagram are linear fits to the data. Error bars in each figure represent computed standard error.

A3) Thermal conductivity of HfO_2-SiO_2 models from Clarke's model: [2]

The Young's modulus E, computed from elastic stiffness matrix enables us to calculate the minimum lattice thermal conductivity (κ_{min}) of HfO_2-SiO_2 glass using the phenomenological Clarke's model according to:

$$\kappa_{\min} = 0.87 k_B N_A^{2/3} \frac{m^{2/3} \rho^{1/6} E^{1/2}}{M^{2/3}}$$

where: E is Young's modulus, M is the mass, m is the number of atoms in the system, k_B is the Boltzmann constant and N_A is the Avogadro's number. The minimum phonon mean free path is assumed to be the cube root of the volume of the system and the mean phonon velocity includes only the acoustic modes.

The data (Table A1.2) shows no significant difference between the κ_{min} of amorphous silica and that of mixed HfO_2-SiO_2 models. This result is expected as Clarke's model assumes a material is homogenous when estimating the phonon mean free path, which produces a bulk scalar quantity for thermal conductivity. This assumption of homogeneity does not allow for individual atom mass, local chemistry or defects in structure to contribute to the thermal conductivity. Thus in a binary system, such as hafnia- silica, the Clarke's model does not account for the clustering of hafnia or the large difference in mass between hafnium and silicon. This stands as a failure of the method as the hafnia-silica glasses shows depletion of low-frequency phonon modes in their phonon density of states. These low frequency phonon models are known to dominate heat conduction in solids. [3](More details included in Section A3)

Composition (mol%)	Density ($g \cdot cm^{-3}$)	E (GPa)	(M/m) (Kg)	κ_{min} ($Wm^{-1}K^{-1}$)
0:36 (0)	2.01	71	20.03	1.1
1:36 (2.7)	2.31	76	21.24	1.1
2:36 (5.3)	2.47	77	22.67	1.0
3:36 (7.6)	2.52	70	23.88	1.0
4:36 (10.)	2.68	75	25.04	1.0

Table A1.2: Minimum lattice thermal conductivity of hafnia-silicate glass using Clarke's phenomenological model

A4) Non-linear changes in phDOS and a possible rupture of floppy modes

A major conclusion from my study with HfO_2-SiO_2 glass is that there is a depletion of low frequency vibrational modes when HfO_2 is added to SiO_2 glass. The dDOS, or difference between normalized phonon density of states (phDOS) and IdDOS, which is integrated dDOS, illustrates this phenomena nicely with the difference of: 0:36 and 1:36 and 3:36 and 4:36. It is interesting to note what happens if differences are considered between models that vary in their HfO_2 composition by more than one unit. I define the IdDOS(2) as: $\int_0^{\vartheta} phDOS^{x_4}(\vartheta') - phDOS^{x_2}(\vartheta')d\vartheta$ where $x_4 - x_2 = (10. - 5.3), (7.6 - 2.7)$ and $(5.3 - 0)$. Similarly IdDOS(3) is defined as $\int_0^{\vartheta} phDOS^{x_4}(\vartheta') - phDOS^{x_1}(\vartheta')d\vartheta$ where $x_4 - x_1 = (10.0 - 2.7)$ and $(7.6 - 0)$. One representative plots of IdDOS (2), in particular between (10.0 – 5.3) and IdDOS (3), specifically (10.0 – 2.7) is shown is Figure A1.3. Considering mass effects in a 1-D linear chain model for atomic vibrations in solids, it is expected to observe a higher population of vibrational states in the low frequency regions in the 4:36 model compared to the 1:36 or 2:36 model due to the presence of more Hf atoms in the 4:36 model. [3] However, I observe negative difference between populated phonon modes for IdDOS(2)[10.0 – 5.3] at 44 cm^{-1} and IdDOS(3)[10.0 – 2.7] at 22 cm^{-1}. Thus, the effect of "pinning floppy modes" is observed. This negative IdDOS is attributed to larger $(HfO)_x$ built by clustering Hf–O–Hf linkages, best observed in 4:36 models.

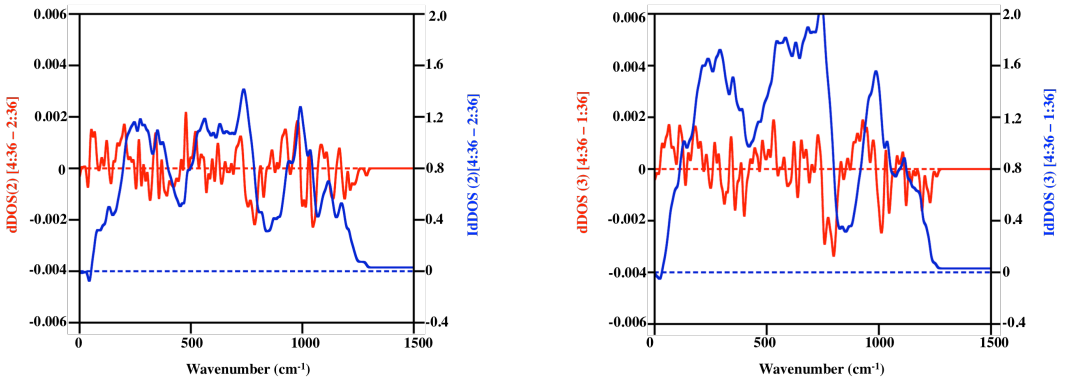

Figure A1.3: dDOS(ν) (upper curve, red) and IdDOS(ν) (lower curve, blue) comparing vibrational spectra (normalized phDOS(ν)) of 4:36 and 2:36 (left) and 4:36 and 1:36 (right). Graphs have been stacked to show the relation between dDOS and its integration, IdDOS. The initial data (normalized phDOS) was obtained by convoluting individual frequencies with a Gaussian function of 15 cm^{-1} widths. A negative value of IdDOS (2) at 44 cm^{-1} and IdDOS (3) at 22 cm^{-1} implies that the composition with higher Hf content has a deficiency of vibrational modes accumulated up to this wavenumber and shows the effect of pinning floppy modes in glasses.

References:

[1] F.D. Murnaghan, The compressibility of media under extreme pressures, P Natl Acad Sci USA 30 (1944) 244-247.

[2] D.R. Clarke, Materials selection guidelines for low thermal conductivity thermal barrier coatings, Surf Coat Tech 163 (2003) 67-74.

[3] C. Kittel, Interpretation of the Thermal Conductivity of Glasses, Phys Rev 75(6) (1949) 972-974.

Summary:

Hafnia-silica glasses (HfO_2-SiO_2) with low hafnia content are the subject of interest in this project. Small, yet realistic models of HfO_2-SiO_2 are constructed containing 108 – 120 atoms. Hf atoms adopt 4, 5 and 6 fold geometry and show a preference for clustering, or formation of Hf–O–Hf linkages. These HfO_x clusters contribute to the pinning of low frequency vibrational modes (also known as *floppy modes*). The absence of these *floppy modes* are predicted to affect the thermal conductivity of these glasses. In addition, further investigation shows that a single unit of HfO_2 is enough to trigger the pinning effect. Heat capacity and vibrational spectra (both phonon density of states – phDOS and IR spectra) for these glass compositions are in accordance to expectation. They exhibit a simple *rule of mixing* where the properties of the mixed sytem are a weighted means of the properties of the pure systems. However, computed elastic moduli and minimum lattice thermal conductivity are exceptions as these properties show almost no impact of the added HfO_2.

This work is a valuable addition to other computational studies done so far on HfO_2-SiO_2 due to the following reasons:

1. Previous work on HfO_2-SiO_2 glass targets higher (> 25) mol % of HfO_2 dissolved in SiO_2. This is the first instance of a reliable study with small quantities of HfO_2.
2. For the first time, the solubility of HfO_2 in SiO_2 is verified using precise quantum chemical calculations. The reported values (1.9 [-0.3/+11.6] mol% at 1873 K) also agree to the only available experimental data within limits of standard error.
3. Absence of low frequency *floppy modes* in hafnia-silica glass compositions due to presence of HfO_x clusters is also observed for the first time.

Future research may involve extensive study of the thermal conductivity of these models. As phonons are main carriers of heat in amorphous systems, modal dependency of thermal conductivity using Green-Kubo approach [1] may be an interesting find. Moreover, the dielectric constant for these systems may be investigated as they are target materials for gate dielectrics.

References

[1] W. Lv, A. Henry, Direct calculation of modal contributions to thermal conductivity via Green-Kubo modal analysis, New J Phys 18 (2016)

CHAPTER 2

FIRST PRINCIPLES MODELING AND SIMULATION OF Zr-Si-B-C-N CERAMICS: DEVELOPING HARD AND RESISTANT COATINGS[2]

[2] This work has been published in Acta Materialia and is being used with the permission of the publisher, 2016

Scope and Motivation

Zirconium borides, carbides, and nitrides belong to a prominent and valued category of ceramics known as Ultra-High Temparature Ceramics (UTHCs). UTHCs are known as such due to their high melting points (> 3000 K), high thermal conductivity and thermal shock resistance. [1] These materials are also classified as "hard materials" with hardness values more than 20 GPa. [2] Popular applications of Zr-based compounds are cutting tools, drill bits and as coatings on engine valves. However, these materials have poor oxidation resistance at high temperature. For example, ZrB_2 reacts with oxygen to form B_2O_3 that volatilizes above 1373 K according to the reaction: $2\ ZrB_2 + 5\ O_2 \rightarrow 2\ ZrO_2\ (s) + 2\ B_2O_3\ (l, g)$

In contrast to zirconium based ceramics, silicon based ceramics (e.g. SiC, Si_3N_4, etc.) possess excellent oxidation resistance up to 1800 K. This oxidation resistance is due to the formation of an outer layer of SiO_2 glass that inhibits oxygen diffusion into the inner parent material. Thus by combining functional properties such as hardness and oxidative resistance of different compounds (here zirconium and silicon based ceramics respectively), we can design materials with tailored properties.

Experimental work conducted at the Department of Material Science and Engineering at UTA has investigated amorphous thin films (thickness between 3.5 and 4.1 μm) of ZrBCN. These were synthesized by pulsed magnetron sputtering of Zr and B_4C targets in flowing N_2. Films of composition $Zr_{41}B_{30}C_8N_{20}$ showed a high hardness (36 GPa) due to the formation of "nano-domains" in the material. However, the oxidation resistance proved poor - only up to 800 K. [3, 4] The addition of silicon based ceramics to films of $Zr_{41}B_{30}C_8N_{20}$ could improve the oxidation resistance.

In this project, my goal is to model theoretical ZrSiBCN ceramics and study the hardness using ab-initio molecular dynamics. This project is a part of the "Materials Genome Initiative" which aims to accelerate advanced materials discovery and deployment in the United States. At the end of this chapter is an appendix where I include detailed supplementary information.

References

[1] W.G. Fahrenholtz, E.J. Wuchina, W.E. Lee, Y. Zhou, Introduction, Ultra-High Temperature Ceramics, John Wiley & Sons, Inc 2014, pp. 1-5.

[2] E.W. Neuman, G.E. Hilmas, Mechanical Properties of Zirconium-Diboride Based UHTCs, Ultra-High Temperature Ceramics, John Wiley & Sons, Inc2014, pp. 167-196.

[3] M. Zhang, J. Jiang, J. Houska, J. Kohout, J. Vlcek, E.I. Meletis, A study of the microstructure evolution of hard Zr-B-C-N films by high-resolution transmission electron microscopy, Acta Mater. 77 (2014) 212-222.

[4] M. Zhang, J. Jiang, J. Vlček, P. Steidl, J. Kohout, R. Cerstvy, E.I. Meletis, Effect of Nitrogen Content on the Microstructure and Hardness of Hard Zr-B-C-N Films, Microscopy and Microanalysis 20(SupplementS3) (2014) 1892-1893.

First Principles Modeling and Simulation of Zr-Si-B-C-N ceramics: Developing Hard and Resistant Coatings

Atreyi Dasmahapatra[1], Efstathios Meletis[2], and Peter Kroll[1,*],

[1] Department of Chemistry and Biochemistry, The University of Texas at Arlington, 700 Planetarium Place, Arlington, Texas 76019, United States.

[2] Department of Materials Science and Engineering, University of Texas at Arlington, 501 West First St., Arlington, Texas 76019, United States.

Abstract

We model amorphous ZrSiBCN ceramics combining ab-initio molecular dynamic simulations with melt-quench and simulated annealing techniques. Starting from the parent composition $Zr_{42}B_{30}C_8N_{18}$ we systematically increase the Si_3N_4 content along four different pathways in the composition diagram and evaluate trends in structure and properties. Mixtures of ZrB_2, ZrN, and ZrC exhibit Zr layers as well as ZrB_2 and ZrN(C) nuclei, but addition of Si_3N_4 reduces structural order in the models. Elastic moduli decrease with increasing Si_3N_4 content to values less than expected of a simple mixture model. Thus, while addition of Si_3N_4 to amorphous ZrBCN coatings may improve oxidation resistance, this needs to be balanced with desired mechanical properties.

Keywords:
Hard coatings, density functional theory calculations, ab-initio molecular dynamics, elastic moduli, nucleation

Introduction:

Zirconium borides, carbides and nitrides are ultra high temperature ceramics (UHTCs) with melting points above 3000° C. [1, 2] They are frequently used as protective coatings due to their refractory nature and high hardness. [3, 4] Thin films of ZrB_2, ZrC, or ZrN are synthesized via physical vapor deposition (PVD) processes, for instance by reactive magnetron sputtering [5] or via chemical vapor deposition (CVD) techniques. [6, 7] In a recent study, quaternary ZrBCN films with thickness between 3.5 and 4.1 μm have been synthesized by pulsed magnetron sputtering of Zr and B_4C targets in flowing N_2. [8, 9] These coatings exhibit hardness up to 36 GPa, and the high value is attributed to a nano-domain structure of ZrN grains joined via monolayer interfaces. [8, 9]

At elevated temperatures zirconium-based UHTC's have poor oxidation resistance, unfortunately. [10] ZrB_2 forms ZrO_2 and B_2O_3 upon oxidation, and although a protective layer of glassy B_2O_3 forms, it evaporates rapidly at temperatures exceeding 1200° C exposing a non-protective ZrO_2 layer. [11-13] Zirconium carbides oxidize at temperatures lower than ZrB_2, at 1000° C. [14] Zirconium nitrides have the least oxidation resistance forming ZrO_2 at temperatures as low as 500°C. [15-17] The quaternary ZrBCN films mentioned above show strong oxidation at 800°C. [8, 9]

An approach to improve oxidation resistance of zirconium borides at high temperatures is the addition of a silicon bearing compound, for example silicon nitride [18] or silicon carbide. [19] Significant improvements to oxidation resistance (up to 1900°C) have been reported for ZrB_2 and 20 vol% SiC composites. [20] Oxidation resistance of ZrB_2-Si_3N_4 ceramics was found to increase to 1300-1400 °C with increasing Si_3N_4 content due to formation of a protective layer of borosilicate glass. Addition of 10 mol% of Cr and Ta diborides to these ZrB_2-Si_3N_4 coatings improved the oxidation resistance further. [21]

The high temperature mechanical properties of these materials have also been another prominent field of study. Addition of 20 vol% SiC to ZrB_2 decreases the Young's modulus of

510 GPa at room temperature to 420 GPa at 1400 °C. [22] At 1600 °C, the Young's modulus then plunges to 100 GPa. Another study finds the Young's modulus of ZrB_2-SiC composites dropping to 210 GPa at 1500 °C compared to 510 GPa at room temperature. [23] This decrease in Young's modulus is attributed to the presence of oxides at grain boundaries in the polycrystalline material. [24] The presence of 5% Si_3N_4 as a sintering aid in pure ZrB_2 also lowers the Young's Modulus to 419 GPa. [25] At room temperature, ZrB_2-SiC composites have exhibited Vickers hardness of 17-24 GPa depending on the SiC particle size. [26, 27]. Addition of Si_3N_4 to ZrB_2 and SiC (ZrB_2+20 SiC+4 Si_3N_4), decreases hardness to ~14 GPa. [25]

In this work, we will investigate the impact of Si_3N_4 addition on structure and properties of ZrSiBCN materials using structure modeling and ab-initio calculations. Previously, Houska et al. used computational methods to investigate atomic and electronic structure of ZrBCN. [28] They compared different compositions and characterized covalent and metallic bonding in these materials. They used rock-salt type Zr(N+C+B) solid-solutions as models to rationalize the high hardness observed in ZrBCN films.

Our exploration starts with the composition $Zr_{42}B_{32}C_8N_{18}$, a ternary mixture of ZrN, ZrB_2, and ZrC. This composition is close to the composition $Zr_{41}B_{30}C_8N_{19}$ of sputtered films, for which a hardness of 36 GPa has been measured. [8, 9] Varying the ZrN, ZrB_2, and Si_3N_4 phase content, we generate structure models via melt-quench and subsequent annealing techniques. We will show that formation of nm-sized ZrN and ZrB_2 nuclei happens even at the short time-scales of our computer simulation. We compute elastic moduli and Vickers hardness and highlight the impact of Si_3N_4 addition to ZrSiBCN materials.

Computational details:

Structures and energies of ZrSiBCN models and of crystalline reference phases are computed within density functional theory (DFT). [29-33] We use the Generalized Gradient Approximation (GGA) [34, 35] for electron exchange and correlation together with the Projector Augmented Wave (PAW) method. [36, 37] For optimizations and property calculations we use a cut-off of

350 eV for the expansion of the wave function into a plane wave basis set. Sampling of the Brillouin zone is done at the Γ-point for amorphous models and using appropriate meshes for all crystalline models.

We create structures of amorphous ZrSiBCN by a "melt-quench" approach, which is followed – for selected models – by a sequence of simulated annealing. For both melt-quench and the simulated annealing processes, we perform ab-initio molecular dynamic (aiMD) simulations under a canonical (NVT) ensemble. We use a time-step of 2 fs for integrating the equations of motion and control temperature via velocity rescaling. The velocity rescaling is performed at every time-step. To save computational costs, we reduce the cutoff energy to 205 eV during aiMD simulations. In the beginning of the melt-quench procedure, we place 100 atoms randomly into a box with a volume reflecting a mixture of the constituting phases ZrB_2, ZrN, ZrC, and Si_3N_4. Then we create a "liquid" state via simulation at 5000 K for 10 ps (5,000 time-steps) during which the system loses all memory of its initial configuration. This randomization is supported by the fact that atoms exchange more than 90 % of their nearest neighbors during this period. Subsequently, the ensemble is cooled to 3000 K within 20 ps, which corresponds to a cooling rate of 10^{14} Ks^{-1}. At 3000 K, the system is again equilibrated for 20 ps, after which it is cooled to 2000 K within 20 ps (cooling rate of $5 \cdot 10^{13}$ Ks^{-1}) and finally down to 300 K in 20 ps (cooling rate of $8.5 \cdot 10^{13}$ Ks^{-1}). The overall simulation time to generate a "melt-quench" structure in this study is almost two orders of magnitude (about 50 times) longer in Ref. [28]. The time-temperature sequence of the melt-quench process is displayed in Figure 1 (left). For each composition, we generate five independent models via the melt-quench procedure (total 65 models). All structures obtained after the melt-quench procedure are finally optimized (positions and cell parameters) by converging forces to 5 meV/Å and stresses below 1 kBar.

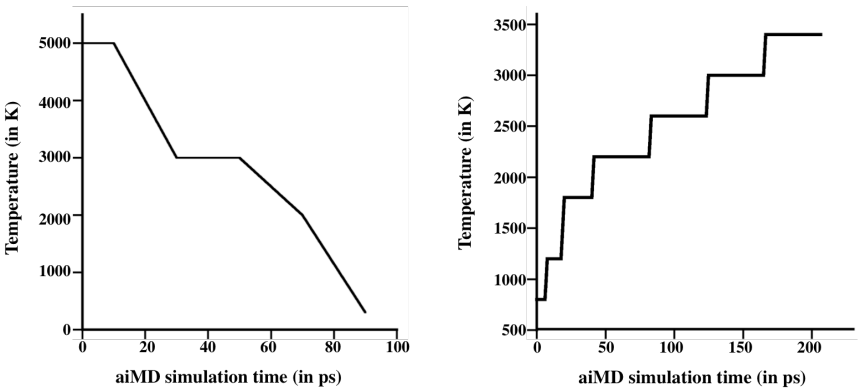

Figure 1: Time-temperature profile for (left) the aiMD melt-quench procedure and (right) for aiMD simulated annealing.

Simulated annealing starts after optimization of melt-quench models. For every composition, we choose the melt-quench model with lowest energy and simulate this at 800 K for 2 ps (total 13 models). Then we sequentially heat the model to 1200, 1800, 2200, 2600, 3000, and 3400 K using a heating rate of 2.5 $x10^{14}$ Ks^{-1}, while keeping the temperature constant for 5 to 20 ps once the desired temperature has been achieved. A graph with the temperature profile during simulated annealing is shown in Figure 1 (right). During the annealing procedure, we take a snapshot of the model every 2 ps and optimize the structure, while the annealing simulation continues. The optimized configurations track the underlying potential energy surface, above which the structure evolves at elevated temperatures. Moreover, since the annealing procedure effectively "heals" structural defects, we receive a sequence of models of which some have energies lower than the initial configurations. After a first complete annealing simulation, we choose the lowest energy model once again and repeat the annealing procedure all over. This is illustrated in Figure 2 for the model of $Zr_{27}Si_{15}B_{22}C_8N_{28}$. The figure on the left illustrates the first annealing process. The red dot shows the energy of the initial structure of this model of $Zr_{27}Si_{15}B_{22}C_8N_{28}$ as received after optimization of the melt quench model. Some healing of structural imperfections occurs during annealing at 1800 K, and a new "lowest energy structure" for the model is found. Further annealing during this run does not produce a lower energy structure, so the model is taken and, once again, subjected to a second annealing procedure.

During the second annealing procedure, for which longer "holding" times have been chosen (see Fig. 2 (right)), another drop in energy is observed. A third annealing process (not shown here) did not produce a model with even lower energy. In general, we consider a model being "converged" with respect to energy gains, if the maximum gain within annealing was less than 1 eV for 100 atoms (0.01 eV/atom).

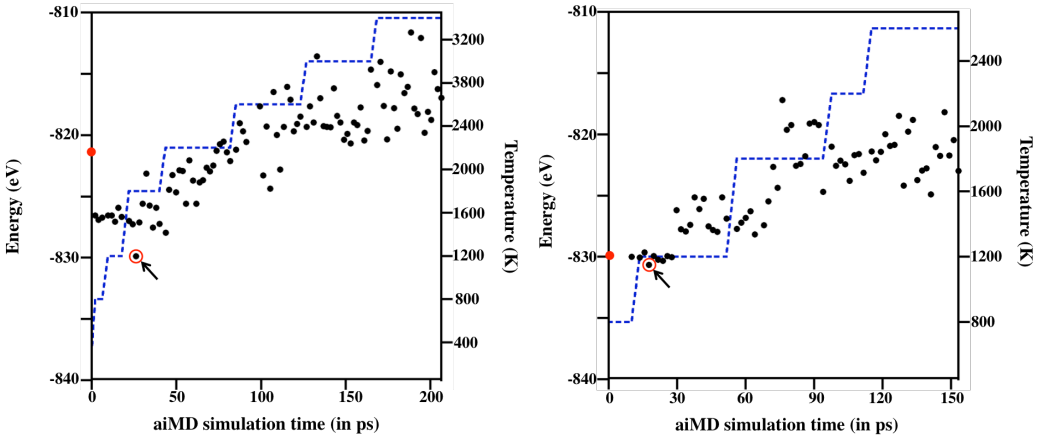

Figure 2: Energy landscapes for the model $Zr_{27}Si_{15}B_{22}C_8N_{28}$ computed in two simulated annealing processes. Both plots show on their left Y-axis the energy (in eV) and on their right Y-axis the temperature (in K) of the annealing process. Black dots correspond to energies of the optimized snapshots taken every 2 ps. The dashed blue line shows the temperature during the annealing, from which the snapshot was taken. (Left): First annealing. The red dot marks the initial energy of the model as obtained after aiMQ and optimization. Optimized snapshots taken during the annealing provide a sequence of models, some with lower energy than the initial state. The red circle and the black arrow mark the lowest energy model obtained during first annealing. (Right) Second annealing with longer holding times at each temperature. The red dot shows the energy of the starting configuration, as obtained from the first annealing. The red circle and the black arrow mark the lowest energy model obtained during second annealing. The energies converge initially and the structure is "stable". Overall, the second annealing process is slightly shorter in time to reduce computational costs.

We compute elastic constants c_{ij} via the strain-stress relationship given by Hooke's Law for all models, those received after the melt-quench procedure (5 for each composition) and for models with lowest energy obtained from the annealing procedure (1 for each composition). We estimate Bulk modulus (B), Young's modulus (E), and shear modulus (G) as well as Poisson's ratio for

each structure within the approximations of Voigt, Reuss and Hill. [38-40] We evaluate Vickers Hardness, H_V, using its empirical relation to B and G as proposed by Chen et al..[41]

Results:

a) Composition Diagram

We investigate ZrSiBCN structures with composition located in the quaternary ZrB_2-ZrN-ZrC-Si_3N_4 phase diagram. Every model comprises of 100 atoms. We compute mole coefficient and mole fraction (mol%) directly from composition, e.g. $Zr_{25}Si_{18}B_{16}C_8N_{33}$ == 8·ZrC + 9·ZrN + 8·ZrB_2 + 6·Si_3N_4 == 25.8 mol% ZrC + 29.0 mol% ZrN + 25.8 mol% ZrB_2 + 19.4 mol% Si_3N_4. We fix the amount of ZrC in all models (8 formula units of ZrC) and represent the composition of the remaining ZrB_2-ZrN-Si_3N_4 content in a ternary diagram (Figure 3). We acknowledge that this is not a perfect slice of the quaternary phase diagram, since the mol% of ZrC in the ZrSiBCN structures varies depending on the content of the other constituents. The small amount of ZrC is very helpful for structure simulations, because C may substitute for both N (in ZrN-like arrangements) and B (in ZrB_2-like fragments).

Starting from the "parent" composition of $Zr_{42}B_{30}C_8N_{18}$ ($Zr_{42}B_{32}C_8N_{18}$ == 8·ZrC + 18·ZrN + 16·ZrB_2), which is close to the experimentally realized composition of $Zr_{41}B_{30}C_8N_{19}$ – we adopt four different pathways (1) - (4) to incorporate Si_3N_4. These paths are indicated in the ternary composition diagram shown in Figure 3. Along each pathway we add units of Si_3N_4 to the model, while balancing the total number of atoms in a model (100) by changing the amount of ZrB_2 and ZrN. The net change along the four pathways is (1) + Si_3N_4 – ZrB_2 – 2 ZrN, (2) + 6 Si_3N_4 – 8 ZrB_2 – 9 ZrN, (3) + 2 Si_3N_4 – 4 ZrB_2 – ZrN, and (4) + Si_3N_4 – 3 ZrB_2 + ZrN. Path (1) is almost parallel to the ZrN-Si_3N_4 tie-line, while path (3) is approximately parallel to the ZrB_2-Si_3N_4 tie-line.

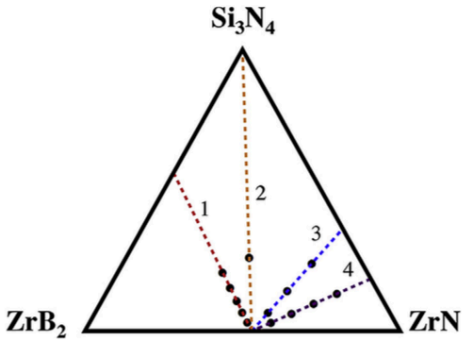

Figure 3: Ternary composition diagram for Zr-Si-B-C-N compounds (with constant ZrC amount). Lines originate from "parent" composition $Zr_{42}B_{30}C_8N_{18}$ and indicate pathways of incorporating Si_3N_4. Black dots represent compositions investigated in this study.

We generate five independent models for each composition via the melt-quench procedure, and subject the lowest-energy model of each composition to the simulated annealing procedure. From the annealing procedure we receive one more model for each composition. Hence, in total we analyze six models for each of the 13 compositions. For reference, we compute crystalline structures of ZrB_2, ZrC and ZrN (both NaCl-type), β-Si_3N_4, h-BN and c-BN.

b) Structure and Ordering:

Figure 4 shows four representative structures from each of the four pathways as obtained after two cycles of simulated annealing. It is difficult to provide simple quantitative measures for bonding in these mixed systems. However, we find average bond distances comparable with those computed for crystal structures. For instance, Zr-B (2.42 Å in the model; 2.54 Å in hexagonal ZrB_2), Zr-C (2.34 Å; 2.34 Å in c-ZrC), Zr-N (2.37 Å; 2.31 Å in c-ZrN), Si-N (1.77 Å; 1.75 Å in β-Si_3N_4), Si-C (1.81 Å; 1.86 Å in β-SiC), B-B (1.72 Å; 1.83 Å in hexagonal ZrB_2), and B-N (1.47 Å; 1.45 Å in h-BN). C-C, C-N, and N-N bonds do not appear in these models. We also find occasionally some Zr-Si bonds (2.79 Å; 2.72 Å in $ZrSi_2$).

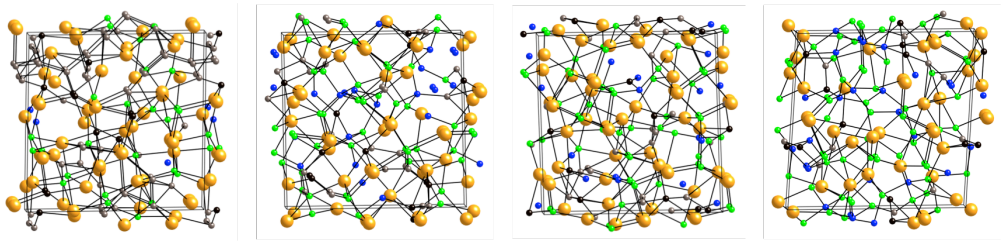

Figure 4: Representative models of amorphous ZrSiBCN structures obtained after two cycles of repeated annealing. From left to right the compositions are: $Zr_{39}Si_3B_{30}C_8N_{20}$ (3 mol% Si_3N_4), $Zr_{36}Si_6B_{28}C_8N_{22}$ (5 mol% of Si_3N_4), $Zr_{33}Si_9B_{26}C_8N_{24}$ (8 mol% Si_3N_4) and $Zr_{25}Si_{18}B_{16}C_8N_{33}$ (19 mol% of Si_3N_4). Large (orange) spheres represent Zr, small (green) N, small (blue) Si, small (brown) B, and small (black) C.

Simulated site-site distance pair correlation functions g(r) of two models – $Zr_{39}Si_3B_{30}C_8N_{20}$ (pathway (1) at 3 mol% Si_3N_4) and $Zr_{25}Si_{18}B_{16}C_8N_{33}$ (pathway (2) at 19 mol% Si_3N_4) shown in Figure 5 support our observations. In particular, partial g(r)'s show that both systems exhibit no C-C, C-N, or N-N bonding. Zr···Zr correlations at 3.2-3.3 Å are comparable to distances between Zr layers in hexagonal ZrB_2 (3.17 Å), c-ZrN (3.27 Å) and c-ZrC (3.30 Å).

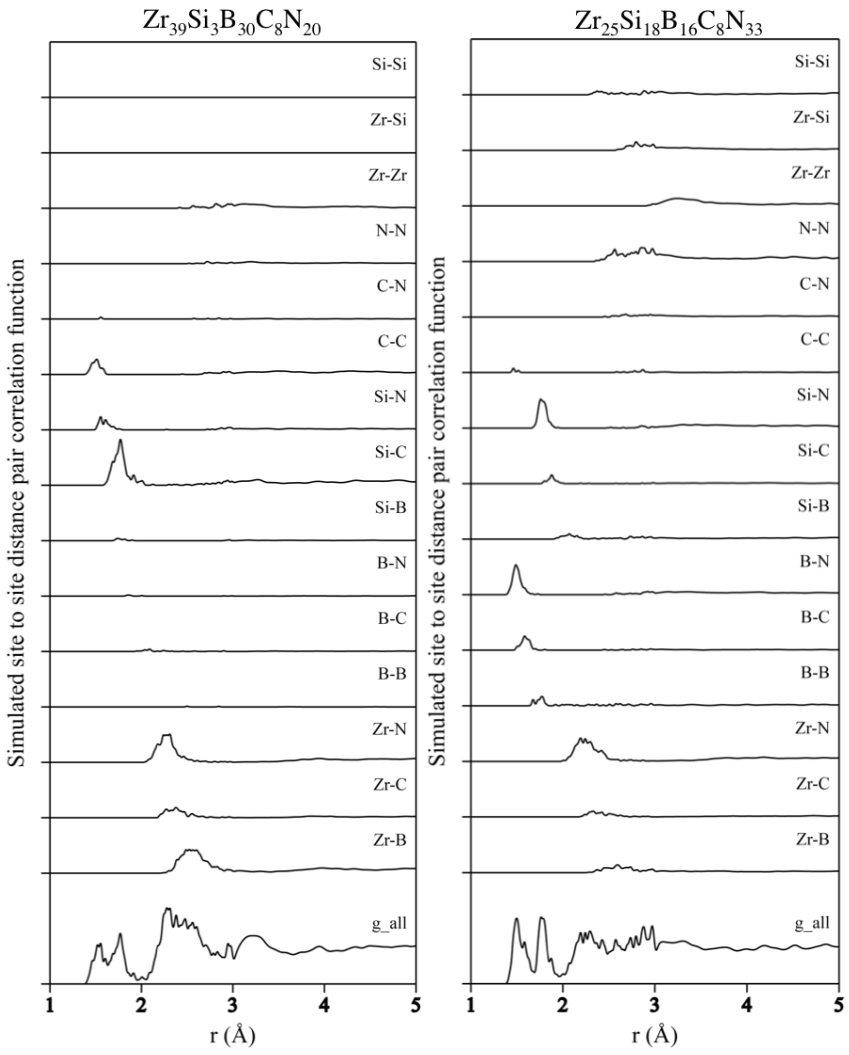

Figure 5: Simulated site-site distance pair correlation functions g(r) of $Zr_{39}Si_3B_{30}C_8N_{20}$ (pathway 1, composition 1, 3 mol% Si_3N_4) and $Zr_{25}Si_{18}B_{16}C_8N_{33}$ (pathway 2, composition 1, 19 mol% Si_3N_4).

We can characterize – qualitatively – the structural order that occurs in these Zr-Si-B-C-N models. Zr tends to arrange in layers, each layer resembling closest packing (cp) in a plane. Interstitials spaces between the layers are filled with N, C and B in such a way that Zr is, ideally, six-fold coordinated. These Zr-centered octahedra fuse together and form small nuclei of ZrN(C) (Figure 6, left). B atoms tend to aggregate in B-B networks forming rings like in the honeycomb B-substructure of ZrB_2, with Zr located above and below the rings (Figure 6, right). The ZrB_2 nuclei do not appear as frequent as ZrN(C) nuclei. These fragments and nuclei appear in melt-quench models and annealed models alike, with more pronounced order in the latter.

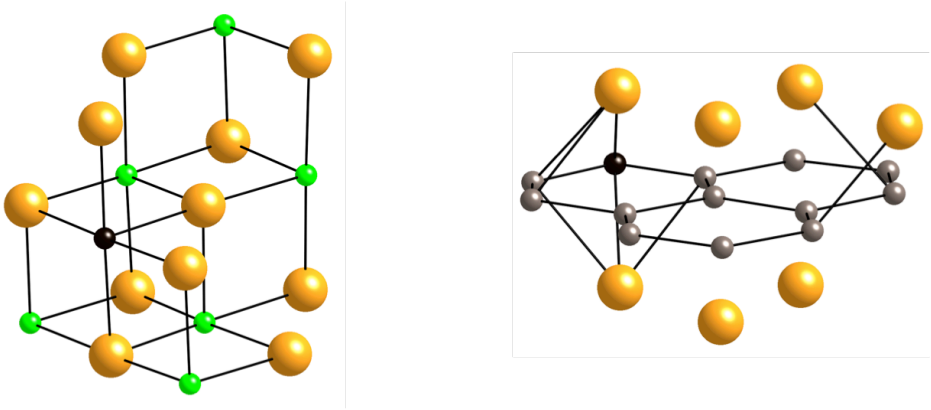

Figure 6: (left) ZrN(C) nucleus in $Zr_{39}Si_3B_{30}C_8N_{18}$ (pathway (1), 3 mol% Si_3N_4) (Right) Fused B_6-rings between Zr layers (right). Note that in both nuclei one C is substituting for N and B, respectively. Large (orange) spheres represent Zr, small (green) N, small (brown) B, and small (black) C.

The impact of increasing Si_3N_4 content is a decreasing tendency to form nuclei of any kind. For example, models with two and more units of Si_3N_4 are free of B_6-rings. Moreover, the number of Zr-centered octahedra fused together (size of ZrN(C) nuclei) decreases significantly as the Si_3N_4 content increases. Overall, structures containing Si_3N_4 are less ordered and exhibit a larger variety of local environments for all atoms.

c) Thermochemistry:

In Table 1 we show the computed enthalpy of formation of ZrSiBCN models. For each composition we only consider the model with the lowest energy. The enthalpy of formation is defined with reference to the crystal structures ZrN, ZrC, ZrB_2, and β-Si_3N_4, according to: $\Delta Hf = E(a\text{-}ZrSiBCN) - [m\cdot E(c - ZrB_2) + n\cdot E(c - ZrN) + p\cdot E(c - ZrC) + r\cdot E(\beta - Si_3N_4)/n_{atoms}$ where m, n, p and r stand for formula units(f.u.) of c-ZrB_2, c-ZrN, c-ZrC and β-Si_3N_4 respectively. Reference energies for the crystalline structures are:

c-ZrB_2 = -24.74 eV/f.u.; c-ZrC = -19.33 eV/f.u; c-ZrN = -20.23 eV/f.u.; β-Si_3N_4=-58.69 eV/f.u.

Overall, ΔH_f of these models is about 0.4-0.5 eV/atom with the exception of the parent model, $Zr_{42}B_{32}C_8N_{18}$, for which the enthalpy of formation is only half as high, 0.24 eV/atom. For amorphous Si_3N_4 itself, we find consistently a value of 0.2 – 0.3 eV/atom for the enthalpy of

formation, which parallels earlier investigations. [44, 45] Hence, the addition of Si_3N_4 to a phase assemblage of ZrB_2, ZrC, and ZrN significantly increases ΔH_f. This increase of ΔH_f parallels the observed decrease to form ordered nuclei with addition of Si_3N_4.

Pathway	Composition	Energy (eV/atom)	m	n	p	r	ΔH_f (eV/atom)
Parent	$Zr_{42}B_{32}C_8N_{18}$	-9.81	16	18	8	0	0.24
Pathway (1)	$Zr_{39}Si_3B_{30}C_8N_{20}$	-8.67	15	16	8	1	0.41
	$Zr_{36}Si_6B_{28}C_8N_{22}$	-8.57	14	14	8	2	0.45
	$Zr_{33}Si_9B_{26}C_8N_{24}$	-8.49	13	12	8	3	0.46
	$Zr_{30}Si_{12}B_{24}C_8N_{26}$	-8.40	12	10	8	4	0.48
	$Zr_{27}Si_{15}B_{22}C_8N_{28}$	-8.31	11	8	8	5	0.51
Pathway (2)	$Zr_{25}Si_{18}B_{16}C_8N_{33}$	-8.35	8	9	8	6	0.52
Pathway (3)	$Zr_{37}Si_6B_{24}C_8N_{25}$	-8.68	12	17	8	2	0.45
	$Zr_{32}Si_{12}B_{16}C_8N_{32}$	-8.63	8	16	8	4	0.48
	$Zr_{27}Si_{18}B_8C_8N_{39}$	-8.64	4	15	8	6	0.45
Pathway (4)	$Zr_{40}Si_3B_{26}C_8N_{23}$	-8.77	13	19	8	1	0.43
	$Zr_{38}Si_6B_{20}C_8N_{28}$	-8.86	10	20	8	2	0.38
	$Zr_{36}Si_9B_{14}C_8N_{33}$	-8.87	7	21	8	3	0.42

	$Zr_{34}Si_{12}B_8C_8N_{38}$	-8.91	4	22	8	4	0.43

Table 1: Enthalpy of formation (ΔH_f) of a-ZrSiBCN with respect to crystalline phases (ZrB_2, ZrN, ZrC and β-Si_3N_4). For each composition only the model with lowest energy was considered.

c) Elastic Moduli and Vickers hardness:

Elastic constants c_{ij} (there are 21 independent elements of c_{ij} for each model, since the structures do not possess any symmetry) are computed for all ZrSiBCN models, six for each composition. The stiffness matrix (c_{ij}) of an isotropic model comprises three independent values only, since $c_{11} = c_{22} = c_{33}$, $c_{44} = c_{55} = c_{66}$, $c_{12} = c_{23} = c_{13}$, and all remaining elements vanish. [46] This is not fulfilled for individual models we constructed, most likely because their size is not large enough to be "isotropic". However, averaging c_{ij} for models of the same composition yields isotropic behavior within the margin of error. A representative average stiffness matrix, for composition $Zr_{39}Si_3B_{30}C_8N_{20}$, is shown in Table 2:

c_{ij}	1	2	3	4	5	6
1	266 ± 14	137 ± 9	118 ± 5	-20 ± 17	13 ± 13	5 ± 6
2	137 ± 9	258 ± 7	114 ± 9	10 ± 11	-17 ± 7	-7 ± 5
3	118 ± 5	114 ± 9	265 ± 15	-11 ± 9	12 ± 9	6 ± 3
4	-20 ± 17	10 ± 11	-11 ± 9	61 ± 16	19 ± 14	4 ± 5
5	13 ± 13	-17 ± 7	12 ± 9	19 ± 14	58 ± 10	0 ± 6
6	5 ± 6	-7 ± 5	6 ± 3	4 ± 5	0 ± 6	82 ± 4

Table 2: Stiffness matrix [6x6] of $Zr_{39}Si_3B_{30}C_8N_{20}$ averaged over 5 independent melt-quench models. For each entry of c_{ij} we list the value together with the standard error. The minimum and maximum standard errors are 3 and 16 GPa, respectively, with an average of 9 GPa.

Using the stiffness (c_{ij}) and compliance (s_{ij}) matrices, we compute the elastic moduli B, G and E using the Voigt, Reuss and Hill (V-R-H) approach. [38-40] Voigt's method yields an upper boundary for an elastic modulus: bulk modulus $B_V = (1/9)[(c_{11} + c_{22} + c_{33}) + 2(c_{12} + c_{13} + c_{23})]$ and shear modulus $G_V = (1/15)[(c_{11} + c_{22} + c_{33}) - (c_{12} + c_13 + c_{23}) + 3(c_{44} + c_{55} + c_{66})$. Reuss's method provides a lower bound of an elastic modulus: $B_R = [(s_{11} + s_{22} + s_{33}) + 2(s_{12} + s_{13} + s_{23})]^{-1}$ and $G_R = 15\,[4(s_{11} + s_{22} + s_{33}) - (s_{12} + s_{13} + s_{23}) + 3(s_{44} + s_{55} + s_{66})]^{-1}$. The Hill method gives an average of the upper and lower bounds as $B_H = (1/2)\,[B_V + B_R]$ and $G_H = (1/2)[G_V + G_R]$. The Young's modulus (E) is related to the bulk (B) and shear (G) moduli as $E = 9BG/(3B + G)$, and our estimate of E is based on the aggregate Hill values of B and G. For a given composition the moduli can be determined either by first averaging the c_{ij} and computing moduli from the averaged stiffness matrix or alternatively by first computing moduli for each model and then averaging the moduli for each composition. We choose the latter approach, since it provides us a simple error estimate of each modulus based on its average and its variation (in comparison to the requirement to do a full error propagation from stiffness coefficients). Vickers hardness (H_V) is estimated using the empirical relation between hardness and elastic moduli as proposed by Chen: $H_V = 2\,(G^3/B^2)^{0.585} - 3$. [41].

In Table 3, we summarize results of elastic moduli and hardness (H_V) for crystalline structures, the parent composition $Zr_{42}B_{30}C_8N_{18}$ and for ZrSiBCN models. There is reasonable agreement between our computed data with references in literature. For example, experimental data for the independent elastic constants of hexagonal ZrB_2 (space group: P6/mmm) are c_{11}=581 GPa, c_{12}=55 GPa, c_{13}=121 GPa, c_{33}=445 GPa, and c_{44}=240 GPa. [47] This yields B, G, E of 244 GPa, 233 GPa, and 530 GPa, respectively, within the V-R-H approximation. Our computed moduli for ZrB_2 are 247 GPa, 214 GPa, and 499 GPa, for B, G, and E, respectively, with a deviation of less than 10% from the experimental data. For crystalline ZrC, we compute moduli

B and G to 236 GPa and 146 GPa, respectively, which provides an estimate of 18 GPa for H_V. This is in close agreement with recent computational data (B = 234 GPa, G = 164 GPa, Hv = 23 GPa, [48]), and differences arise only from the use of different pseudopotentials and cut-offs ($E_{cut\text{-}off}$ = 350 eV against 560 eV in reference [48]). Experimental values of B for ZrC, which depend on the measurement technique and sample microstructure, range between 207 and 223 GPa. [49, 50] Our computed elastic moduli of ZrN are B = 268 GPa, G = 195 GPa, and E = 470 GPa, somewhat larger than recent computational data (B = 245 GPa, G = 150 GPa, E = 375 GPa) [51]. From nano-indentation measurements, the elastic constants for β-Si_3N_4 are determined to be: c_{11} = 343 GPa, c_{12} = 136 GPa, c_{13} = 120 GPa, c_{33} = 600 GPa and c_{44} = 124 GPa. [52] Accordingly, the elastic moduli from V-R-H approximations are B = 227 GPa, G = 120 GPa, E = 307 GPa and H_V = 13 GPa. Computational data in reference [53] for β-Si_3N_4 yields values of B = 225 GPa and G = 120 GPa. [53] Comparison of these values with our computed values listed in Table 3 for β-Si_3N_4 (B = 236 GPa, G = 126 GPa, E = 313 GPa) shows good agreement. [53] For the parent composition a-$Zr_{42}B_{30}C_8N_{18}$, we compute B, G, E, and H_V of 171, 79, 206, and 8 GPa, respectively.

In Figure 7 we plot bulk modulus B, shear modulus G, Young's modulus E and Vickers hardness H_V as a function of Si_3N_4 content (mol-% of Si_3N_4) along the selected pathways of the composition diagram (see Fig. 3).

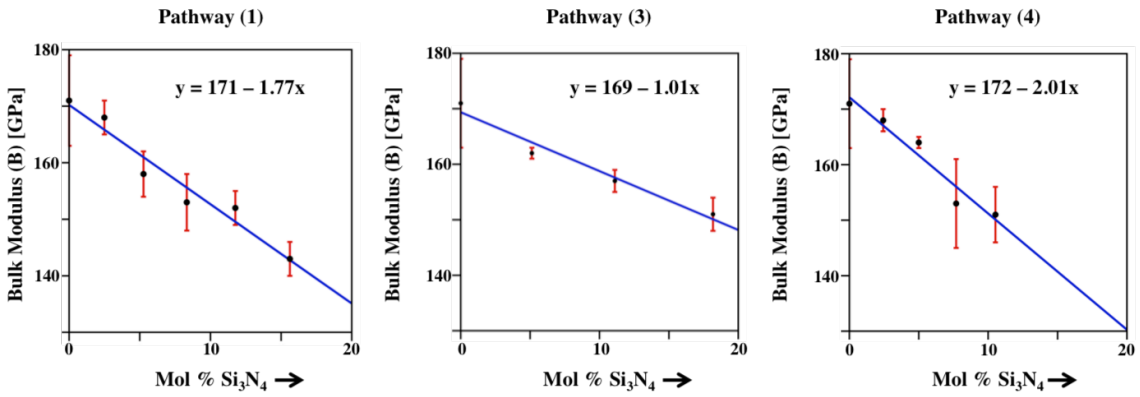

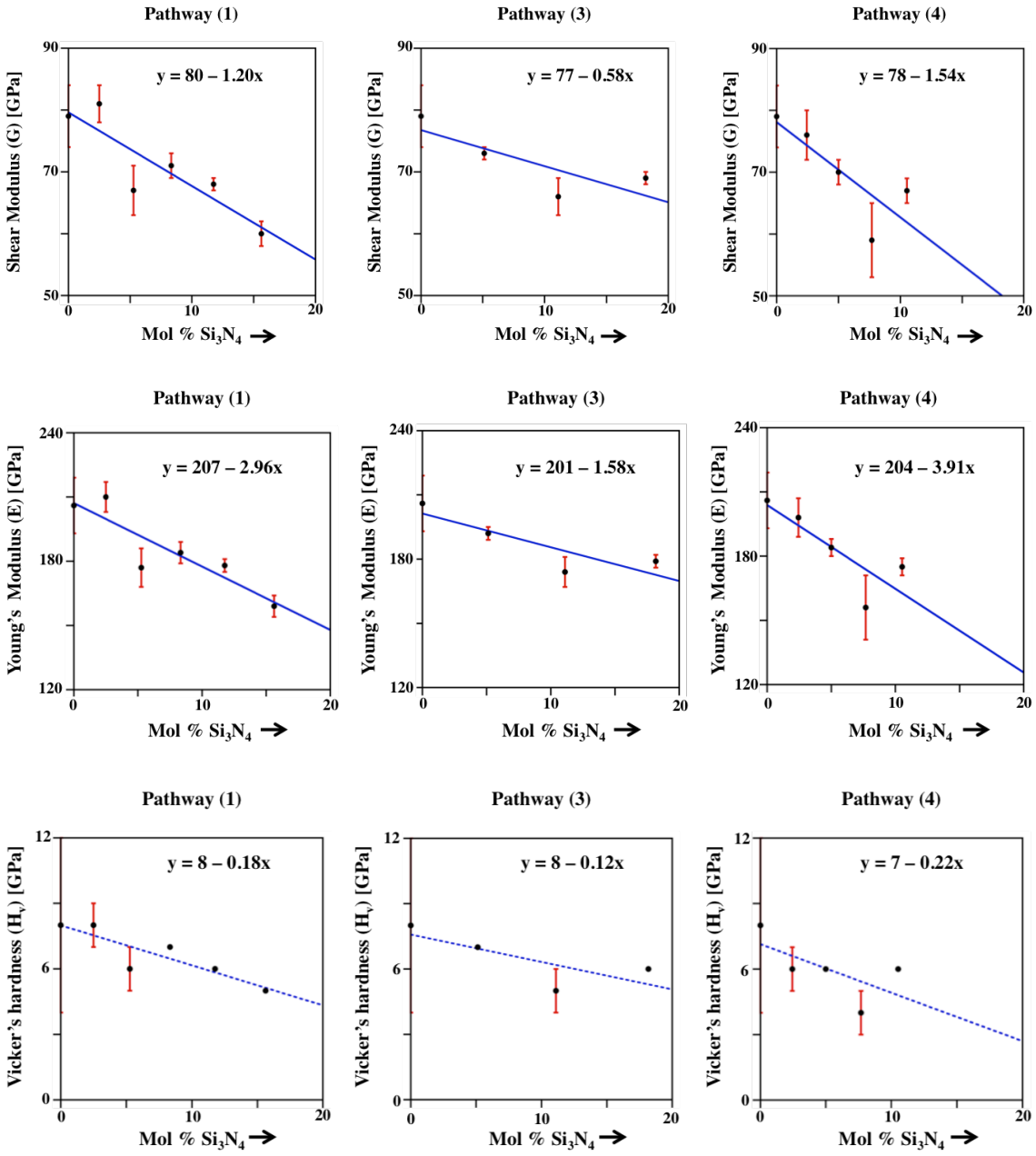

Figure 7: Average elastic moduli – bulk moduli B (top), shear moduli G (top-middle) E (bottom-middle) and Vickers hardness H_V (bottom) – of ZrSiBCN plotted as a function of mol-% Si_3N_4 along pathway (1), (3) and (4) of the composition diagram shown in Fig. 3. The lines in each diagram are linear fits to the data. Error bars in each figure depict computed standard error. The standard errors computed for Vickers hardness of some ZrSiBCN compositions are small and hence not visible in the scale of the graph.

Linear fits to the data in Figure 7 show a decrease of elastic moduli and hardness with increasing Si_3N_4-content. For instance, addition of 1 mol-% of Si_3N_4 to compositions along pathway (1),

decreases the bulk modulus by 1.8 GPa. For pathway (3) and (4) the decrease in B is 1.0 GPa and 2.0 GPa per mol % Si_3N_4 added, respectively. For shear modulus (G) the decrease per mol-% Si_3N_4 is 1.2 GPa for pathway (1), 0.6 GPa for pathway (3) and 1.5 GPa for pathway (4). The decrease in Young's modulus (E) is ~ 3.0, 1.6 and 4.0 GPa along pathway (1), (3) and (4) respectively. However, Vickers hardness (H_V) drops only slightly (by ~ 0.2 GPa per mol-% Si_3N_4) along each pathway, since the estimate by Chen strongly correlates H_V to the ratio of B and G. Overall, starting from the initial composition $Zr_{42}B_{30}C_8N_{18}$, an increase of Si_3N_4 content in the ZrSiBCN models results in a decrease of elastic moduli B and G and, ultimately, of Vickers hardness. A decrease in G, E, and H_V (but not in B) can be expected from a simple mixture model applied to the addition of Si_3N_4 to a phase assemblage of ZrB_2, ZrC, and ZrN. However, we show in next paragraph that effect is larger than expected and that the moduli are impacted additionally by the reduced structural order (as discussed in the previous section).

Along pathway (1) a simple mixture model of $Zr_{42}B_{30}C_8N_{18}$ based on mole fractions of crystalline ZrN, ZrC, ZrB_2 and Si_3N_4 and moduli of crystalline structures given in Table 3 predicts moduli of 254 GPa, 193 GPa, and 461 GPa, for B, G, and E, respectively. Computed values are 171, 79, and 208 GPa, for B, G, and E, respectively. For the model with largest Si_3N_4 content, $Zr_{27}Si_{15}B_{22}C_8N_{28}$, a mixture model yields 198, 102, and 343 GPa, and the computation gives 143, 60, and 159 GPa, for B, G, and E, respectively. Thus, computed models have significantly lower moduli than expected by a mixture model. If data of amorphous a-Si_3N_4 (either from computed models, or using reported experimental data of B = 196 GPa [44] and E = 289 GPa [53]) is used to predict the "ideal" moduli for these compositions, the discrepancy is still significant. More importantly, the deviation from an ideal mixture model increases with Si_3N_4 content along all pathways. We note that along pathway (1), (2) and (3) addition of Si_3N_4 happens at the expense of ZrN, while the ZrB_2 content remains almost constant. On the other hand, along pathway (4) Si_3N_4 is added at the expense of ZrB_2, and the ZrN content increases slightly. Along both paths we observe significant decrease of local order with increase of Si_3N_4 content. Therefore, for these

ZrSiBCN models a decrease of elastic moduli correlates with a decrease in structural order, which in turn goes along with an increase of Si_3N_4 content.

	Composition	Bulk Modulus (GPa)	Shear Modulus (GPa)	Young's Modulus (GPa)	Vickers Hardness (GPa)
Crystalline phases	c-ZrB_2	247	214	499	36
	c-ZrN	268	195	470	27
	c-ZrC	236	146	364	18
	β–Si_3N_4	236	126	313	13
Parent	$Zr_{42}B_{30}C_8N_{18}$	171 ± 8	79 ± 5	206 ± 13	8 ± 4
Pathway (1)	$Zr_{39}Si_3B_{30}C_8N_{20}$	190 ± 22	86 ± 4	225 ± 11	8 ± 1
	$Zr_{36}Si_6B_{28}C_8N_{22}$	158 ± 4	67 ± 4	177 ± 9	6 ± 1
	$Zr_{33}Si_9B_{26}C_8N_{24}$	153 ± 5	71 ± 2	184 ± 5	7 ± 0
	$Zr_{30}Si_{12}B_{24}C_8N_{26}$	152 ± 3	68 ± 1	178 ± 3	6 ± 0
	$Zr_{27}Si_{15}B_{22}C_8N_{28}$	143 ± 3	60 ± 2	159 ± 5	5 ± 0
Pathway (2)	$Zr_{25}Si_{18}B_{16}C_8N_{33}$	144 ± 4	59 ± 3	157 ± 8	5 ± 1
Pathway (3)	$Zr_{37}Si_6B_{24}C_8N_{25}$	162 ± 1	73 ± 1	192 ± 3	7 ± 0
	$Zr_{32}Si_{12}B_{16}C_8N_{32}$	157 ± 2	66 ± 3	174 ± 7	5 ± 1
	$Zr_{27}Si_{18}B_8C_8N_{39}$	151 ± 3	69 ± 1	179 ± 3	6 ± 0
Pathway	$Zr_{40}Si_3B_{26}C_8N_{23}$	168 ± 2	76 ± 4	198 ± 9	6 ± 1

(4)	$Zr_{38}Si_6B_{20}C_8N_{28}$	164 ± 1	70 ± 2	184 ± 4	6 ± 0
	$Zr_{36}Si_9B_{14}C_8N_{33}$	153 ± 8	59 ± 6	156 ± 15	4 ± 1
	$Zr_{34}Si_{12}B_8C_8N_{38}$	151 ± 5	67 ± 2	175 ± 4	6 ± 0

Table 3: Computed B, G, and E and Vickers Hardness of crystalline ZrB_2, ZrC, ZrN, and Si_3N_4 and of amorphous ZrSiBCN models. For amorphous models the error given refers to the standard error obtained from averaging moduli of individual models.

Conclusion

In this work, we model amorphous ZrSiBCN ceramics, which are candidates for high temperature coating materials. Using melt-quench and simulated annealing techniques together with ab-initio molecular dynamic simulations, we generate mixtures of ZrB_2, ZrN, ZrC and Si_3N_4 each model comprising 100 atoms. Starting from the parent composition $Zr_{42}B_{30}C_8N_{18}$ we follow four different pathways along which Si_3N_4 can be included. Models we receive exhibit Zr layers as well as ZrB_2 and ZrN(C) nuclei. We observe, qualitatively, that structural order depends on the amount of Si_3N_4 content in the system: the more Si_3N_4 the lower the order. Thermochemical calculations yield an enthalpy of formation (ΔH_f) of = 0.4 – 0.5 eV/atom for the ZrSiBCN models. We compute independent elastic constants and from those elastic moduli (B, G and E) within the V-R-H approximations. Along each pathway, we observe decrease of B, G, E and H_V with increasing Si_3N_4 content. Values for B, G, E and H_V are lower than expectations from a simple mixture model, indicating additional impact of reduced structural order upon Si_3N_4 addition.

Consequently, while addition of Si_3N_4 to amorphous ZrBCN coating materials may improve the materials' oxidation resistance, the computations show that Si_3N_4 also impacts mechanic performance of the coatings. Most notably, we show that a significant effect arises via reduction in structural order. While sputtered ZrBCN coatings show nano-domain structure with substantial proportion of nano-grains, we expect that addition of Si_3N_4 impedes the formation of

nuclei and nano-grains and increases disorder in the films. Thus, the engineers' choice will be a balance between desired oxidation resistance and target mechanical properties.

Acknowledgements

This work was supported by the National Science Foundation [grant number CMMI-1335502]. The computational work was made possible through generous grants by the Texas Advance Computing Center in Austin, TACC, Texas, and by the High Performance Computing facilities at UTA.

References:

[1] E. Wuchina, E. Opila, M. Opeka, W. Fahrenholtz, I. Talmy, The Electrochemical Society Interface, 16 (2007) 30.

[2] W.G. Fahrenholtz, E.J. Wuchina, W.E. Lee, Y. Zhou, Ultra-high temperature ceramics: materials for extreme environment applications, John Wiley & Sons, 2014.

[3] K. Upadhya, J.M. Yang, W.P. Hoffman, Am Ceram Soc Bull, 76 (1997) 51-56.

[4] W.G. Fahrenholtz, G.E. Hilmas, I.G. Talmy, J.A. Zaykoski, J Am Ceram Soc, 90 (2007) 1347-1364.

[5] K. Tanabe, H. Asano, Y. Katoh, O. Michikami, Jpn J Appl Phys 2, 26 (1987) L570-L572.

[6] J.W. Sung, D.M. Goedde, G.S. Girolami, J.R. Abelson, J Appl Phys, 91 (2002) 3904-3911.

[7] Y.G. Wang, Q.M. Liu, J.L. Liu, L.T. Zhang, L.F. Cheng, J Am Ceram Soc, 91 (2008) 1249-1252.

[8] M. Zhang, J. Jiang, J. Vlček, P. Steidl, J. Kohout, R. Cerstvy, E.I. Meletis, Microscopy and Microanalysis, 20 (2014) 1892-1893.

[9] M. Zhang, J. Jiang, J. Houska, J. Kohout, J. Vlcek, E.I. Meletis, Acta Mater., 77 (2014) 212-222.

[10] S.R. Levine, E.J. Opila, M.C. Halbig, J.D. Kiser, M. Singh, J.A. Salem, J Eur Ceram Soc, 22 (2002) 2757-2767.

[11] W.C. Tripp, H.C. Graham, J Electrochem Soc, 118 (1971) 1195-&.

[12] Berkowit.Jb, J Electrochem Soc, 113 (1966) 908-&.

[13] M. Singh, H. Wiedemeier, J Am Ceram Soc, 74 (1991) 724-727.

[14] K.R. Janowski, R.D. Carnahan, Jom-J Min Met Mat S, 17 (1965) 1042-&.

[15] E.I. Golovko, R.F. Voitovich, Zh Fiz Khim+, 56 (1982) 2063-2065.

[16] M. Caillet, H.F. Ayedi, J. Besson, Journal of the Less Common Metals, 51 (1977) 323-331.

[17] E.J. Opila, N.S. Jacobson, Materials Science and Technology.

[18] F. Monteverde, A. Bellosi, Scripta Mater, 46 (2002) 223-228.

[19] F. Monteverde, A. Bellosi, Solid State Sci, 7 (2005) 622-630.

[20] A.L. Chamberlain, W.G. Fahrenholtz, G.E. Hilmas, J Am Ceram Soc, 89 (2006) 3638-3645.

[21] I.G. Talmy, J.A. Zaykoski, M.M. Opeka, J Am Ceram Soc, 91 (2008) 2250-2257.

[22] W.H. Rhodes, E.V. Clougherty, D. Kalish, Other Information: UNCL. Orig. Receipt Date: 30-JUN-73, 1970.

[23] E.W. Neuman, G.E. Hilmas, W.G. Fahrenholtz, J Am Ceram Soc, 96 (2013) 47-50.

[24] E.W. Neuman, G.E. Hilmas, W.G. Fahrenholtz, J Eur Ceram Soc, 35 (2015) 463-476.

[25] F. Monteverde, S. Guicciardi, A. Bellosi, Mat Sci Eng a-Struct, 346 (2003) 310-319.

[26] A.L. Chamberlain, W.G. Fahrenholtz, G.E. Hilmas, D.T. Ellerby, J Am Ceram Soc, 87 (2004) 1170-1172.

[27] J. Watts, G. Hilmas, W.G. Fahrenholtz, J Am Ceram Soc, 94 (2011) 4410-4418.

[28] J. Houska, J. Kohout, J. Vlcek, Thin Solid Films, 542 (2013) 225-231.

[29] P. Hohenberg, W. Kohn, Physical Review, 136 (1964) B864-B871.

[30] G. Kresse, J. Hafner, Physical Review B, 47 (1993) 558-561.

[31] G. Kresse, J. Hafner, Physical Review B, 49 (1994) 14251-14269.

[32] G. Kresse, J. Furthmüller, Physical Review B, 54 (1996) 11169-11186.

[33] G. Kresse, J. Furthmüller, Computational Materials Science, 6 (1996) 15-50.

[34] J.P. Perdew, K. Burke, M. Ernzerhof, Physical Review Letters, 77 (1996) 3865-3868.

[35] J.P. Perdew, K. Burke, M. Ernzerhof, Physical Review Letters, 78 (1997) 1396-1396.

[36] P.E. Blöchl, Physical Review B, 50 (1994) 17953-17979.

[37] G. Kresse, D. Joubert, Physical Review B, 59 (1999) 1758-1775.

[38] W. Voigt, Lehrbuch der Kristallphysik, B. B. Teubner, Leipzig, 1928.

[39] A. Reuss, ZAMM - Journal of Applied Mathematics and Mechanics / Zeitschrift für Angewandte Mathematik und Mechanik, 9 (1929) 49-58.

[40] R. Hill, Proceedings of the Physical Society. Section A, 65 (1952) 349.

[41] X.Q. Chen, H.Y. Niu, D.Z. Li, Y.Y. Li, Intermetallics, 19 (2011) 1275-1281.

[42] D.R. Clarke, Surf Coat Tech, 163 (2003) 67-74.

[43] P. Giannozzi, S. Baroni, J Chem Phys, 100 (1994) 8537-8539.

[44] P. Kroll, J Eur Ceram Soc, 25 (2005) 163-174.

[45] P. Kroll, Journal of Non-Crystalline Solids, 351 (2005) 1127-1132.

[46] J.F. Nye, Physical Properties of Crystals Oxford Univ. Press, New York, 1957.

[47] N.L. Okamoto, M. Kusakari, K. Tanaka, H. Inui, M. Yamaguchi, S. Otani, J Appl Phys, 93 (2003) 88-93.

[48] C.W. Xie, A.R. Oganov, D. Li, T.T. Debela, N. Liu, D. Dong, Q.F. Zeng, Phys Chem Chem Phys, 18 (2016) 12299-12306.

[49] H. O.Pierson, Handbook of Refractory Carbides & Nitrides: Properties, Characteristics, Processing and Apps., Noyes Publication, 1996.

[50] R. Chang, L.J. Graham, J Appl Phys, 37 (1966) 3778-&.

[51] V.I. Ivashchenko, P.E.A. Turchi, V.I. Shevchenko, J Phys-Condens Mat, 21 (2009).

[52] J.C. Hay, E.Y. Sun, G.M. Pharr, P.F. Becher, K.B. Alexander, J Am Ceram Soc, 81 (1998) 2661-2669.

[53] A. Khan, J. Philip, P. Hess, J Appl Phys, 95 (2004) 1667-1672.

[54] J.W. Lawson, M.S. Daw, C.W. Bauschlicher, J Appl Phys, 110 (2011).

[55] N. Hirosaki, Y. Okamoto, M. Ando, F. Munakata, Y. Akimune, J Ceram Soc Jpn, 104 (1996) 49-53.

[56] J. Houska, P. Steidl, J. Vlcek, J. Martan, Ceram Int, 42 (2016) 4361-4369.

[57] A.L. Ortiz, V. Zamora, F. Rodriguez-Rojas, Ceram Int, 38 (2012) 2857-2863.

[58] H.G. Smith, N. Wakabayashi, M. Mostoller, Phonon Anomalies in Transition Metals, Alloys and Compounds, in: D.H. Douglass (Ed.) Superconductivity in d- and f-Band Metals: Second Rochester Conference, Springer US, Boston, MA, 1976, pp. 223-249.

[59] P.T. Jochym, K. Parlinski, Eur Phys J B, 15 (2000) 265-268.

[60] L.H. Liu, C.J. Liu, S.Y. Yang, Z.J. Zhang, W. Gao, Z.M. Xie, Chinese J Polym Sci, 21 (2003) 99-101.

[61] S.D. Gupta, S.K. Gupta, P.K. Jha, Journal of Thermal Analysis and Calorimetry, 107 (2012) 49-53.

[62] N. Wada, S.A. Solin, J. Wong, S. Prochazka, Journal of Non-Crystalline Solids, 43 (1981) 7-15.

[63] Y.Q. Cai, L.T. Zhang, Q.F. Zeng, L.F. Cheng, Y.D. Xu, Physical Review B, 74 (2006).

[64] X.J. Wang, Y. Xie, Q.X. Guo, Chem Commun, (2003) 2688-2689.

[65] R. Geick, C.H. Perry, Rupprech.G, Physical Review, 146 (1966) 543-&.

[66] S.Y. Shapoval, V.T. Petrashov, O.A. Popov, A.O. Westner, M.D. Yoder, C.K.C. Lok, Appl Phys Lett, 57 (1990) 1885-1886.

[67] K. Inagawa, K. Watanabe, H. Ohsone, K. Saitoh, A. Itoh, J Vac Sci Technol A, 5 (1987) 2696-2700.

Appendix 2:

In this section I include some more computations – done with the ZrSiBCN models. These computations were initially planned to bea part of the published manuscript. However, due to length issues with the journal, they were omitted. The language is in plural – to include contributions of other authors to the work.

A2.1) Thermal conductivity:

Lattice thermal conductivities of ZrSiBCN are computed using Clarke's model that computes the minimum thermal conductivity of materials above their Debye temperature. According to this model:

$$\kappa_{\min} = 0.87 k_B N_A^{2/3} \frac{m^{2/3} \rho^{1/6} E^{1/2}}{M^{2/3}}$$

where: E is Young's modulus, M is the mass, m is the number of atoms in the system, k_B is the Boltzmann constant and N_A is the Avogadro's number. The minimum phonon mean free path is assumed to be the cube root of the volume of the system and the mean phonon velocity includes only the acoustic modes. [1] Results are included in Table 3 along with thermal conductivity for the crystalline phases. The Clarke's model clearly has its limitation, as can be seen by comparing estimated κ_{min} with other computational data or experimental results. For example, Lawson et al. report thermal conductivity (κ) of 18 $Wm^{-1}K^{-1}$ at 1000 K for ZrB_2 from atomistic Green Kubo simulations. [2] For β-Si_3N_4, an experimental value of κ = 28 $Wm^{-1}K^{-1}$ at 1400 K has been reported. [3] Nevertheless, within these limitations we compute κ_{min} of $Zr_{42}B_{30}C_8N_{18}$ to 4.1 $Wm^{-1}K^{-1}$, which is close to the measured value of 7.3 W/mK at 394 K for $Zr_{41}B_{30}C_8N_{19}$. [4] We then find that adding Si_3N_4 has no significant impact on κ_{min}, as we consistently estimate κ_{min} ~ 4.0 $Wm^{-1}K^{-1}$. From the Clarke's formula it is expected that a decrease in Young's modulus and density lead to decrease in κ_{min} while a decrease in mean atomic mass (M/m) increase κ_{min}. In our ZrSiBCN models, the Young's modulus decreases along the selected pathways (see Figure 7)

and so does the mean atomic mass (M/m) due to intermixing atoms of different atomic mass. Thus, upon increasing Si_3N_4 content a decrease in Young's modulus is compensated by a decrease in mean atomic mass (M/m) resulting in a constant value of κ_{min}.

	Composition	Young's Modulus (GPa)	Thermal Conductivity κ_{min} ($Wm^{-1}K^{-1}$)
Crystalline phases	c-ZrB_2	499	2.30
	c-ZrN	470	2.59
	c-ZrC	364	1.61
	β–Si_3N_4	313	2.48
Parent	$Zr_{42}B_{30}C_8N_{18}$	206 ± 13	4.06 ± 0.02
Pathway (1)	$Zr_{39}Si_3B_{30}C_8N_{20}$	225 ± 11	4.4 ± 0.1
	$Zr_{36}Si_6B_{28}C_8N_{22}$	177 ± 9	4.10 ± 0.04
	$Zr_{33}Si_9B_{26}C_8N_{24}$	184 ± 5	4.17 ± 0.06
	$Zr_{30}Si_{12}B_{24}C_8N_{26}$	178 ± 3	4.21 ± 0.04
	$Zr_{27}Si_{15}B_{22}C_8N_{28}$	159 ± 5	4.07 ± 0.06
Pathway (2)	$Zr_{25}Si_{18}B_{16}C_8N_{33}$	157 ± 8	4.09 ± 0.08
Pathway (3)	$Zr_{37}Si_6B_{24}C_8N_{25}$	192 ± 3	4.12 ± 0.03
	$Zr_{32}Si_{12}B_{16}C_8N_{32}$	174 ± 7	4.06 ± 0.09
	$Zr_{27}Si_{18}B_8C_8N_{39}$	179 ± 3	4.26 ± 0.03

Pathway (4)	$Zr_{40}Si_3B_{26}C_8N_{23}$	198 ± 9	4.09 ± 0.09
	$Zr_{38}Si_6B_{20}C_8N_{28}$	184 ± 4	3.98 ± 0.05
	$Zr_{36}Si_9B_{14}C_8N_{33}$	156 ± 15	3.7 ± 0.2
	$Zr_{34}Si_{12}B_8C_8N_{38}$	175 ± 4	3.97 ± 0.05

Table A2.1: Computed Young's modulus (E) and κ_{min} of crystalline ZrB_2, ZrC, ZrN, and β-Si_3N_4 and of amorphous ZrSiBCN models. For amorphous models the error given refers to the standard error obtained from averaging moduli of individual models.

A2.2) IR spectra:

In Fig. A2.1 we show the computed IR spectra of crystalline ZrB_2, ZrC, ZrN and β-Si_3N_4. ZrB_2 has two IR active modes at 454 cm^{-1} and 479 cm^{-1}. Experimental data shows evidence of a peak at ~500 cm^{-1}. [5] ZrC and ZrN exhibit peaks at 225 cm^{-1} and 512 cm^{-1}, respectively. For ZrC, the peak at 225 cm^{-1} is in good agreement with phonon modes of ZrC crystals obtained from a normal mode analysis [6] or by ab initio lattice dynamics calculations. [7] Experimentally, ZrN based ceramics derived from for organometallic precursors show Zr-N vibrations at 469 cm^{-1}. [8] First principles calculations of the phonon density of states for ZrN shows Zr-N vibrations at ~500 cm^{-1}. [9] The IR spectra of β-Si_3N_4 are more complicated and show 6 IR-active modes. The low frequency modes at 360 cm^{-1}, 420 cm^{-1} and 556 cm^{-1} are in agreement with experimental IR spectra (380 cm^{-1}, 447 cm^{-1} and 580 cm^{-1}) by Wada et al. [10] and computational data (378 cm^{-1}, 424 cm^{-1} and 562 cm^{-1}) by Cai et al.. [11] The high frequency IR modes at 816 and 873 cm^{-1} differ significantly from the experimental modes at 910 and 985 cm^{-1}. However, our data is consistent with computed IR of β-Si_3N_4 – 848 and 886 cm^{-1}. [12] The sixth peak at 1021 cm^{-1} agrees well to both experiment (1040 cm^{-1}) and computation (1010 cm^{-1}) in literature. [10], [11] Thus our computed IR modes for the crystalline phases are in reasonable agreement to published literature.

Computed IR spectra of ZrSiBCN models (Figure 9) exhibit three major regions. A first below 200 cm^{-1}, a second (main peak) from 200 to 600 cm^{-1}, and the high frequency tail above 600 cm^{-1}. Inspection of eigenmodes shows that the range below 200 cm^{-1} is attributed to vibrations of Zr atoms without contribution from C, N, Si or B atoms. The range between 200-600 cm^{-1} is related to localized Zr-C, Zr-N, and Zr-B vibrations while above 600 cm^{-1} we observe modes with localized Si-N, B-N and B-B vibrations. Both hexagonal and cubic boron nitride shows characteristic peaks between 780 and 1300 cm^{-1}. [12-15]. The spectra shown in Fig. 9 show significant fluctuations and by visual inspection, no trend can be extracted. However, the increasing Si_3N_4-content correlates with an increase of vibrational modes with wave numbers larger than 600 cm^{-1} (see Fig. 10).

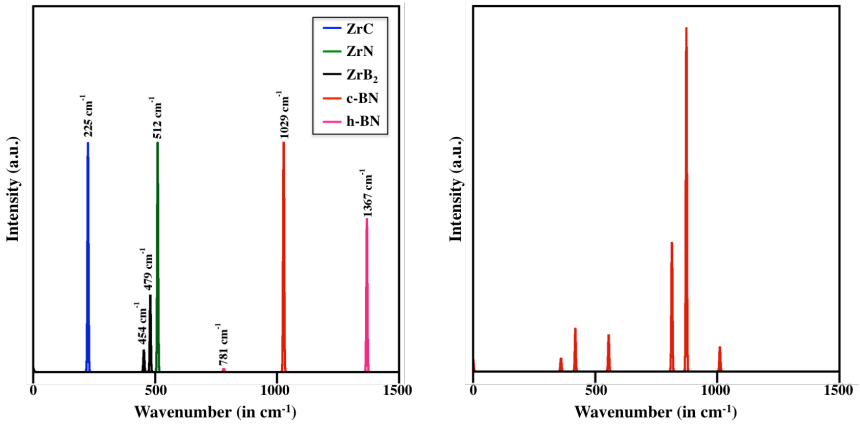

Figure A2.1: (Left) IR spectra for crystalline ZrB_2, ZrC, ZrN, c-BN and h-BN. (Right) IR spectra for β-Si_3N_4. In these spectra, each line has been broadened using Gaussian functions of 3 cm^{-1} width.

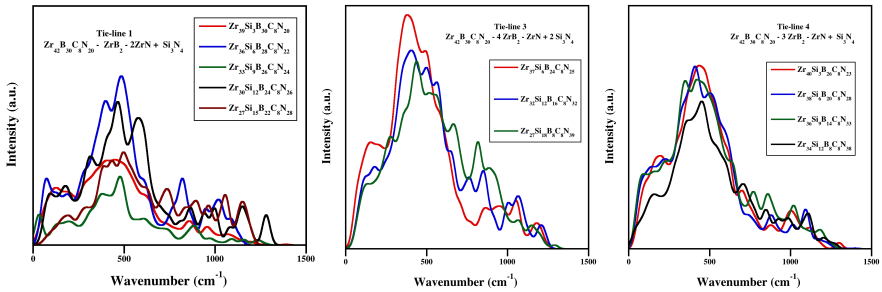

Figure A2.2: IR spectra of (left) five compositions along pathway (1), (middle) three compositions along pathway (3) and (right) 4 compositions along pathway (4). Each IR spectra is an average of 6 models; lines have been broadened using Gaussian functions of 50 cm^{-1} width.

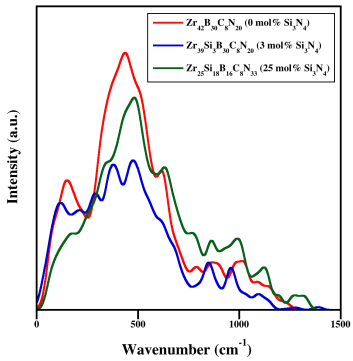

Figure A2.3: IR spectra of three models with different Si_3N_4 –content, 0, 3 and 25 mol%, to illustrate trends in relative intensities. Each IR spectra is an average of 6 models; lines have been broadened using Gaussian functions of 50 cm^{-1} width.

A3.3) Structure of the parent composition – $Zr_{42}B_{30}C_8N_{18}$

In this section, is a representative model of $Zr_{42}B_{30}C_8N_{18}$ – the parent composition. The model shows seggregation of B atoms, in the form of B_6 rings fused between the Zr layer. This models is also generated in the same strategy as in the a-ZrSiBCN model: melt and quench followed by repeated annealing.

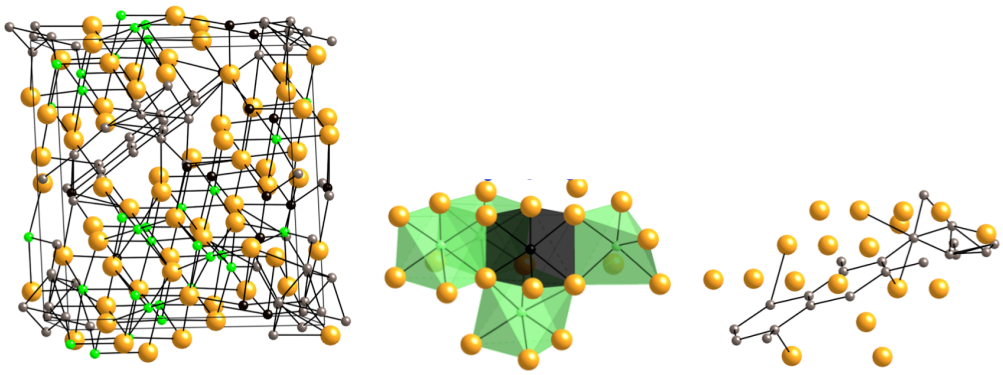

Figure A2.4: (Left) Representative model of amorphous $Zr_{42}B_{30}C_8N_{18}$ structure obtained after three cycles of repeated annealing. (Middle & right) ZrN(C) nucleus and fused B_6-rings between Zr layers. Note that on the nuclei in middle one C is substituting for N. This model has a hardness of 11 GPa and kmin of 4.1 $Wm^{-1}K^{-1}$Large (orange) spheres represent Zr, small (green) N, small (blue) Si, small (brown) B, and small (black) C. Models are courtesy of Dr. P. Kroll.

References

[1] D.R. Clarke, Surf Coat Tech, 163 (2003) 67-74.

[2] J.W. Lawson, M.S. Daw, C.W. Bauschlicher, J Appl Phys, 110 (2011).

[3] N. Hirosaki, Y. Okamoto, M. Ando, F. Munakata, Y. Akimune, J Ceram Soc Jpn, 104 (1996) 49-53.

[4] J. Houska, P. Steidl, J. Vlcek, J. Martan, Ceram Int, 42 (2016) 4361-4369.

[5] A.L. Ortiz, V. Zamora, F. Rodriguez-Rojas, Ceram Int, 38 (2012) 2857-2863.

[6] H.G. Smith, N. Wakabayashi, M. Mostoller, Phonon Anomalies in Transition Metals, Alloys and Compounds, in: D.H. Douglass (Ed.) Superconductivity in d- and f-Band Metals: Second Rochester Conference, Springer US, Boston, MA, 1976, pp. 223-249.

[7] P.T. Jochym, K. Parlinski, Eur Phys J B, 15 (2000) 265-268.

[8] L.H. Liu, C.J. Liu, S.Y. Yang, Z.J. Zhang, W. Gao, Z.M. Xie, Chinese J Polym Sci, 21 (2003) 99-101.

[9] S.D. Gupta, S.K. Gupta, P.K. Jha, Journal of Thermal Analysis and Calorimetry, 107 (2012) 49-53.

[10] N. Wada, S.A. Solin, J. Wong, S. Prochazka, Journal of Non-Crystalline Solids, 43 (1981) 7-15.

[11] Y.Q. Cai, L.T. Zhang, Q.F. Zeng, L.F. Cheng, Y.D. Xu, Physical Review B, 74 (2006).

[12] X.J. Wang, Y. Xie, Q.X. Guo, Chem Commun, (2003) 2688-2689.

[13] R. Geick, C.H. Perry, Rupprech.G, Physical Review, 146 (1966) 543-&.

[14] S.Y. Shapoval, V.T. Petrashov, O.A. Popov, A.O. Westner, M.D. Yoder, C.K.C. Lok, Appl Phys Lett, 57 (1990) 1885-1886.

[15] K. Inagawa, K. Watanabe, H. Ohsone, K. Saitoh, A. Itoh, J Vac Sci Technol A, 5 (1987) 2696-2700.

Summary:

Amorphous ZrSiBCN ceramics have an applications as a high performance coating material at elevated temperatures. This work is a significant contribution to the *Materials Genome Project*. The key points of this study are summarized as below:

1. Si_3N_4 is added to the parent composition of $Zr_{42}B_{30}C_8N_{18}$ along 4 proposed pathways. The amount of Si_3N_4 added varies between 3 – 19 mol %.
2. Nucleation is observed in these models (100 atoms), even within small time-scales of simulations.
3. The addition of Si_3N_4 to the parent material lowers the tendency of crystalline aggregate formation – nuclei of ZrN(C) or fused *honey-comb* like B_6 rings in between Zr layers.
4. Computed mechanical properties of the parent material are also compromised as Si_3N_4 is added to it. Decrease in bulk, shear and Young's modulus are observed which also leads to a decrease in the Vicker's Hardness (H_V). While absolute values computed cannot be compared to experimental data available (due to differences in methodology), this study still proposes a clear trend.
5. The parent composition has a H_V of (8 ± 4) GPa. Adding small amounts of Si_3N_4 (3 mol %, $Zr_{39}Si_3B_{30}C_8N_{20}$) does not affect the hardness (8 ± 1 GPa). If this composition is experimentally synthesized it will be a useful addition to oxidation resistant coatings. The low quantity of Si_3N_4 is expected to prevent the oxidation of ZrBCN composition by forming protective layer of borosilicate glass.

Open threads in ZrSiBCN modeling comprise of building large-scale models of ZrSiBCN compositions that enable us to further study the effects of crystalline aggregates on material properties. Two important questions arise: 1) Is there a Hall-Petch effect that could connect the size of the crystalline nuclei to the strength in these materials ? [1-5]

2) What is the critical size of these nuclei if they were not restricted within periodicity of the small models? [6]

References:

[1] J.H. Vanderveen, E.O. Hall, W.P. Rees, N.J. Petch, A.J.K. Honeyman, N.P. Allen, J.E. Mclennan, A.M. Sage, A.A. Wells, P.L. Pratt, G.M. Boyd, T.S. Robertson, G. Burns, B.C. Woodfine, G.W. Greenwood, A.G. Quarrell, C.F. Tipper, B.E. Hopkins, The Notched Slow-Bend Test as a Brittle-Fracture Test - the Fracture of Alpha Iron - Intergranular Brittleness in Iron-Oxygen Alloys - the Cleavage Strength of Polycrystals - Discussion, J Iron Steel I 177(3) (1954) 334-345.

[2] W. Sylwestrowicz, E.O. Hall, The Deformation and Ageing of Mild Steel, P Phys. Soc. Lond. B 64(378) (1951) 495-502.

[3] N.J. Petch, The Cleavage Strength of Polycrystals, J Iron Steel I 174(1) (1953) 25-28.

[4] E.O. Hall, The Deformation and Ageing of Mild Steel .2. Characteristics of the Luders Deformation, P Phys. Soc. Lond. B 64(381) (1951) 742-&.

[5] E.O. Hall, The Deformation and Ageing of Mild Steel .3. Discussion of Results, P Phys. Soc. Lond. B 64(381) (1951) 747-753.

[6] J.J. De Yoreo, P.G. Vekilov, Principles of Crystal Nucleation and Growth, Rev. Mineral. Geochem. 54(1) (2003) 57.

CHAPTER 3

MODELING AMORPHOUS SILICON NITRIDE: A COMPARATIVE STUDY OF EMPIRICAL POTENTIALS[3]

[3] This work is accepted in Computational Materials Science and is being used with the permission of the publisher, 2017

Scope and Motivation

Amorphous silicon nitride (a-Si_3N_4) ceramics is the leading contender for engine parts – turbo charger rotors, valve springs, etc.. Si_3N_4 also has applications in microelectronics and is used to mask oxidation in silicon integrated circuits. Moreover, Si_3N_4 is resistant to water and alkali salts and is used as protective coatings for silvered glass mirrors. Si_3N_4 is biocompatible and used in bearings that improve endurance of prosthetic hip and knee joints. The study of Si_3N_4 microstructure is important. [1-3]

Various models of a-Si_3N_4 have been proposed, the first being a "ball-and-stick model" by Ohdomari et al. using the ideas of a continuous random network (CRN). More recently, the use of empirical potentials is a popular method to model a-Si_3N_4. Several empirical potentials were implemented to describe amorphous Si_3N_4 however, a comparative study between these empirical potentials is lacking. In this chapter, I include results of a study that involves modeling a-Si_3N_4 using 9 different flavors of empirical potential. These models are optimized using DFT and investigated for their thermochemistry and local coordination defects.

Interestingly, I conclude that the Tersoff potential, one of the most cited empirical potentials when modeling a-Si_3N_4, produces unrealistic models with numerous *dangling bonds*. This work also brings the Marian-Gastreich two body potential (MG2) and the Garofalini potential (SG) to the forefront as my results indicate these are the best potentials to model a-Si_3N_4. A major reason for the neglect in usage of the MG2 potential is inaccessibility. The MG2 potential is not available in any popular molecular dynamics simulation package. However, as a part of this project, I have implemented the MG2 potential in LAMMPS, and will make it available to the community upon request.

This chapter first includes the journal article followed by the appendix where I include details of implementation of MG2 potential in LAMMPS and some more useful supplementary information.

References

[1] A.J. Moulson, Reaction-bonded silicon nitride: its formation and properties, J. Mater. Sci. 14(5) (1979) 1017-1051.

[2] R. Riedel, G. Mera, R. Hauser, A. Klonczynski, Silicon-based polymer-derived ceramics: synthesis properties and applications-a review dedicated to Prof. Dr. Fritz Aldinger on the occasion of his 65th birthday, J. Ceram. Soc. Jap. 114(1330) (2006) 425-444.

[3] B.S. Bal, M.N. Rahaman, Orthopedic applications of silicon nitride ceramics, Acta Biomater. 8(8) (2012) 2889-2898.

Modeling amorphous Silicon Nitride: A comparative study of empirical potentials

Atreyi Dasmahapatra[1] and Peter Kroll[1*]

[1] Department of Chemistry and Biochemistry, The University of Texas at Arlington, 700 Planetarium Place, Arlington, Texas 76019, United States.

Abstract:

We perform a comparative study of empirical potentials for atomistic simulations of amorphous silicon nitride (a-Si_3N_4). We choose 5 different parameterizations of the Tersoff potential, the Marian-Gastreich two-body (MG2) and three-body (MG3) potential, the Vashishta (V) potential, and the Garofalini (SG) potential. Amorphous models of Si_3N_4, comprising of 448 atoms, are generated by each empirical potential using a melt-and-quench procedure. Subsequently, models are optimized using Density Functional Theory calculations, and structures resulting from these DFT optimizations are compared. We emphasize local coordination of atoms and the enthalpies of formation (ΔH_f) relative to crystalline β-Si_3N_4. The SG and MG2 potentials prove to be best options for modeling of a-Si_3N_4. Models generated with these potentials are close to their DFT local minimum, exhibit the smallest number of defects, and have realistic enthalpies of formation.

Introduction

Silicon nitride is a ceramic material with diverse applications owing to its good mechanical and electrical properties. [1] Dense sintered Si_3N_4 components exhibit high thermal strength and fracture toughness and are used in many engineering applications. [2,3] Thin films of amorphous silicon nitride have a high dielectric constant and are applied in microelectronics. [4-7] Thick films of Si_3N_4 are promising materials for non-linear optical applications. [8,9] Moreover, Si_3N_4 is an environmental barrier coating material due to its oxidation resistance up to 1500 °C. [10] Silicon nitride also exhibits great biocompatibility and is used as bearings for total hip and knee joint replacement in orthopedics. [11]

There is extensive work in computational modeling of amorphous silicon nitride (a-Si_3N_4). The first study was reported by Ohdomari et. al. who constructed a continuous random network ball-and-stick model. [12] A Keating type potential was applied to relax these models and radial distribution functions characterized the local environment of atoms. Umesaki et al. used a Busing-type pair potential to model a-Si_3N_4 by molecular dynamic (MD) simulations. [13] Their models consisted of SiN_4 tetrahedral units with few structural defects, and the radial distribution function (RDF) as well as the structure factor agreed well with experimental data.

Development of a Tersoff potential to model a-Si_3N_4 was first pursued by Kroll. [14] Seven different parameterizations for the N atom were proposed and used together with the original Si parameters by Tersoff. [15,16]. Adopting one of these parameter sets, Matsunaga studied a variety of silicon nitride ceramics including amorphous SiCN, SiBN and Si_3N_4 ceramics. [17,18] Brito-Mota et al. proposed an alternative parameter set for N and studied local geometry and bonding in a-SiN_x ($0 < x < 1.6$) materials. [19,20] The parameterization of Brito-Mota was later augmented to study hydrogen interactions in a-SiN_x:H systems. [21] Vashishta et. al. developed a Si-N interaction potential including charges, polarizabilities, and bond angle terms. This potential was used to model multi-million atom models of a-Si_3N_4 and study nano-indentation, crack propagation, and various mechanical properties of a-Si_3N_4. [22-26] As part of their efforts

to model SiBN ceramics, Marian et. al. proposed a two-body potential for interactions involving Si, B and N. [27] This potential reproduced structure, vibrational and elastic properties of crystalline Si_3N_4 and BN, and was used to model mixtures of these two systems, particularly $Si_3B_3N_7$. The same authors also suggested a more elaborate three-body potential for modeling SiBN materials. [28] Completing this brief survey, Garofalini et. al. developed an interaction potential for modeling inter-granular films in Si_3N_4 ceramics. [29,30]

Given several empirical potentials available for modeling Si_3N_4, an obvious question is: which is the best? Since all the potential models outlined have been fitted to properties of α- and β-Si_3N_4, they describe these crystalline structures quite well. However, these potentials are also used to model amorphous silicon nitride, and while transferability is commonly assumed, it is, by no means, guaranteed to work. Therefore, our goal is to compare these different empirical potentials with respect to their ability to provide sound models of amorphous silicon nitride. Our comparison is facilitated through Density Functional Theory (DFT) calculations, which provide a rigorous assessment of every structure generated by each empirical potential within one common method.

The next section will provide a brief description of the individual empirical potentials. We then describe the computational approach that we use for structure generation and DFT calculations. In the result section we emphasize local atomic arrangements and structural changes happening during DFT optimizations as well as the enthalpy of formation.

Interatomic Potentials

In this section we briefly describe the analytical form of each empirical potential and their parameters.

1. Tersoff Potential

The Tersoff potential is based on the concept that the strength of a bond between two atoms depends on their local environment. [15,16] The potential is short-ranged, with only the first

coordination shell included, and consists of two-body and three-body terms. It was originally developed to model single element semi-conductors such as Si, Ge, and C, but soon was applied to binary systems such as SiC. [31] The key-idea of the Tersoff potential is its "transferability"; eleven (11) parameters are developed for each element, only once. Parameters for interaction in compound systems are then governed by simple rules of mixture. This approach, ideally, eliminates the work to find new parameter sets for every new combination of elements. Practically, the potential still uses two unique parameters for each binary combination of elements, χ_{ij} and ω_{ij}, which can be used to tailor hetero-atomic interaction. The explicit functional form of the potential is given in the appendix.

Tersoff-parameters for modeling of Si_3N_4 have been developed by Kroll and by Brito-Mota et al. [14,20]. Kroll followed the original idea of Tersoff and fitted potential parameters for N using structure and elastic data for hypothetical phases of nitrogen only. Unique parameters for C-N and Si-N interaction were subsequently fitted using experimental and computed data of C_3N_4 and Si_3N_4 crystalline structures. A variety of parameter sets were proposed and analyzed. [14] Three suitable sets are shown in Table 1 (labels 001-1, 001-2, 002-1). Brito-Mota et al., on the other hand, optimized their parameter set for N-N and for Si-N interaction simultaneously using experimental and computed data available for β-Si_3N_4, the N_2 molecule and trisilylamine molecule, Si_3NH_9. The parameters (label BM) are included in Table 1. The parameter set used by Matsunaga et al. is identical with set 001-1 of Kroll; with the exception that one of the unique binary parameters (ω_{ij}) was set to 1. [18] It is listed as an independent set (label mat) in Table 1. For all Tersoff potential parameterizations, the attractive part of homo-atomic interactions Si-Si and N-N is set to zero for modeling of Si_3N_4. Hence, Si-Si and N-N interactions are repulsive up to the defined cutoff distance.

Parameters	001-1	001-2	002-1	mat	BM

A [eV]	11000	11000	8860.0	11000	6368.14
B [eV]	219.45	219.45	197.09	219.45	511.760
λ [$Å^{-1}$]	5.7708	5.7708	5.5237	5.7708	5.43673
μ [$Å^{-1}$]	2.5115	2.5115	2.3704	2.5115	2.70
b [10^{-2}]	10.562	10.562	5.8175	10.562	0.529380
n	12.4498	12.4498	8.2773	12.4498	1.33041
c	79934	79934	79126	79934	20312.0
d	134.32	134.32	112	134.32	25.5103
cos q (h)	-0.99734	-0.99734	-0.99995	-0.99734	-0.562390
$\chi_{Si\text{-}N}$	0.91736	0.88779	0.85758	0.91736	0.65
$\omega_{Si\text{-}N}$	1.0993	0.98426	0.66175	1*	1.00
R (pm)	180				
S (pm)	210				

Table 1: Tersoff potential parameter sets for N: 001-1, 001-2, 002-1 by Kroll, BM by Brito-Mota et al. and mat by Matsunaga. [14,17,20] The sets 001-1 and 001-2 differ only in choice of the unique binary parameters $\chi_{Si\text{-}N}$ and $\omega_{Si\text{-}N}$. The parameter set mat is identical to 001-1 except for $\omega_{Si\text{-}N}$ (set to 1 in mat).

2. Marian-Gastreich two-body potential (MG2) [27]

The MG2 potential was originally developed for modeling of SiBN ceramics. [27] For our study, we use its portion relating to SiN systems only. The potential consists of two-body terms only: attractive Morse-type for Si-N, screened Coulomb repulsion for Si-Si and N-N, and an additional dispersion term for N-N interactions. A taper function provides a cutoff at a distance of 5.8 Å. The explicit form of the potential together with parameters is given in the appendix. The absence of a three-body term in covalently bonded systems makes the MG2 potential unique in comparison to all other empirical potentials considered in this study.

3) The Marian-Gastreich three-body Potential (MG3) [28]

Soon after the MG2 potential, the same authors developed a three-body potential for modeling of SiBN ceramics. [28] The MG3 potential includes charges, attractive Coulomb interactions and a Stillinger-Weber-type angular term. [32] A smooth cutoff of the potential limits its range to 8 Å. Si-Si and N-N interactions are repulsive up to the cutoff. We use only the portion relating to SiN systems in this work. The analytical form of the potential together with parameters is given in the appendix.

4) The Vashishta Potential (V) [22]

The Vashishta potential is another approach involving two-body and three-body terms. It includes steric repulsion, screened Coulomb interaction, and screened charge-dipole interactions. A three-body Stillinger-Weber-type angular term accounts for bond bending effects. [32] The two-body part of the potential has a cutoff distance of 5.5 Å, while the three-body part is short-ranged with a cutoff of 2.6 Å. Homo-atomic interactions of Si-Si and N-N are defined repulsive. The analytical form of the potential along with its parameters is included in the appendix.

4) The Garofalini Potential (SG) [29]

The Garofalini potential, originally developed to study inter-granular films in Si_3N_4 ceramics, consists of both two and three body terms. The two-body term is a modified Born-Meyer Huggins potential that defines the homo-atomic interactions as repulsive. [33-35] The three-body

part adopts the functional form of the Stillinger-Weber potential. [32] The analytical form and the parameters for this potential are given in the appendix.

Computational Method:

The empirical potentials have been implemented into the LAMMPS-code (Large-scale Atomic/Molecular Massively Parallel Simulator), with the exception of the MG3 potential, for which we rely exclusively on the GULP (General Utility Lattice Program) package. [36,37] Generating models of amorphous Si_3N_4 is achieved through molecular-dynamic (MD) simulations following a standard melt-and-quench (MQ) procedure: first producing a "melt-like" state at very high temperatures and thereafter cooling the system down to low temperature and minimizing its energy. All MD and energy minimizations using empirical potentials are carried out at constant volume. Each model comprises 448 atoms (192 Si, 256 N), which is a compromise between size (simulation box parameter ~16 Å) and computational demand, since all models are further computed using Density Functional Theory (DFT) calculations.

In LAMMPS, we heat the system from 0 to 5000 K in 3 ps (rate = 1.5 x 10^{15} K•s^{-1}). At 5000 K a "melt" has formed, confirmed by rapid exchange of neighbors for all atoms. We keep the system at 5000 K for 0.75 ps, and then "quench" the system to 3000 K in 75 ps (2.6 x 10^{13} Ks^{-1}), at which temperature we keep it for 0.75 ps. Next we cool the system to 2000 K in 75 ps (1.3 x 10^{13} Ks^{-1}) and from there, finally, to 300 K in another 75 ps (2.3 x 10^{13} Ks^{-1}). The total simulation time for this melt-quench procedure is 229.5 ps. We use a time step of 0.15 fs throughout these MD simulations. After the MD-MQ procedure, we perform a final energy minimization of the structure. In GULP, we use a slightly different temperature profile due to scaling issues of the code. MG3 models have been produced by first heating the system from 0 to 5000 K in 10 ps (rate = 4.7 x 10^{14} K•s^{-1}) after which we cool it to 300 K in 105 ps (4.5 x 10^{13} K•s^{-1}). Thus, models generated in GULP have been quenched at more than twice the rate in comparison to models generated with LAMMPS. Since this could be a potential source of concern, we analyzed results for models generated with the MG2, for which we used both codes and temperature schedules.

However, we compared energies and radial distribution functions and found no discernable differences between the two cohorts of models generated either way.

Since we work at constant volume, we set the volume of the simulation box to match densities from 2.6 - 3.4 $g \cdot cm^{-3}$ (in steps of 0.1 $g \cdot cm^{-3}$). For every density we produce 10 models, hence a total of 90 models for each potential.

We compared the CPU usage for the individual potentials for a system of 3584 atoms for 35000 MD steps. While the total time spent will depend on the particular platform, a comparison of relative computational effort needed may be a decisive factor when choosing a particular potential. With the exception of the MG3 potential, we achieved all computations within LAMMPS on the Stampede supercomputer at Texas Advanced Computing Center (TACC). As expected, the two-body MG2 potential turned out to be the fastest method, with 3.9 μs/atom/step. Tersoff potentials needed approximately 5, the Vashishta potential 7.1, and the SG potential 10 μs/atom/step.

After structure generation by the melt-quench method, we switch to Density Functional Theory (DFT) calculations employing the VASP code (Vienna Ab-Initio Simulation Package). [38-40] We use the Generalized Gradient Approximation (GGA) for electron exchange and correlation combined with the Projector Augmented Wave (PAW) method. [41] The Brillouin zone is sampled at the Γ−point. At the start of DFT calculations, we compute the energy of all (approximately 1,000) models using soft pseudopotential and cut-off energy (E_{cut}) of 300 eV for the expansion of the wave function into a plane wave basis set. These "static" calculations yield DFT energies, which we use to select models for further optimization. Of the 90 models computed for every empirical potential, we select the 10 models with lowest energy and proceed to further optimizations within DFT. We always add models with low density to the cohort to study their development in the quantum-chemical approach.

Optimization within DFT is first done at constant volume continuing with soft pseudopotential and E_{cut} = 300 eV. After 60 optimization steps, we switch to hard pseudopotentials, E_{cut} of 500 eV, and optimize lattice parameters and positions simultaneously. In the end, forces are

converged to lower than 0.1 eV/Å and stresses smaller than 5 kBar. We compute the reference energy of crystalline β-Si_3N_4 to 8.170 eV/atom and 8.182 eV/atom, within the two approaches, respectively.

Site-site pair-correlation functions (PCFs) of a-Si_3N_4 are generated collecting individual entries of the ten (10) models with lowest energy selected for "full" DFT optimization. We broaden the data with Gaussians of FWHM = 2 pm. Each PCF is drawn to scale and is normalized so that it approaches the value 10 at infinite distance. The difference between two ticks on the ordinate is 30.

Results and Discussion:

Structure

Representative models of a-Si_3N_4, consisting of 448 atoms with a density comparable to that of crystalline β-Si_3N_4 (3.1 g·cm^{-3}) are shown in Figure 1. These models have been generated by the empirical MG2 and Vashishta potentials and subsequently optimized in DFT.

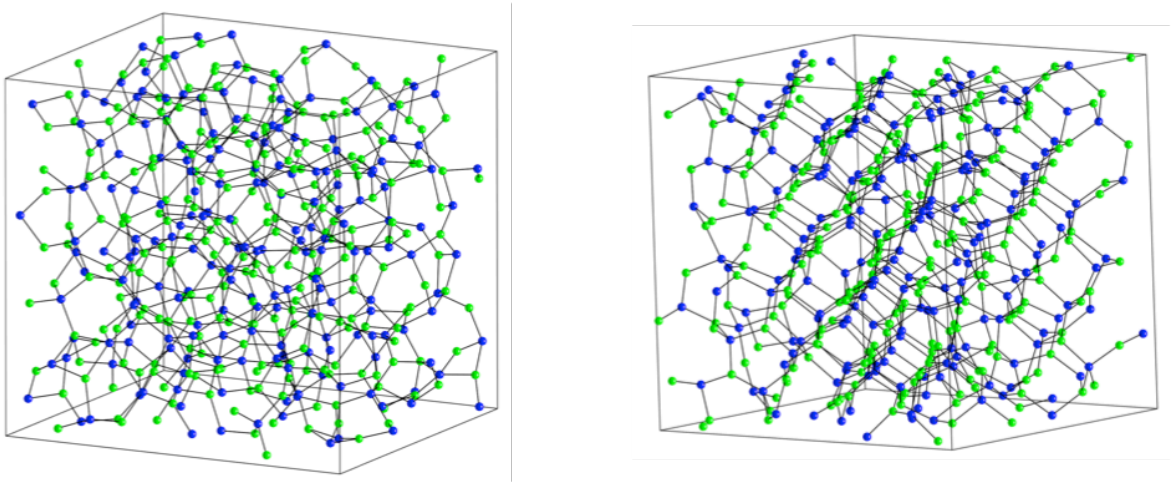

Figure 1: Representative models of a-Si_3N_4 generated with the MG2 (left) and Vashishta (right) potential and subsequently optimized in DFT. Blue spheres are Si. Green spheres are N. Density of each model is 3.1 g•cm^{-3}. The simulation boxes have dimensions between 16 and 17 Å and angles 88°< α, β, γ < 92°.

Characterizing the structure of amorphous a-Si_3N_4 models, we first turn to the coordination of individual atoms. The crystal structures of α- and β-Si_3N_4 display Si 4-fold coordinated by N and N 3-fold coordinated by Si. Bonding in amorphous silicon nitride (which may still contain small proportions of hydrogen) resembles the local environments of β-Si_3N_4, with only minute amounts of defects. [42,43] In contrast, the high-pressure modification of γ-Si_3N_4, which adopts a spinel-type structure, exhibits both 4-fold and 6-fold coordinated Si together with 4-fold coordinated N. The 3-fold coordinated Si (silyl-cation) is a known species in chemistry, but it is highly reactive and can only stabilized by very bulky ligands under particular conditions. [44]

The models produced using different flavors of empirical potentials exhibit significant amounts of "under-coordinated"(UC) Si (3 or fewer neighbors) and N (2 or fewer neighbors) as well as "over-coordinated"(OC) Si (5 or more) and N (4 or more). Though it is often difficult to make a clear distinction between a "very long" Si-N bond, which may occur for a strongly pyramidal Si displaying a fourth Si-N distance of up to 2.40 Å, and a "true" 3-fold connected $Si^{[3]}$, we set the first nearest neighbor cut-off distance to 2.20 Å for convenience. This is about 30% larger than the Si-N bond length of 1.72 Å in β-Si_3N_4. [42,43] The fractions of "under-" and "over-coordinated" atoms in lowest energy models – as achieved from empirical potential simulation prior to DFT and after DFT calculations – are given in Table 2 together with the average coordination number, CN, before and after DFT.

Overall, models generated with the Tersoff potential – parameter sets 001-1, 001-2, 002-1, mat and BM – exhibit 10 - 20% under-coordinated Si after model generation and before DFT optimization. The amount reduces significantly during DFT optimization, due to the high reactivity of $Si^{[3]}$. However, the fraction of $Si^{[3]}$ present after DFT optimization still exceeds 4% in all Tersoff-models. The percentage of over-coordinated Si is up to 10%, and changes only marginally during DFT optimization. Considering the coordination environment of N atoms, we find that all Tersoff models exhibit 3 - 10% under-coordinated N before DFT optimization, changing slightly to 3 - 7 % after DFT optimization. The percentage of over-coordinated N is about 6 - 8% for all Tersoff parameters sets. Overall, the Tersoff potentials provide the highest

fraction of Si and N atoms deviating from their "ideal" coordination number of 4 and 3, respectively.

In contrast to Tersoff potentials, the MG2, MG3, Vashishta and SG empirical potentials generate significantly less under- and over-coordinated atoms. In particular, these potentials provide smaller fractions of under-coordinated Si in comparison to Tersoff models. This impacts structural changes during subsequent DFT optimizations. Among the peculiarities we observe is the inclination of the MG3 potential to generate models with many over-coordinates atoms. Even after DFT optimization, these models retain an average Si coordination number of 4.1. In contrast, the Vashishta and SG potentials strongly avoid over-coordination of Si.

Taking a look at models with low-density ($\rho < 2.7$ g·cm^{-3}), we find that, with the exception of the MG2 potential, all empirical potentials produce significantly higher fractions of under-coordinated atoms. Tersoff models exhibit 20-30 % under-coordinated Si and 10-20 % under-coordinated N before DFT optimizations. This number drops by half, 10-15 % for Si and 5-10 % for N, after "full" DFT optimization. The Vashishta and SG potential models also produce higher amounts of under-coordinated Si (15 % for both V and SG) and N (10 % for V and 12 % for SG) at low density. These values reduce to less than 5 % for both Si and N after DFT optimization. The MG3 potential yields 16% of under-coordinated Si and 12% of under-coordinated N before DFT, which is reduced to 10% for Si and 8% for N after DFT optimizations. Only for the MG2 potential the fraction of under-coordinated Si and N is below 10 %. After DFT optimization, the fraction of under-coordinated Si and N, change only minimally.

As noted earlier, all potential approaches applied here implement repulsive N-N and Si-Si interactions and, therefore, explicitly prevent formation of close N···N or Si···Si contacts during structure simulation. The Tersoff approach, in principle, can include N-N bond formation and a detailed assessment and discussion is given in Ref. [14]. Despite forced avoidance, Tersoff-models always contain 2-4 N-N bonds after DFT optimization. (see Table 2) Hence, with 256 N atoms in each model, 2-3 % of N atoms are involved in homo-atomic N-N bonds. In contrast, no such bonds appear in models generated by the MG2, MG3, V, or SG potentials after DFT

optimization. These potentials are apparently more effective in avoiding N-N bonds due to their longer cutoff distance.

		Before DFT			After DFT			
Pot Name	Atom center	% UC	% OC	CN	% UC	% OC	CN	Number of N-N bonds
001-1	Si	17	4	3.9	5	8	4.0	3.6
	N	10	0	2.9	6	9	3.0	
001-2	Si	16	6	3.9	5	8	4.0	2.8
	N	7	0	2.9	4	6	3.0	
002-1	Si	16	15	4.0	9	8	4.0	3.2
	N	1	2	3.0	7	7	3.0	
mat	Si	15	6	3.9	7	9	4.0	2.4
	N	7	0	2.9	5	6	3.0	
BM	Si	13	9	4.0	4	9	4.0	2.2

	N	3	0	3.0	3	7	3.0	
MG2	Si	2	6	4.0	2	5	4.0	0.0
	N	6	8	3.0	1	5	3.0	
MG3	Si	4	12	4.1	3	9	4.1	0.0
	N	0	7	3.1	1	5	3.0	
V	Si	2	0	4.0	1	1	4.0	0.0
	N	7	4	3.0	4	4	3.0	
SG	Si	6	0	3.9	1	4	4.0	0.0
	N	5	1	3.0	2	4	3.0	

Table 2: Statistics for Under-coordinated (UC) and Over-coordinated (OC) atoms as well as average coordination numbers for Si and N in a-Si_3N_4 models. "Before DFT" refers to models obtained after empirical potential simulations, while "After DFT" refers to models optimized completely in DFT. The average number of N-N bonds, found only in Tersoff models after DFT optimization, is listed as well.

Despite all imperfections in local bonding, the average Coordination Number (CN) is between 3.9 and 4.1 for Si and 2.9 and 3.1 for N — in all models, unrelated to density and independent of the particular potential applied. Hence, all potentials generate – on average – an "ideal"

coordination number of 4 and 3 for Si and N, respectively. This trend is, of course, reminiscent of the parameter fitting, and has been stated for these potentials before. [18-20,27-29]

In course of our modeling we encountered a peculiarity of the Vashishta potential (V). It generates highly ordered structures including macro- and nano-crystalline models. Figure 1, right side, already shows ordering of Si and N atoms in planes together with 6-membered rings that are typical for sphalerite and wurtzite structures. In Figure 2 we emphasize a polyhedral representation of that model: tetrahedral center of Si are connected by N, which indeed arrange in closest packed planes stacked on top of each other. Essentially, Si atoms fill tetrahedral interstitials, and small nuclei of a (hypothetical) defective sphalerite Si_3N_4 emerge. In small models with 448 atoms and 16 – 17 Å box length the driving force towards such structures is so strong that some simulations result in a single-crystal. Large-scale models still show this trend by forming nano-crystalline structures, see Fig. 2 right.

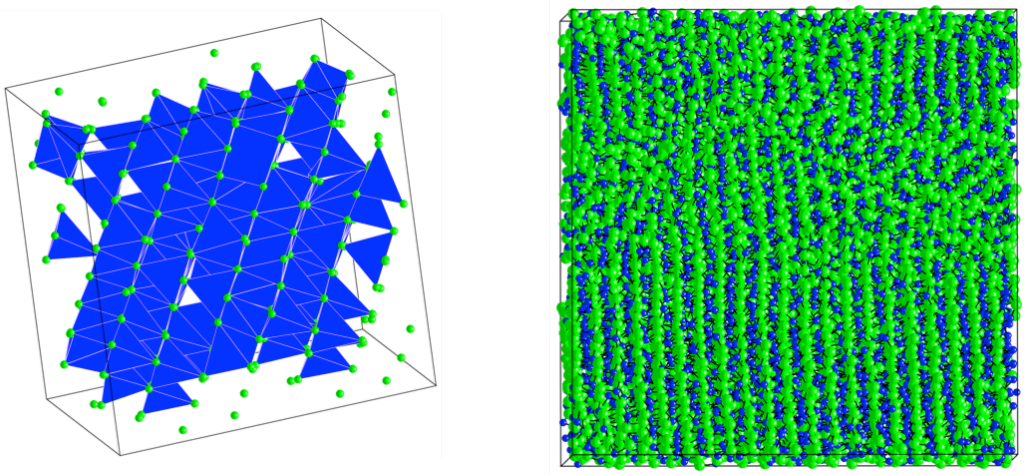

Figure 2: Model of Si_3N_4 generated using Vashishta potential. (Left) Small model of 448 atoms shows a regular arrangement of N atoms (represented by spheres). (Right) Large-scale model comprising of 12,096 atoms also shows N atoms ordered along lattice planes. The box length is 48.3 Å. Green spheres are N, while blue spheres are Si atoms.

Pair Correlation Function

In Figure 3 we show site-site distance pair correlation functions (PCF) or total g(r) of a-Si_3N_4 models generated by each empirical potential and computed before and after DFT optimizations.

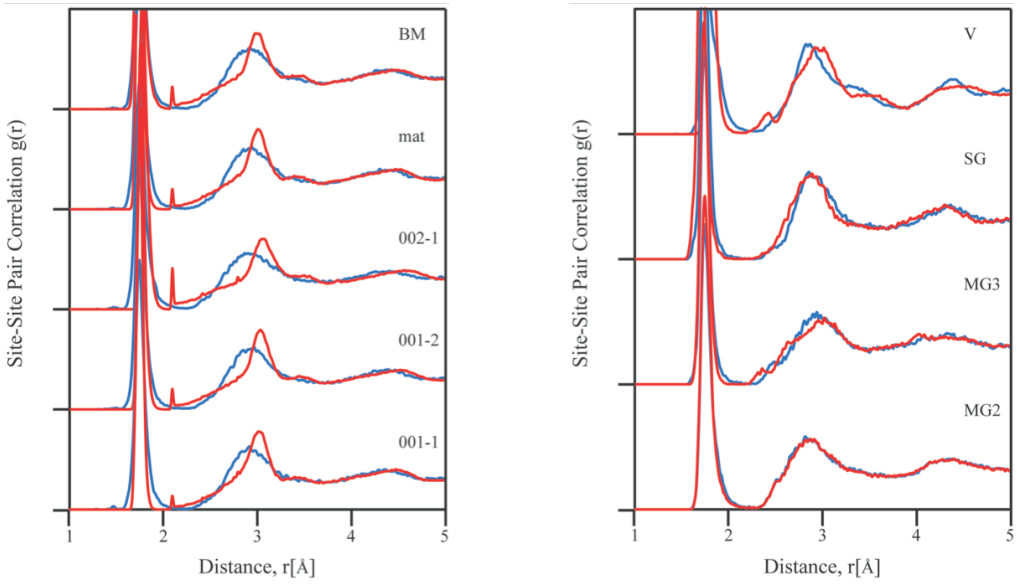

Figure 3: Site-site distance pair correlation function (PCF) or total g(r) of a-Si_3N_4. Red lines refer to models before and blue lines to models after DFT optimization. (Left): PCFs for 5 different parameterizations of the Tersoff potential (right): PCFs for MG2, MG3, SG and Vashishta (V) potential models of a-Si_3N_4.

Pair correlation functions of the various Tersoff potentials (Fig. 3, left) resemble each other closely. Si-N bonds are found in the first major peak around 1.7 Å, with only small variations. Common to all structures generated by Tersoff potentials is a small peak at 2.1 Å. This distance reflects the cut-off for N-N repulsion in the Tersoff potential (parameters R and S; see Appendix). Thus, for every N any "neighboring" N is pushed outside this cut-off radius, and N···N contacts with distances smaller 2.1 Å are penalized. Similarly, Si···Si contacts are "allowed" only beyond 2.8 Å, and this distance is marked by a small kink. Consequently, the pronounced peak at 3.0 Å is due to Si···Si correlations.

DFT optimization of Tersoff models smoothens out the peak at 1.7 Å and the kink at 2.8 Å. As noted before, some N-N bonds develop and become visible at 1.4 Å. Interestingly, the range from 2.1 to 2.4 Å is depleted after DFT optimizations. The pronounced Si···Si peak at 3.0 Å is

broadened and shifted to slightly shorter distances, where it now overlaps with the N···N next-nearest neighbor shell forming a wide hump centered at 2.9 Å.

While PCFs generated from Tersoff models before and after DFT optimization show noticeable differences, PCFs of SG, MG3, and – in particular – MG2 models remain remarkably consistent and almost unaffected by DFT optimizations. Si-N bonds appear at 1.7 Å, and N···N as well as Si···Si next-nearest neighbor correlations form the broad hump at 2.9 Å. Using the SG potential, Vedula et. al. reported very similar PCF peaks. [45] Amorphous Si_3N_4 models generated via MD simulations using the Car-Parrinello method and optimized in DFT (using LDA pseudopotentials) exhibit comparable PCFs. [46] Similarly, network models optimized using DFT calculations also corroborate the PCF peaks. [47]

Significant changes are also observed in PCFs of Vashishta models. Before DFT optimization the Si-N bond peak is centered at 1.8 Å. Persistent in all models is a small hump at 2.3 Å. It relates to Si···N contacts and involves all $Si^{[3]}$ and many $Si^{[4]}$. While the first peak "optimizes" to a typical Si-N bond distance of 1.7 Å upon DFT optimization, the hump develops into a "shoulder" at 2.0 Å. It is now due to "long" Si-N bonds for 4 and 5-coordinated Si atoms. The second coordination sphere of Si…N contacts appears at 3.4 Å and shifts slightly to 3.3 Å after DFT optimizations. While the PCF shown here is a collection of 10 independent models, strong ordering and formation of small nuclei is visible by a localized hump at 4.4 Å, which develops after DFT optimizations.

To highlight the pronounced order in some Vashishta models, we show in Fig. 4 the PCF (without DFT optimization) of one specific model up to 8 Å. For comparison, we add the PCF of a crystalline Si_3N_4 model with defective sphalerite structure (dsph-Si_3N_4). We also add the PCF of a model with dsph-Si_3N_4 structure subjected to MD simulations using the Vashishta potential for 10000 MD steps at 300 K. The similarities of the PCFs between the "amorphous" model and the MD-simulation of dsph-Si_3N_4 are striking. On the right side of Fig. 4 we show the PCF of the large-scale (12096 atoms) model shown previously in Fig. 2. Strong order is visible for up to 5 Å indicating the formation of nuclei with dsph-Si_3N_4 structure.

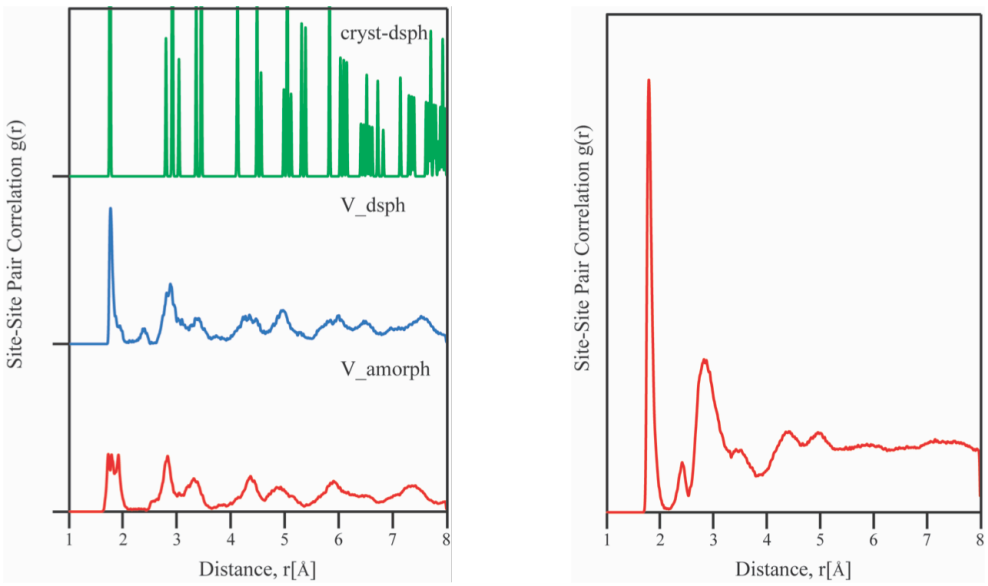

Figure 4: (Left) Total PCFs of a-Si_3N_4 structures. At the bottom the g(r) of one specific 448-atom model of "amorphous"-Si_3N_4 generated with the Vashishta (V) potential (Label: V_amorph); in the middle the PCF of crystalline dsph-Si_3N_4 obtained after MD simulations for 10000 steps at 300 K (snapshot) (Label: V_dsph); at the top the PCF of a 448 atom mode of crystalline dsph-Si_3N_4 (Space group P-43m; a=16.508 Å) (Label: cryst-dsph). (Right) Total PCF of a large-scale (12096 atoms) Vashishta potential model of a-Si_3N_4; the model is also shown in Fig. 2.

Enthalpy of formation

In Table 3, we list the energies of crystalline Si_3N_4 structures, α, β, γ, and dsph, with respect to the energy of β–Si_3N_4, computed by each potential.

Potential	β-Si_3N_4	α-Si_3N_4	γ-Si_3N_4	dsph-Si_3N_4
001-1	-5.57	0.03	0.84	0.47
001-2	-5.48	0.02	0.75	0.44
002-1	-5.76	0.01	0.29	0.28
BM	-5.24	0.01	0.58	0.19

mat	-5.85	0.03	0.86	0.43
MG2	-5.02	0.01	-0.08	0.06
MG3	-6.94	0.03	-0.01	0.19
V	-3.68	0.01	0.91	0.07
SG	-68.50	0.01	1.02	0.78
DFT	-8.182	0.001	0.15	0.25

Table 3: Energies (in eV/atom) of crystalline polymorphs of Si_3N_4. Energies are given relative to β-Si_3N_4, for which we state the value computed with the respective potential.

All potentials correctly predict that the β-phase is lower in energy than the α-phase in Si_3N_4. MG2 and MG3 yield the high-pressure γ-phase as the lowest energy configuration, a deficiency that has been noted before. [27,28] The stability of the high-pressure phase γ-phase correlates to the observed trend of over-cordination of atoms in MG2/MG3 models of a-Si_3N_4.

The data of Table 3 helps to analyze the enthalpy of formation, ΔH_f, of amorphous Si_3N_4 models that we show in Fig. 5. ΔH_f is a measure of energy compounded in local distortions, structural defects, and other deviation from a perfect crystal structure. This energy will (ideally) be released upon crystallization. The enthalpy of formation, ΔH_f, here defined *per atom* is given with respect to crystalline β-Si_3N_4 as the reference phase. The only experimental data of ΔH_f of Si_3N_4 available in the literature has been proposed by Tomaszkiewicz. [48] His value of 67.8 ± 13 kJ/mol or 0.10 ± 0.01 eV/atom is based on fluorine combustion calorimetric measurements of a polymer-derived SiN_x compound, which included C, O, and H in significant (> 1% by atom) quantities.

Our goal here is not only to provide a value for ΔH_f of a-Si_3N_4, but more to quantify the "proximity" of empirical model to DFT optimization. In Fig. 5 we compare ΔH_f computed before and after DFT optimization. As noted before, we computed ten independent (10) models for each potential. The change in ΔH_f upon DFT optimizations can be used as a measure for how "close" an empirical model is to the DFT local minimum.

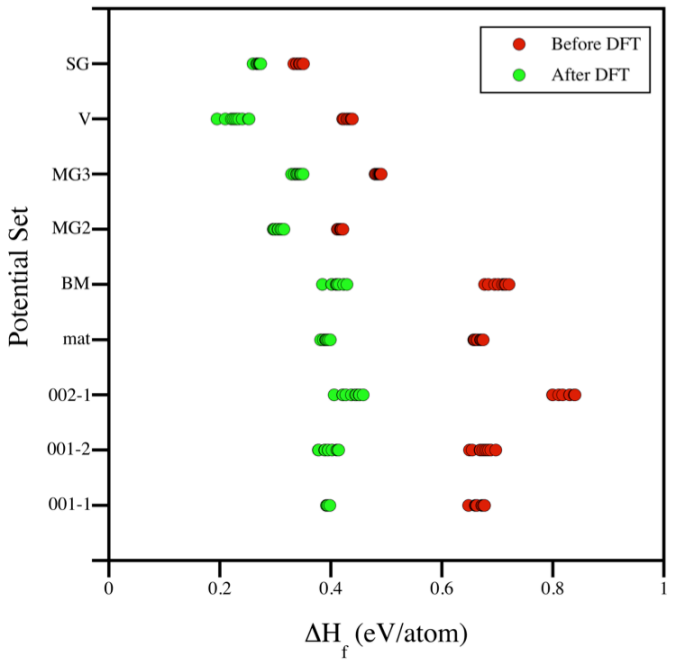

Figure 5: Enthalpies of formation ΔH_f in eV/atom of amorphous models with respect to crystalline β-Si_3N_4 compared before (red dots) and after (green dots) DFT optimization.

Tersoff models have the highest initial ΔH_f before DFT optimization, ranging from 0.65 to 0.85 eV/atom. They gain considerably in energy during DFT optimization and settle between 0.39 and 0.43 eV/atom – remarkably consistent for all the various parameterizations. The energy gain of 0.25 eV/atom, however, is significant, since it corresponds to a temperature equivalent of 2900 K. Thus, the models do not behave better than a hypothetical melt suddenly quenched from temperatures above the melting point of Si_3N_4 (2173 K, [49]). In contrast, MG2 and MG3 models start with ΔH_f of 0.41 and 0.48 eV/atom, respectively, and optimize to 0.32 and 0.35 eV/atom, respectively. Here the temperature equivalents of the energy gains are below the melting point.

Surprisingly, the two-body MG2 potential provides models with lower enthalpy of formation than the MG3 potential, although the latter was designed to "improve" the covalent character of the potential by including angular interactions. The SG potential generates models with an initial ΔH_f of 0.36 eV/atom, which is already lower than ΔH_f of best "optimized" Tersoff models. Optimizing the SG models then yields ΔH_f of 0.28 eV/atom, and the enthalpy gain during optimization corresponds to only 900 K. Models generated by the Vashishta potential start with a ΔH_f of 0.42 eV/atom and optimize to 0.20 to 0.30 eV/atom, depending on the degree of order observed in the model.

None of our models, however, exhibits a ΔH_f that comes close to the experimental value of 0.10 eV/atom. Excluding the nano-crystalline models generated by the Vashishta potential, the lowest ΔH_f values we find are 0.28 eV/atom and 0.32 eV/atom for models generated with the SG and MG2 potential, respectively. Previous DFT calculations using network models found ΔH_f of 0.27 eV/atom.[50] Using similar network models together with extensive ab-initio molecular dynamic simulations at elevated temperatures we achieve a ΔH_f as low as 0.25 eV/atom in a-Si_3N_4 models with 224 atoms. Since a typical uncertainty of similar DFT calculations is only 0.02 eV/atom, [51] the discrepancy between experimental and computed value either points to an inability to model amorphous silicon nitride using the methods described here or indicate flaws in the experimental data analysis.

Summary and Conclusion

We model a-Si_3N_4 using a combination of empirical potentials and density functional theory calculations. Empirical potentials chosen are - five parameterizations of the Tersoff potential for N (001-1, 001-2, 002-1, mat and BM), the Marian-Gastreich two-body (MG2) and three body (MG3) potential, the Vashishta (V) potential and the Garofalini (SG) potential. Models with target densities ρ = 2.6 - 3.4 $g \cdot cm^{-3}$ are generated with empirical potentials using melt-and-quench techniques and subsequently optimized within density functional theory. We compare the

"quality" of these models in terms of structural features, coordination of atoms, pair correlation functions (PCFs) and enthalpies of formation (ΔH_f) — as obtained from DFT calculations.

Our results indicate that both Garofalini (SG) and Marian-Gastreich two-body (MG2) potentials are excellent choices for empirical potential modeling of a-Si_3N_4. These potentials yield models that are relatively defect free with < 5% of under-coordinated Si or N, even before DFT optimization. Compared to this, the Tersoff models produce an excessive amount of under-coordinated Si, even after rigorous DFT optimization. Such under-coordination of atoms is unrealistic as this relates to highly reactive dangling bonds in the system. The MG3 potential has a tendency to over-coordinate atoms. Models generated using the Vashishta potential have a small fraction of under-coordination of atoms. However, melt-quench simulations with this potential yield models with nuclei of a hypothetical defect sphalerite-type of Si_3N_4, showing a strong tendency of this potential to create crystalline structures.

Analysis of pair correlation functions highlight the impact of short cut-offs for Tersoff models. Noticeable peaks build up at cut-off distances using the empirical potential, and vanish during DFT optimization. In contrast, MG2 and SG models show barely any change in their PCF. Models produced using the Vashishta potential exhibit a series of pronounced distance correlations up to 8 Å, corresponding to signature peaks of crystalline dsph-Si_3N_4.

Best estimates for the enthalpy of formation (ΔH_f) of amorphous silicon nitride, a-Si_3N_4, are 0.25 to 0.29 eV/atom, based on models generated using the SG and MG2 potentials combined with subsequent DFT optimizations. The enthalpy of formation of some Vashishta models is even lower, but due to pronounced order and formation of a hypothetical crystalline structure. Tersoff models not only exhibit the highest formation enthalpy, but also show substantial energy gain and structural changes during DFT optimizations.

In conclusion, the MG2 potential is computationally efficient, yields models with moderately low coordination defects and reasonable values for the enthalpy of formation. The SG potential is at least equally good, but requires more than twice as much CPU time to generate models. Both potentials produce structures close to the DFT ground state. Thus, we recommend that the

MG2 and SG potentials be used for future work in modeling of amorphous Si_3N_4, whenever a reasonable description of the atomistic structure is important.

Appendix:

Functional form of inter-atomic potentials

1) Tersoff Potential

The total energy of the system is given by the sum of the site-energy E_i of n atoms.

$$E = \sum_{i=1}^{n} E_i = \frac{1}{2} \sum_{i \neq j}^{n} V_{ij}$$

V_{ij} is a generalized Morse potential with a single cutoff. Thus:

$$V_{ij} = f_c(r_{ij}))\left\{ f_R(r_{ij}) + b_{ij} f_A(r_{ij}) \right\} \text{ where}$$

$$f_R(r_{ij}) = A_{ij} \exp(-\lambda_{ij} r_{ij}) \text{ and } f_A(r_{ij}) = -B_{ij} \exp(-\mu_{ij} r_{ij})$$

$$f_C(r_{ij}) = \begin{cases} 1, r_{ij} < R_{ij} \\ \frac{1}{2} + \frac{1}{2} \cos\left(\frac{\pi(r_{ij} - R_{ij})}{S_{ij} - R_{ij}} \right), R_{ij} < r_{ij} < S_{ij} \\ 0, r_{ij} < S_{ij} \end{cases}$$

The total energy, E, is the difference between attractive (f_A) and repulsive (f_R) components, which are both functions of the interatomic separation r_{ij}. The term f_C is a cut-off function that limits the range of the potential to nearest-neighbors. The attractive term (f_A) is modified by the bond-order term, b_{ij}, which impacts the "bond strength" based on the environment and accounts for three-body interaction between atoms. It is defined as:

$$b_{ij} = \chi_{ij}\left(1+\zeta_{ij}^{n_i}\right)^{\frac{1}{2n_i}}$$

$$\zeta_{ij}^{n_i} = \sum_{k\neq i,j} f_C(r_{ik})\omega_{ik}\beta_i g(\theta_{ijk})$$

$$g(\theta_{ikj}) = 1 + \frac{c_i^2}{d_i^2} - \frac{c_i^2}{d_i^2 + (h_i - \cos\theta_{ikj})^2}$$

The term ζ_{ij} defines the effective coordination number of atom i, that is, the number of nearest neighbors, taken into account the relative distance of two neighbors, r_{ij} - r_{ik}, and the bond-angle, θ. There are 13 parameters to be fitted: A, B, λ, μ, R. S, β, n, c, d, h, χ and ω. The parameters χ_{ij} and ω_{ij} address bond polarity in hetero-atomic bonds. For hetero-atomic systems the following mixing rules are used:

$$\lambda_{ij} = \frac{1}{2}(\lambda_i + \lambda_j)$$

$$\mu_{ij} = \frac{1}{2}(\mu_i + \mu_j)$$

$$A_{ij} = (A_i A_j)^{1/2}$$

$$B_{ij} = \chi_{ij}(B_i B_j)^{1/2}$$

$$R_{ij} = (R_i R_j)^{1/2}$$

$$S_{ij} = (S_i S_j)^{1/2}$$

For Si we use the parameters originally designed by Tersoff in 1989 (Table 1). For N, we use 5 different parameter sets – 001-1, 001-2, 002-1, mat and BM (included in Table 1 in section Interatomic Potentials).

Parameters	Si
A [eV]	1830.8

B [eV]	471.11
λ [Å^{-1}]	2.4799
μ [Å^{-1}]	1.7322
β [10^{-2}]	1.1x10^{-6}
n	0.78734
c	10039
d	16.217
cos q (h)	-0.59825
R (pm)	250
S (pm)	280

Table 1: Tersoff potential parameter sets for Silicon atom. [15]

2. Marian-Gastreich two-body potential (MG2) [27]

In the MG2 potential, the total energy of the system, $E_{Si\text{-}N}$, is given as a summation of 3 two-body interactions: $E_{Si-N} = E_{N-Si} + E_{Si-Si} + E_{N-N}$. The Morse potential describes both attractive and repulsive interactions between Si and N atoms. Atoms are considered non-charged and columbic repulsions between like atoms, i.e, N-N and Si-Si are reproduced by short-ranged exponentially damped 1/r-type potentials. This columbic-like potential is named as "General Potential".

$$E_{N-Si} = Morse = D_e\{(1-e^{-a(r-r_0)})^2 - 1\}$$

$$E_{N-N/Si-Si} = General = \frac{A}{r}e^{-r/\rho}$$

Finally, attractive damped dispersion forces of Tang-Toennis model are introduced to define N-N van der Waals forces in a layered system. [52]

$$E_{N-N} = -\frac{C_6}{r^6}\left(1 - e^{-b_6 r}\sum_{k=0}^{6}\frac{(b_6 r)^k}{k!}\right)$$

At large interatomic distances all two-body potentials are tapered to zero between an inner (x_i) and an outer (x_o) cutoff radius by multiplying the two-body potential energies by a fifth-order polynomial, P_5. Therefore the energy and its first and second derivatives with respect to the inter-nuclear coordinate remain continuous. The functional form of P_5 is:

$$P_5 = (x_i - x_0)\times\{-6\cdot r^5 + 15(x_i + x_0)r^4 - 10(x_i^2 + 4x_i x_0 + x_0^2)r^3 + 30(x_i^2 x_0 + x_i x_0^2)r^2 - 30x_i^2 x_0^2 r + 10x_i^2 x_0^3 + x_0^5 - 5x_i x_0^4\}$$

The various parameters of the Marian-Gastreich 2 body potential are given in Table 2.

	Potential	Parameters (units)	Values
N-Si	Morse	D_e (eV)	3.88461
		a ($Å^{-1}$)	2.32660
		r_0 (Å)	1.62136
Si-Si	General	A (eV Å)	177.510
		ρ (Å)	0.63685
N-N	General	A (eV Å)	2499.01
		ρ (Å)	0.36029

N-N	Damped dispersion	C_6 (eV Å^6)	16691.4
		b_6 (Å^{-1})	0.50328
P5	Tapering function	x_i (Å)	4.3
		x_0 (Å)	5.8

Table 2: Parameters of SiN system as defined by the Marian Gastreich two-body (MG2) potential

3) The Marian-Gastreich three-body Potential (MG3) [28]

The Marian Gastreich three-body potential, MG3, is a summation of two-body repulsive Columbic, repulsive Buckingham and attractive damped dispersion potential with the addition of the three-body Stillinger Weber (SW) potential. The SW term applies only to N-Si-N configurations only. All two-body forces are tapered to zero using fifth-order polynomial smoothing functions, thus ensuring their continuity. Unlike MG2, this potential is charged.

For SiN systems, the potential is defined as $E_{Si\text{-}N} = E_{N\text{-}Si} + E_{Si\text{-}Si} + E_{N\text{-}N}$. The analytical forms for each of these two and three body potentials along with the parameters are summarized in Table 3.

	Potential	Parameters (units)	Values
N-Si	Buckingham	A (eV)	1319.23
		ρ (Å)	0.266735
N-Si	Coulomb Taper	C (eV)	-20.4023

		r_0 (Å)	2.6
N-N	Buckingham	A (eV)	1168.10
		ρ (Å)	0.344070
N-N	Damped dispersion	C_6 (eV Å^6)	460.00
		b_6 (Å^{-1})	2.86875
Si-Si	Buckingham $E = Ae^{-r/\rho}$	A (eV)	105.19
		ρ (Å)	0.591214
N-Si-N	$E = A\left(\cos\theta - \cos\theta_0\right)^2 \exp\left[\frac{\rho}{r_{12} - r_{\max 12}} + \frac{\rho}{r_{13} - r_{\max 13}}\right]$	A (eV)	10.44
		ρ (Å)	1.0
		$r_{max12/13}$ (Å)	3.0
		θ_0 (deg)	109.47
N	Coulomb terms	q_N (a.u.)	-0.7875
Si		q_{Si} (a.u.)	1.05
P_5	Tapering function	x_i (Å)	6.00

		x_0 (Å)	8.00

Table 3: Analytical expressions and parameters of SiN system as described by the MG3 potential along with units.

4) The Vashishta Potential (V) [22]

The Vashishta potential contains both two-body and three-body terms. Unlike the Tersoff and MG2 potential, the atoms carry effective charges. The two-body terms in the potential is a sum of 3 terms – 1) steric repulsion between ions, 2) long-range screened Coulomb repulsions to account for charge-transfer effects between ions, and 3) screened charge-dipole interactions due to electronic polarizability of negatively charged ions. The three-body terms in the potential include the effects of bond bending and stretching. The analytical form of the potential is given below:

$$V = \sum_{i<j} V_{ij}^2 + \sum_{i<j<k} V_{jik}^3$$

$$V_{ij}^2 = \frac{H_{ij}}{r_{ij}^{\eta_{ij}}} + \frac{Z_i Z_i}{r_{ij}} e^{-r_{ij}/r_{1s}} - \frac{\frac{1}{2}(\alpha_i Z_j^2 + \alpha_j Z_i^2)}{r_{ij}^4} e^{-r_{ij}/r_{4s}}; H_{ij} = A_{ij}\left(\sigma_i + \sigma_j\right)^{\eta_{ij}}$$

$$V_{jik}^3 = B_{jik}\left(\frac{r_{ik} \bullet r_{ij}}{r_{ik} r_{ij}} - \cos\bar{\theta}_{jik}\right)^2 \exp\left(\frac{\gamma}{r_{ij} - r_{c3}} + \frac{\gamma}{r_{ik} - r_{c3}}\right)$$

H_{ij} and η_{ij} are the strength and exponents of the steric repulsion. Z_i and Z_j are the effective ionic charge of particle i and j and α_i and α_j are their corresponding electronic polarizability. The terms r_{1s} and r_{4s} denote screening lengths for Coulomb and charge-dipole interactions. B_{jik} is the strength of the bond stretching interaction while $\bar{\theta}_{jik}$ is a constant that incorporates bond bending. $\bar{\theta}_{jik}$ is the angle formed by by r_{ji} and r_{ki} at the vertex i. The term γ is set to 1 Å. The three-body

interaction ranges ≤ r_{c3}, which is the cutoff distance, chosen to 2.6 Å. The various parameters of the Vashishta potential and their units are tabulated in Table 4.

	Z_i (e)	α_i (Å^3)	σ_i (Å)
Si	1.472	0	0.47
N	-1.104	3	1.30
	η_{ij}		
Si-Si	11		
Si-N	9		
N-N	7		
	B_{jik} (eV)		$\bar{\theta}_{jik}$
Si-N-Si	12.484		120
N-Si-N	6.242		109.47

A_{ij} (eV)	γ (Å)	r_{1s} (Å)	r_{4s} (Å)	r_c (Å)	r_{c3} (Å)
1.248	1.0	2.5	2.5	5.5	2.6

Table 4: SiN parameters of the Vashishta Potential

5) The Garofalini Potential (SG):

The Garofalini potential was developed to study the calcium silicate inter-granular films in Si_3N_4 ceramics. The potential consists of two- and three- body terms. The two-body term consists of a short-range repulsive term and a modified Columbic term:

$$V_{ij}^{(2)} = A\exp\left(\frac{-r_{ij}}{\rho_{ij}}\right) + \frac{q_i q_j}{r_{ij}} \cdot \xi\left(\frac{r_{ij}}{\beta_{ij}}\right)$$

$$where, \xi\left(\frac{r_{ij}}{\beta_{ij}}\right) = \frac{2}{\sqrt{\pi}} \int_{r_{ij}/\beta_{ij}}^{\infty} e^{-r^2} dt$$

The Columbic term is modified by the complimentary error function, ξ, which tapers the Columbic interaction to zero. The other parameters for this two body term are A, B and ρ. Charges are denoted by $q_i = q_{Si} = +4.0$ and $q_j = q_N = -3.0$.

The three-body term is:

$$V_{jik}^{(3)} = \left[\lambda_{jik}\left(\cos\theta_{jik} - \cos\theta_{jik}^0\right)^2 \exp\left(\frac{\gamma_{ij}}{r_{ij} - r_{ij}^0} + \frac{\gamma_{ik}}{r_{ik} - r_{ik}^0}\right)\right]$$

It acts like a penalty function that raises the energy of the system when the angles between involved species deviate from their ideal value. The parameters of the SG potential are listed in Table 6.

Two-body term			
Atom pair	A_{ij} (eV)	β_{ij} (Å)	ρ_{ij} (Å)
Si–Si	1171.531	2.290	0.290
Si–N	4868.377	2.413	0.2589
N–N	451.948	2.610	0.290

Three-body term				
Atoms involved	λ_{ij} (eV)	γ_{ij} (Å)	R_{ij} (Å)	θ^0_{ij}
Si–N–Si	218.453	2.60	2.80	120
N–Si–N	149.796	2.80	3.00	109.5

Table 5: SiN parameters of the SG Potential

References

[1] F. L. Riley, J. Am. Ceram. Soc. **83**, 245 (2000).

[2] K. D. Mörgenthaler and H. Bühl, in *Tailoring of Mechanical Properties of Si_3N_4 Ceramics*, edited by M. J. Hoffmann, and G. Petzow (Springer Netherlands, Dordrecht, 1994), pp. 429.

[3] H. Klemm, J. Am. Ceram. Soc. **93**, 1501 (2010).

[4] C. E. Morosanu, Thin Solid Films **65**, 171 (1980).

[5] M. Gupta, V. K. Rathi, S. P. Singh, O. P. Agnihotri, and K. S. Chari, Thin Solid Films **164**, 309 (1988).

[6]T. P. Ma, IEEE Trans. Electron Dev. **45**, 680 (1998).

[7]J. T. Milek, *Silicon Nitride for Microelectronic Applications: Part 2 Applications and Devices* (Springer Science & Business Media, 2013).

[8] T. Ning, H. Pietarinen, O. Hyvarinen, J. Simonen, G. Genty, and M. Kauranen, Appl. Phys. Lett. **100** (2012).

[9] D. J. Moss, R. Morandotti, A. L. Gaeta, and M. Lipson, Nat. Photon. **7**, 597 (2013).

[10] I. G. Talmy, J. A. Zaykoski, and M. M. Opeka, J. Am. Ceram. Soc. **91**, 2250 (2008).

[11] B. S. Bal and M. N. Rahaman, Acta Biomater. **8**, 2889 (2012).

[12] I. Ohdomari, Y. Yamakoshi, T. Kameyama, and H. Akatsu, J. Non-Cryst. Solids **89**, 303 (1987).

[13] N. Umesaki, N. Hirosaki, and K. Hirao, J. Non-Cryst. Solids **150**, 120 (1992).

[14] P.M.Kroll, Ph.D thesis, Computersimulationen und Röntgennahkantenabsorptionsspektroskopie von Siliciumnitrid und Siliciumcarbidnitrid Keramiken, Technische Hochschule (Darmstadt, 1996).

[15] J. Tersoff, Phys. Rev. B **37**, 6991 (1988).

[16] J. Tersoff, Phys. Rev. B **39**, 5566 (1989).

[17] K. Matsunaga, Y. Iwamoto, C. A. J. Fisher, and H. Matsubara, J. Ceram. Soc. Jpn. **107**, 1025 (1999).

[18] K. Matsunaga and Y. Iwamoto, J. Am. Ceram. Soc. **84**, 2213 (2001).

[19] F. de Brito Mota, J. F. Justo, and A. Fazzio, Phys. Rev. B **58**, 8323 (1998).

[20] F. De Brito Mota, J. F. Justo, and A. Fazzio, Int. J. of Quantum Chem. **70**, 973 (1998).

[21] F. D. Mota, J. F. Justo, and A. Fazzio, J. Appl. Phys. **86**, 1843 (1999).

[22] R. Kalia, P. Vashishta, A. Nakano, W. Li, and I. Ebbsjo, in *Amorphous Insulators and Semiconductors*, edited by M. F. T. a. M. I. Mitkova (Kluwer Academic, Netherlands, 1997), p. 151.

[23] P. Walsh, R. K. Kalia, A. Nakano, P. Vashishta, and S. Saini, Appl. Phys. Lett. **77**, 4332 (2000).

[24] P. Walsh, A. Omeltchenko, R. K. Kalia, A. Nakano, P. Vashishta, and S. Saini, Appl. Phys. Lett. **82**, 118 (2003).

[25] K. Tsuruta, A. Nakano, R. K. Kalia, and P. Vashishta, J. Am. Ceram. Soc. **81**, 433 (1998).

[26] M. E. Bachlechner, A. Omeltchenko, A. Nakano, R. K. Kalia, P. Vashishta, I. Ebbsjö, and A. Madhukar, Phys. Rev. Lett. **84**, 322 (2000).

[27] C. M. Marian, M. Gastreich, and J. D. Gale, Phys. Rev. B **62**, 3117 (2000).

[28] M. Gastreich, J. D. Gale, and C. M. Marian, Phys. Rev. B **68**, 094110 (2003).

[29] S. H. Garofalini and W. Luo, J. Am. Ceram. Soc. **86**, 1741 (2003).

[30] P. Rulis, J. Chen, L. Ouyang, W. Y. Ching, X. Su, and S. H. Garofalini, Phys. Rev. B **71**, 235317 (2005).

[31] P. Kelires, Europhys. Lett. **14**, 43 (1991).

[32] F. H. Stillinger and T. A. Weber, Phys. Rev. B **31**, 5262 (1985).

[33] M. Born and J. E. Mayer, Zeitschrift für Physik **75**, 1 (1932).

[34] M. L. Huggins and J. E. Mayer, J. Chem. Phys. **1**, 643 (1933).

[35] J. E. Mayer, J. Chem. Phys. **5**, 67 (1937).

[36] S. Plimpton, J. Comput. Phys. **117**, 1 (1995).

[37] J. D. Gale, J. Chem. Soc., Faraday Trans. **93**, 629 (1997).

[38] G. Kresse and J. Furthmüller, Comput. Mater. Sci. **6**, 15 (1996).

[39] G. Kresse and J. Hafner, Phys. Rev. B **47**, 558 (1993).

[40] G. Kresse and J. Hafner, Phys. Rev. B **49**, 14251 (1994).

[41] G. Kresse and D. Joubert, Phys. Rev. B **59**, 1758 (1999).

[42] T. Aiyama, T. Fukunaga, K. Niihara, T. Hirai, and K. Suzuki, J. Non-Cryst. Solids **33**, 131 (1979).

[43] M. Misawa, T. Fukunaga, K. Niihara, T. Hirai, and K. Suzuki, J. Non-Cryst. Solids **34**, 313 (1979).

[44] W. Sheldrick, Organic Silicon Compounds Volume 1 and Volume 2 (1989)

[45] R. P. Vedula, N. L. Anderson, and A. Strachan, Phys. Rev. B **85**, 205209 (2012).

[46] L. Giacomazzi and P. Umari, Phys. Rev. B **80**, 144201 (2009).

[47] P. Kroll, J. Non-Cryst. Solids **293–295**, 238 (2001).

[48] I. Tomaszkiewicz, J. Therm. Anal. Calorim. **65**, 425 (2001).

[49] W. M. Haynes, *CRC Handbook of Chemistry and Physics, 92nd Edition* (Boca Raton, FL, 2011)

[50] P. Kroll, J. Eur. Ceram. Soc. **25**, 163 (2005).

[51] G. Hautier, S. P. Ong, A. Jain, C. J. Moore, and G. Ceder, Phys. Rev. B **85**, 155208 (2012).

[52] K. T. Tang and J. P. Toennies, J. Chem. Phys. **80**, 3726 (1984).

Appendix 3:

One of the major acheivements in this project is the successful implementation of the MG2 potential in LAMMPS. [1, 2] Thus far, the MG2 potential has been available exclusively as a part of the GULP and TREMOLO-X packages. [3] [4] TREMOL-X is a single-user licenced product. The GULP package, while free, is computationally expensive for simulations involving more than 100 atoms. In the next section, I document the steps involved to include the MG2 potential in LAMMPS. The description consists of some "coding-jargon" intended for its target audience.

A3.1) Implementing Marian-Gastreich Potential in Lammps:

As discussed before, the Marian-Gastreich potential is a sum of two-body interactions in the form: $E_{pot\ Si/N} = E_{N\text{-}Si} + E_{Si\text{-}Si} + E_{N\text{-}N}$; where E is the two-body potential energy.
While Morse and Columbic forces depict Si-N and Si-Si interactions, N-N interactions are defined as repulsive only and described by exponentially damped 1/r potentials of the form $E = (A/r)\exp^{-r/\rho}$. This kind of interaction resembles Columbic type and is named as "General potential" by the authors of the paper. Damped dispersion forces of the Tang-Toennies model describe N-N interactions. [5] This interaction has been added to ensure that the correct layer structures of crystalline hexagonal and rhombohedral BN is provided. Furthermore, in the MG2 potential, all two-body potentials are tapered to zero by multiplying energy and forces by a fifth-order polynomial, P_5, for 4.3 Å < r < 5.8 Å, where r is the interatomic distance.

In Lammps, the Morse Potential is readily available. To implement the General and Damped Dispersion potential, I "modify" the Born-Meyer-Huggins and the Buckingham Potentials. [6] [7] [8] [9]

The Born-Mayer-Huggins potential has the form:

$$E = A\exp\left(\frac{\sigma - r}{\rho}\right) - \frac{C}{r^6} + \frac{D}{r^8}$$

Where: r is the pairwise interatomic distance $|r_1 - r_2|$; A describes the components of the repulsive interaction; C & D are dipole-dipole and dipole-quadrupole interaction constants; σ is a value at which E(r = σ) = 0; ρ depends on the size and "softness" of ions.

This potential can also be written as:

$$E = A\exp\left(\frac{-r}{\rho}\right)$$

with σ, C and D = 0.

I modify the computation of the energy and forces of the BMH potential in LAMMPS by multiplying with variable *rinv* (1/r) in the lammps module *pair_born.cpp*. Moreover, a conditional if-block loop is added to include the tapering cutoffs. The if-block is as follows:

```
x0 = 5.8, xi = 4.3;
if (r > xi & r < x0)
      {
…
eborn = eborn * p5
fborn = forceborn * p5
      …
      }
```

Recall that at large interatomic separations all two-body potentials are smoothly tapered to zero by multiplying by a fifth-order polynomial, P_5 as:

$$P_5 = (x_i - x_0)^{-5} * \{-6r^5 + 15(x_i + x_0)r^4 - 10(x_i^2 + 4x_i x_0 + x_0^2)r^3 + 30(x_i^2 x_0 + x_i x_0^2)r^2 - 30x_i^2 x_i^2 r + 10x_i^2 x_i^3 + x_0^5 - 5x_i x_0^4\}$$

Similarly, the Buckingham Potential is of the form:

$$E = Ae^{-r/\rho} - \frac{C}{r^6}$$

where A, ρ and C are parameters to be fitted. If C = 0, this potential becomes a Born-Mayer type.

The analytical form can be written to match the damped dispersion forces in the MG2 potential:

$$E = -\frac{C_6}{r^6}\left(1 - e^{-b_6 r}\sum_{k=0}^{6}\frac{(b_6 r)^k}{k!}\right)$$

with $A = -C_6/r^6$, $1/\rho = b_6$ and $C = C_6$

Incorporating this potential form in LAMMPS is done by modifying the *pair_buck.cpp* module. A code snippet is included here:

Variable description: ebuck = Energy E(r); i/j-type = particle identifier; r6inv = $1/r^6$; rhoinv = (1/ρ); rexp = $e^{-r*\frac{1}{\rho}}$; pow is a pre-defined function in C++ that returns the value of a number raised to the power exponent: $number^{exponent}$

…

*ebuck = -c[itype][jtype]*r6inv * (1 - rexp*(pow(rhoinv[itype][jtype]*r, 0)/1 + pow(rhoinv[itype][jtype]*r, 1)/1 + pow(rhoinv[itype][jtype]*r, 2)/2 + pow(rhoinv[itype][jtype]*r, 3)/6 + pow(rhoinv[itype][jtype]*r, 4)/24 + pow(rhoinv[itype][jtype]*r, 5)/120 + pow(rhoinv[itype][jtype]*r, 6)/720));*

…

Once again, the interatomic distances are tapered to zero by multiplying with P5.

After the modules are altered, it is important to compile LAMMPS. Finally the simulation is set up with the description of the inter-atomic potential as:

…

#Defining the potential

pair_style hybrid/overlay morse 6.0 born 6.0 buck 6.0

pair_coeff 1 2 morse 3.88461 2.32660 1.62136

pair_coeff 2 2 buck 0.0 1.986965506 16691.4

pair_coeff 2 2 born 2499.01 0.36029 0.0 0.0 0.0

pair_coeff 1 1 born 177.510 0.63685 0.0 0.0 0.0

…

A3.2) Comparison between MG2 potential as implemented in LAMMPS and GULP: A case study with a-Si_3N_4

In this section I compare two 448 atom models of a-Si_3N_4 – 1) generated in LAMMPS using my implementation of MG2 potential; 2) generated using GULP with the built-in MG2 potential.

Both models are generated using a melt-and-quench scheme. Atoms are placed randomly in a box and heated to 5000 K for 10 ps (heating rate = 4.7 x 10^{14} K·s^{-1}) and then quenched/cooled to 300 K in 105 ps (cooling rate = 4.5 x 10^{13} K·s^{-1}). Density is chosen to be 3.2 g·cm^{-3}. For each structure, I compare coordination defects present in the model: namely, the number of 2, 4 and 5 coordinated N atoms and the 5 and 6-coordinated Si. The differences between both methods are negligible. Moreover, if 100 models such models are considered and their coordination defects compared, the differences between results from LAMMPS and GULP vanish.

As expected, the biggest difference between both platforms was the computation time. LAMMPS is computationally less expensive compared to GULP. LAMMPS computes models hundredfold faster than GULP (30 μs/atom/step in GULP compared to 0.3 μs/atom/step in LAMMPS). Computations are done on a local cluster with 12 cores.

Atom [Coordination]	LAMMPS	GULP
N [2]	10	9
N [4]	42	47
N [5]	1	0
Si [5]	32	34

Si [6]	1	1
Bond length, Si-N (Å)	1.77	1.78

Table A3.2: Comparison of coordination defects between a-Si_3N_4 model consisting of 448 atoms, generated by LAMMPS and GULP using a melt-and-quench scheme.

References:

[1] C.M. Marian, M. Gastreich, J.D. Gale, Physical Review B, 62 (2000) 3117-3124.

[2] S. Plimpton, J Comput Phys, 117 (1995) 1-19.

[3] J.D. Gale, Journal of the Chemical Society, Faraday Transactions, 93 (1997) 629-637.

[4] M. Griebel, S. Knapek, G. Zumbusch, Numerical Simulation in Molecular Dynamics: Numerics, Algorithms, Parallelization, Applications, Springer Publishing Company, Incorporated, 2010.

[5] K.T. Tang, J.P. Toennies, The Journal of Chemical Physics, 80 (1984) 3726-3741.

[6] M. Born, J.E. Mayer, Zeitschrift für Physik, 75 (1932) 1-18.

[7] M.L. Huggins, J.E. Mayer, The Journal of Chemical Physics, 1 (1933) 643-646.

[8] J.E. Mayer, The Journal of Chemical Physics, 1 (1933) 270-279.

[9] R.A. Buckingham, Proceedings of the Royal Society of London. Series A. Mathematical and Physical Sciences, 168 (1938) 264.

Summary:

Amorphous Si_3N_4 has many industrial and technological applications. While this material is experimentally synthesized, numerous computational studies aim to study the micro-structure of the material. Most prevalent methods to model a-Si_3N_4 use an empirical potential to describe the inter-atomic interaction. However, the results of each study vary and often purely depend on the flavor of empirical potential used. The graph below shows that the Tersoff potential is the most-cited potential with none of the other potentials coming close.

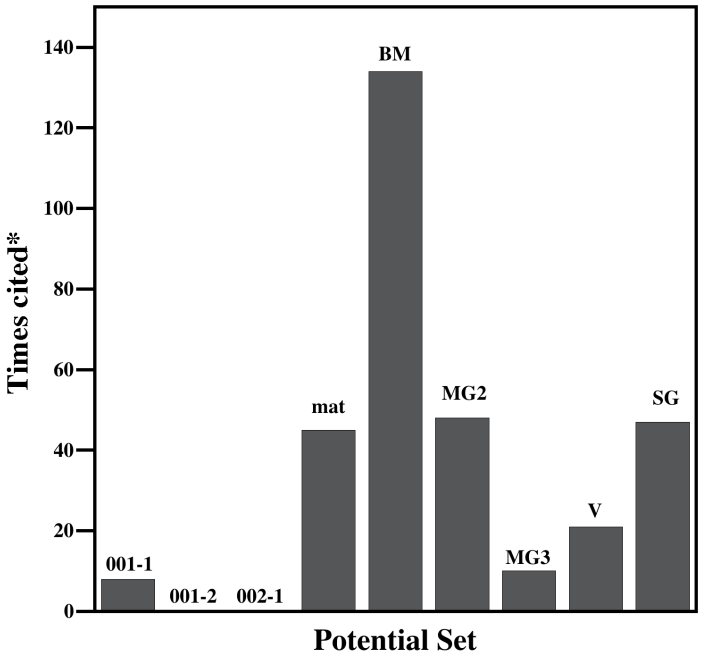

Figure 1: Plot of empirical potentials against the number of times they have been cited in literature. Abbreviations: 001-1, 001-2 and 002-1, mat and BM - Tersoff potential training sets from [1-4]. The *mat* parameters are similar to 001-1 except for ω_{Si-N}. V stands for Vashista Potential, [5] MG2 is for 2 –body Marian Gastriech potential, [6] MG3 is the 3 body Marian Gastriech potential [7] and SG is Garofalinin potential. [8]

*Data is from Web of Science and doesnot include self citations by authors. The number of citations of 001-1 potential may be wrong and is to be re-used with caution.

This study aims to project the Garofalini and the Marian Gastreich two-body potential as ideal potentials to model amorphous Si_3N_4. Moreover, due to the successful implementation of the MG2 potential in LAMMPS, multi-million atom models can be constructed within realistic time frames.

References:

[1] P.M.Kroll, Computersimulationen und Röntgennahkantenabsorptionsspektroskopie von Siliciumnitrid und Siliciumcarbidnitrid Keramiken, Technische Hochschule Darmstadt, Darmstadt, Germany, 1996.

[2] K. Matsunaga, Y. Iwamoto, Molecular dynamics study of atomic structure and diffusion behavior in amorphous silicon nitride containing boron, J. Am. Ceram. Soc. 84(10) (2001) 2213-2219.

[3] F. de Brito Mota, J.F. Justo, A. Fazzio, Structural properties of amorphous silicon nitride, Phys. Rev. B 58(13) (1998) 8323-8328.

[4] F. De Brito Mota, J.F. Justo, A. Fazzio, Structural and electronic properties of silicon nitride materials, Int. J. of Quantum Chem. 70(4-5) (1998) 973-980.

[5] R.Kalia, P. Vashishta, A. Nakano, W. Li, and I. Ebbsjo, Molecular Dynamics Methods and Large-Scale Simulations of Amorphous Materials, in: M.F.T.a.M.I. Mitkova (Ed.), *Amorphous Insulators and Semiconductors*, Kluwer Academic, Netherlands, (1997), p. 151.

[6] C.M. Marian, M. Gastreich, J.D. Gale, Empirical two-body potential for solid silicon nitride, boron nitride, and borosilazane modifications, Physical Review B 62(5) (2000) 3117-3124.

[7] M. Gastreich, J.D. Gale, C.M. Marian, Charged-particle potential for boron nitrides, silicon nitrides, and borosilazane ceramics: Derivation of parameters and probing of capabilities, Physical Review B 68(9) (2003) 094110.

[8] S.H. Garofalini, W.W. Luo, Molecular dynamics simulations of calcium silicate intergranular films between silicon nitride crystals, J Am Ceram Soc 86(10) (2003) 1741-1752.

CHAPTER 4

COMPOSITIONAL AND STRUCTURAL ATOMISTIC STUDY OF THE AMORPHOUS SI-B-N NETWORKS OF INTEREST FOR HIGH-PERFORMANCE COATINGS[4]

[4] This chapter has been published in Journal of Physical Chemistry C and is being used with the permission of the publisher, 2016. My contribution to this article is the computation of thermal conductivity using Green Kubo method, more details are included in the Appendix.

Scope and Motivation

Thermal conductivity of solids is a critical property in several technological applications. [1] Fourier's law defines thermal conductivity as the diffusion of heat in a temperature gradient. The temperature gradient (∇T) is related to the heat flux ($\mathbf{J}$) through κ, the thermal conductivity tensor: $\mathbf{J} = -\kappa(\nabla T)$. In solids, electrons and phonons transport heat. For insulators, the contribution of electrons to thermal conductivity is negligible due to the lack of free electrons. In crystalline solids, the thermal conductivity increases initially with a T^3 dependency, passes through a maximum and decreases with increasing temperature due to strong phonon-phonon scattering. Hence, a dome-shaped curve as shown in Fig. 1. [2] In amorphous solids thermal conductivity increases with increasing temperature. The mechanism of heat transfer is primarily by localized lattice vibrations rather than extended phonons due to the lack of long-range order.

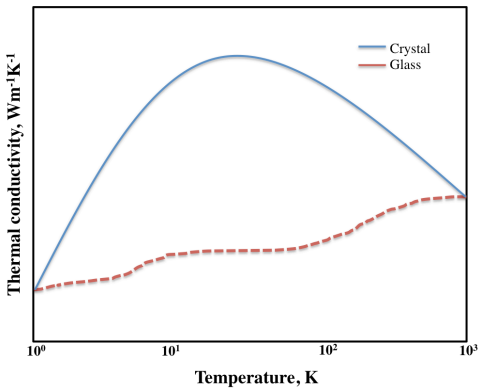

Figure I4.1: Temperature dependence of the thermal conductivity of a crystal (solid line) and a glass (dotted line).

Through computational methods, one can model advanced materials with tailored thermal conductivity for use in microelectronics, thermal insulators and thermal coatings. [1] Several methods exist to compute the κ in amorphous materials – phenomenological models, equilibrium molecular dynamic (MD) simulations and Müller-Plathe non-equilibrium MD simulations. [3-5]

In this chapter, I investigate the thermal conductivity of amorphous silicon boron nitride (a-SiBN) material using the molecular dynamics method.

Amorphous mixtures of silicon nitride (Si_3N_4) and boron nitride (BN) are refractory ceramics that are stable up to 2000 °C. This material is also resistant to oxidation up to 1400 °C. Industrial applications of these ceramics exist as coatings and fibres. The work in this chapter is in collaboration with University of Minnesota. Small network models of a-SiBN, with varying amount of BN (0 - 90 mol %), are composed with 100 - 200 atoms. These models are then subjected to the empirical Tersoff potential and their κ at 300 K investigated. The goal is to assess how the addition of BN impacts thermal conductivity in these materials. The chapter is organized as follows: first the peer-review journal article is included. After the article the appendix is where I include temperature dependent thermal conductivity data a-SiBN models that were independently done by me.

References

[1] D.R. Clarke, C.G. Levi, Materials design for the next generation thermal barrier coatings, Annu. Rev. Mater. Res. 33 (2003) 383-417.

[2] V. Murashov, M.A. White, Thermal Conductivity of Insulators and Glasses, in: T.M. Tritt (Ed.), Thermal Conductivity: Theory, Properties, and Applications, Springer US, Boston, MA, 2004, pp. 93-104.

[3] R.O. Pohl, The applicability of the Debye model to thermal conductivity, Zeitschrift für Physik 176(4) (1963) 358-369.

[4] S. Stackhouse, L. Stixrude, Theoretical Methods for Calculating the Lattice Thermal Conductivity of Minerals, Rev. Mineral. Geochem. 71 (2010) 253-269.

[5] M. Alaghemandi, E. Algaer, M.C. Böhm, F. Müller-Plathe, The thermal conductivity and thermal rectification of carbon nanotubes studied using reverse non-equilibrium molecular dynamics simulations, Nanotech. 20(11) (2009) 115704.

Compositional and Structural Atomistic Study of the Amorphous Si-B-N Networks of Interest for High-Performance Coatings

Jihong Al-Ghalith, Atreyi Dasmahapatra, Peter Kroll, Efstathios Meletis, and Traian Dumitrica

Department of Mechanical Engineering, University of Minnesota, 111 Church Street SE, Minneapolis, MN 55455, USA

Department of Chemistry and Biochemistry, University of Texas at Arlington, 700 Planetarium Place, Arlington, TX 76019, USA

Department of Materials Science and Engineering, University of Texas at Arlington, 501 West First St., Arlington, TX 76019, USA

Abstract:

We explore by computational modeling the effects of Boron (B)-Nitrogen (N) composition on the thermal and mechanical properties of amorphous Silicon-Boron-Nitride (Si-B-N), a synthetic ceramic material with superior thermal protection, mechanical and oxidation resistance at high temperatures attributes. Network-derived Si-B-N models optimized with ab initio molecular dynamics, serve as input structures for classical molecular dynamics simulations. Atomistic Green-Kubo simulations on relaxed super-cells and structural relaxations on strained cells are used to screen the thermal and mechanical properties of a collection of network structures with low enthalpies. We find that when the material is composed of well-mixed parts rather homogeneously spread within the material, the thermal conductivity and elastic constants are isotropic and exhibit a weak dependence on composition and network structure. In contrast, when separation into BN-rich layers occurs, the material exhibits anisotropic behavior, with an increase in thermal conductivity along the layer direction and decrease in elas-tic constant in the cross-layer direction. The insights provided into the composition-structure-property relationships can be useful for the rational design of amorphous Si-B-N materials targeting high-performance coating applications.

1. Introduction

Ultra-high temperature ceramics are a class of synthetic materials with superior thermal, mechanical, and oxidation resistance properties. They have various industrial applications including space shuttle thermal protection system materials [1, 2] and high temperature resistant coatings. [3,4] One focus of protective coating research has been amorphous (a) Si_3N_4 containing (a-Si-B-N), in particular a-$Si_3B_3N_7$ [5] — a ternary material synthesized via the sol-gel route. [6] Especially because of the experimental difficulties associated with the structural characterization of amorphous materials, computer simulations are playing an important role in understanding the structure-properties relationship. Important experimental results have been already reproduced by atomistic calculations carried out on computer-generated networks. For example, molecular dynamics (MD) simulations found that the a-$Si_3B_3N_7$ networks exhibit a very high resistance against crystallization, up to 1,900 K. [7,8] In good agreement with experimentation, [9] MD simulations also predicted that the a-$Si_3B_3N_7$ bulk modulus ranges between 50–250 GPa, depending on its density. [10] In recent years, atomistic simulations are assuming a guiding role in the effort of optimizing the properties of advanced coating materials. [11–15] In a-Si-B-N, understanding the role played by composition is of great importance for the future design of this new material.

So far, a-Si-B-N structures have been explored to understand the impact of the BN:Si3N4 ratio onto mechanical properties. [9,10,16,17] Using classical MD simulations, Griebel et al. [16] derived strain-stress curves of selected a-Si_3BN_5, a-$Si_3B_2N_6$ and a-$Si_3B_3N_7$ models and found that increasing the B content increases the Young's modulus. In this work we extend the scope of the previous studies by revealing how composition and structure might influence a combination of properties desirable for coating applications. Using a combination of atomistic numerical methods, we screen a library of low-enthalpy a-Si-B-N networks — a-Si_3BN_5, a-$Si_3B_3N_7$, and a-$Si_3B_9N_{13}$ — to predict from extensive atomistic simulations the thermal conductivity and

mechanical stiffness at different BN content. This paper is organized as following: Section II describes the numerical methods of investigations, Sections III and IV presents our simulation results, and Section V gives the conclusions.

2. Methods

One of the most difficult tasks of the present work is to compose realistic structural models for a-Si-B-N structures. Instead of attempting to simulate the formation process of a-Si-B-N, we adopted an energy minimization protocol described next. We start by constructing chemically-ordered random networks generated using a modified Wooten-Winer-Weaire al-gorithm. [18] After the network generation, which uses classical empirical potentials, we turn to Density Functional Theory (DFT) calculations as implemented in the Vienna Ab-Initio Simulation package (VASP). [19–21] We first optimize structures (positions and cell parameters) using a cut-off of 500 eV, while converging forces to smaller than 10 meV/Å and stresses below 0.1 GPa. We use the Projector Augmented Wave [22,23] method together with the Generalized Gradient Approximation of electron exchange and correlation. The Brillouin zone was sampled using the Γ-point only. Subsequently, we start an annealing procedure using ab initio molecular dynamics (aiMD). We use a time-step of 2 fs for integrating the equations of motion and adjust temperature via velocity rescaling. To save computational costs, we reduce the cutoff energy to 205 eV. Starting at 300 K, the temperature of the system is ramped to 3400 K with 400 K increments. The holding time at each temperature varies between 6 ps and 40 ps, with shorter periods spent at lower temperatures and longer periods at higher temperatures. Every 2 ps of a simulation we copy the current positions of atoms and optimize this geometry separately, while the annealing continues. This way we receive a sequence of structures, some of which have lower energy than the initial configuration. After completion of an annealing run, we repeat the annealing procedure using the lowest energy model found as the initial configuration of a new run.

Due to the large computational costs associated with ab initio calculations, we will explore the properties of the aiMD generated networks with inter-atomic potential energy models. The lower computational cost for the classical Hamiltonian enables a more accurate spatial representation of the disordered networks and a more efficient screening of the structure-composition-property relationship. The classical MD calculations were performed with the code LAMMPS. [24] We treat the Si-N and B-N interactions with the bond-order Tersoff potential and parameters given in Ref. [25]. For Si-Si, N-N, B-B and Si-B, only repulsion is modeled because these bonds are not present in the aiMD-derived structures and are unlikely to appear in experiment. [26] Additionally, it is known that the homo-elemental N-N bonds are energetically unfavorable. [27] The thermal and mechanical properties of the structures treated with the Tersoff potential were extracted as it is described next.

Because a-Si-B-N are insulators electronically, phonons are the main thermal energy carriers. We have computed their thermal conductivity (κ) in the classical limit from long equilibrium MD runs. In preparation for measurements, the supercells constructed based on the aiMD annealed structures were first evolved in the isothermal-isobaric ensemble at the desired temperature and a pressure of 0 bar for 400 ps, then in the canonical ensemble for 200 ps, and finally in the microcanonical ensemble for another 200 ps in order to achieve good equilibration. We compute the instantaneous microscopic heat current on the MD-generated micro states, as

$$\mathbf{j} = \frac{1}{V}\left[\sum_{i,j,k\neq i\neq j}\frac{1}{2}r_{ij}\left(\mathbf{F_{ij}v_i}\right) + \frac{1}{6}\sum_{i,j,k\neq i\neq j}\frac{1}{2}(r_{ij}+r_{ik})\left(\mathbf{F_{ijk}v_i}\right)\right] \quad (1)$$

Then κ was extracted with the Green-Kubo formula. [28]

$$\kappa_{\alpha\beta} = \frac{V}{k_B T^2}\int_0^{+\infty}\langle j_\alpha(\tau)j_\beta(0)\rangle\, d\tau \quad (2)$$

In these expressions, indexes i, j and k run over the number of atoms. $\mathbf{r}_{ij}$ is the interatomic distance vector, **v** is the atomic velocity, and **F** the interatomic force. T is the average temperature. $\kappa_{\alpha\beta}$ is a component of the lattice thermal conductivity tensor (α and β = x, y, z). k_B is the Boltzmann constant and V the system volume. The angular brackets denote the ensemble

average, and is the autocorrelation time. In practice, κ was calculated by discretizing the right-hand side of eq. (2) in MD time steps, each of 0.15 fs.

To gain insight into the mechanical behavior, we have examined the response to applied strains of a-Si-B-N structures described with the same Tersoff potential. Since the analysis is focused on the linear regime, we simulated cells with ~1 nm side lengths placed under periodic boundary conditions. External strain was applied by elongating the simulation box size in one direction by 0.02 Å at each iteration, followed by conjugate gradient energy minimization. The specimens were allowed to shrink or expand in the other two directions to ensure that the system is under uniaxial loading. The corresponding potential energies were then recorded for each step of strain. The stress and Young modulus (Y) along a specific direction were calculated from the first and second derivative of the total potential energy with respect to the strain, normalized by the cross-sectional area. For each considered structure, external strain was applied in all three cartesian directions.

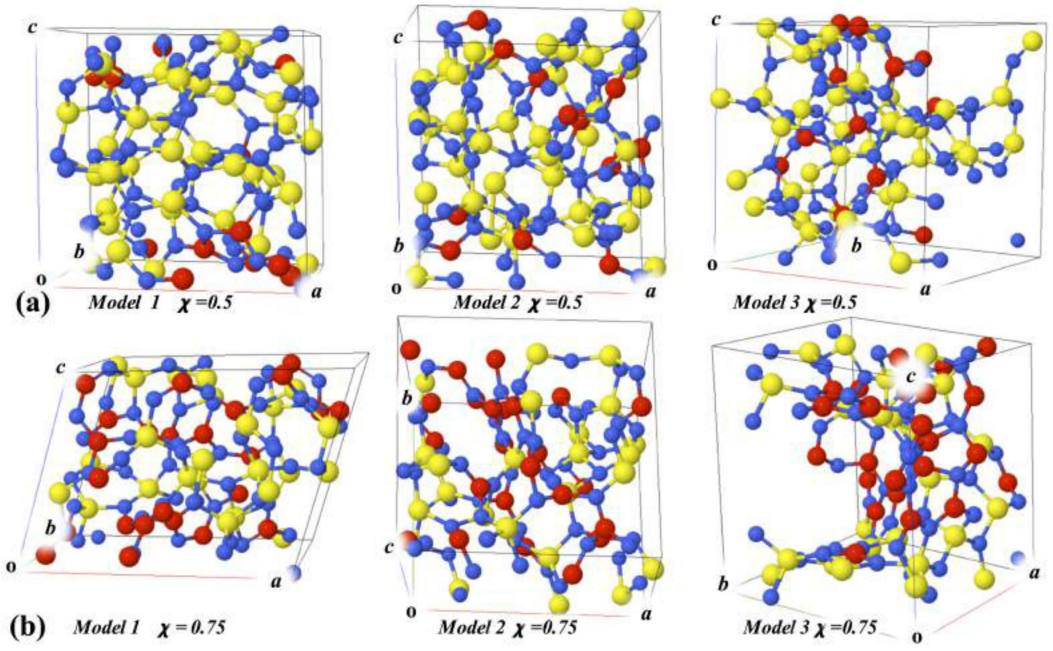

Figure 1. Unit cells of (a) a-Si_3BN_5 ($\chi = 0.5$) and (b) a-$Si_3B_3N_7$ ($\chi = 0.75$) models. Models 1–3 are nearly homogeneous. Color scheme: Si (yellow), B (red), N (blue).

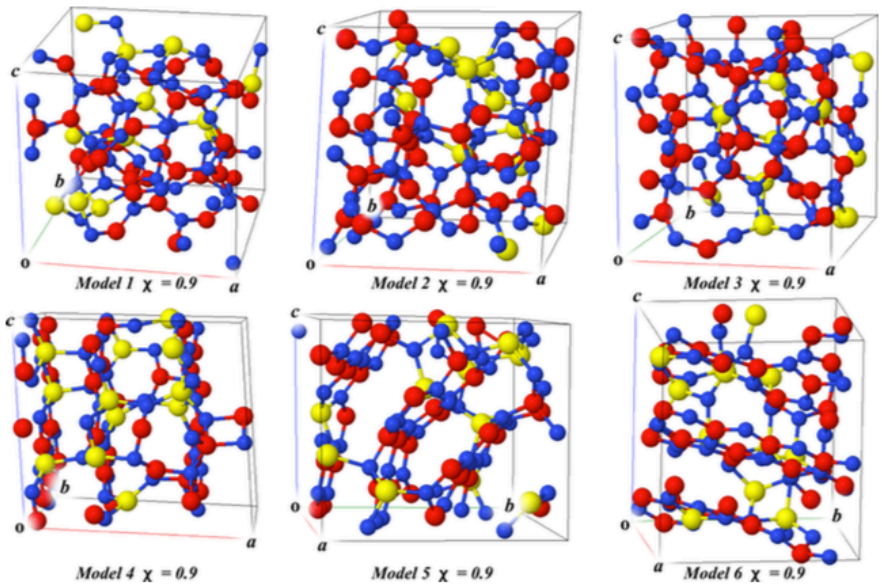

Figure 2. Unit cells of a-$Si_3B_9N_{13}$ ($\chi = 0.9$) models. Models 1–3 (top row) are nearly homogeneous. Models 4–6 (bottom row) present h-BN segregation. Color scheme: Si (yellow), B (red), N (blue).

3. Structures and energetics of a-Si-B-N networks

3.1. Ab-initio Molecular Dynamics Models

Figs. 1 and 2 presents the collection of structures that will be considered in this study. It can be seen that the search for local minima process generates nearly cubic unit cells containing about hundred atoms. The lattice parameters, densities of selected structures at each of the considered stoichiometry and the number of under-coordinated atoms are presented in Table 1. According to our definition, Si, B, and N atoms are under-coordinated if they have less than 4, 3, and 3 first neighbors, respectively, within the cut-off distances set as 20% larger than the experimental values of Si-N and B-N bond lengths of 1.72 Å and 1.43 Å, respectively. [5] We see that for all , the employed aiMD generation procedure gives models with very few or no under-coordinated atoms.

The network generation process produces nearly-homogeneous a-Si-B-N structures. Only when looking at the second-nearest neighbor statistics, these structures present a slight trend for B-N-B preference. [18] But for the high BN content structure $Si_3B_9N_{13}$ we also find segregation of h-BN layers. Fig. 2 shows examples of model structures without (models 1-3) and with (models 4-6) h-BN layers containing Si atoms. It can be observed that the h-BN layers are connected by covalent Si-N and B-N bonds. Similar BN phase segregation was found previously in B-doped Si_3N_4/SiC ceramics. [30]

Because of the h-BN segregation effect, we have also included in our study BN rich structures that were not fully relaxed. Specifically, we have considered an a-BN system taken from the very first annealing cycle after relaxing the model obtained after 7 ps in an aiMD at 2,200 K. This “intermediate" model, listed in the last column of Table 1, serves the purpose of having a balance between 3- and 4-fold coordinated B.

The DFT energies E(a-Si-B-N) of the computed networks cannot be used directly to compare the stability of structures with identical compositions. The relative stability of structures with different compositions depends on the way the structural parts BN and Si3N4 mix to form the network. Therefore, we follow here the approach of binary phase thermodynamics and define for the quasi-binary composition $(BN)_\chi(Si_3N_4)_{1-\chi}$ a per-atom enthalpy of formation, ΔH_f , as:

$$\Delta H_f = \frac{E_{a-SiBN}(\chi) - n_p[(1-\chi)E_{a-Si3N4} + \chi E_{BN}]}{n_a} \quad (3)$$

Here n_p is the number of BN and Si_3N_4 parts in the structures. For example, a-$Si_3B_3N_7$ comprises three parts BN and one part Si_3N_4. Thus, $n_p = 4$ and $\chi = 0{:}75$. We propose to measure ΔH_f with respect to the crystalline β-Si_3N_4 and h-BN phases. Thus, we take $E_{\beta\text{-}Si3N4} = 58.69$ eV and $E_{h\text{-}BN} = 17.89$ eV, which are the energies computed with DFT. n_a is the number of atoms in one a-Si-B-N unit.

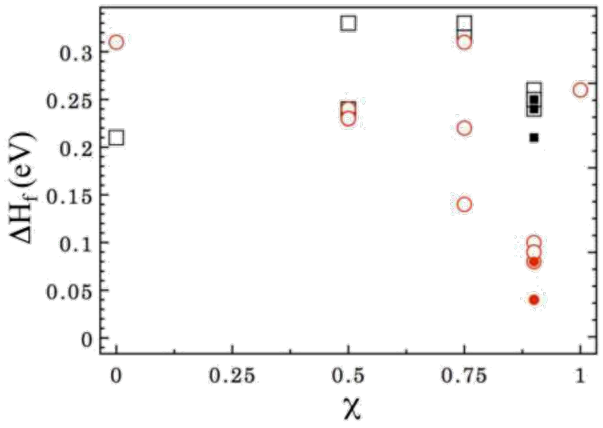

Figure 3: Per-atom enthalpy of formation of $(BN)_{\chi}(Si_3N_4)_{1-\chi}$ structures plotted as a function of χ, which is the BN molar fraction. Circles (○, ●) represent the Tersoff data while squares (□, ■) are the DFT data. Open symbols (○, □) refer to the nearly-homogeneous structures. Filled symbols (●, ■) refer to the structures presenting h-BN layer segregation.

Fig. 3 plots the calculated ΔH_f for selected network structures with lowest DFT energies at each considered. Our data doesn't reveal significant distinctions in the thermochemical stability of the structures with various. The $\chi = 0{:}9$ structures emerge as only slightly more stable than the $\chi = 0{:}75$ ones. The different models with same χ are close in energy. As it can be noted from Fig. 2(b), models 2 and 3 with $\chi = 0.75$ present rather large voids in their network structure. This structural aspect does not reflect in the ΔH_f values, which were both calculated as 0.33 eV/atom. A similar observation about the role of structure can be made at $\chi = 0{:}9$, where we identified significant segregation of the h-BN layers: In Table 2 we compare $\chi = 0{:}9$ structures with and without h-BN layer segregation. It can be seen that both structure types present similar densities and ΔH_f values.

Table 1: Comparison of Selected a-Si-B-N cells with different χ Values, Described with DFT and Tersoff models.

χ	0.00	0.50*	0.75*	0.90*	1.00
No. of atoms	112	108	104	100	256
Lattice lengths (Å)					
a	12.05	10.49	12.32	10.19	13.06
b	10.12	10.27	9.35	9.99	12.52
c	9.75	10.22	9.24	9.31	12.77
Lattice angles					
α (deg)	85.62	88.78	95.85	83.54	88.05
β (deg)	88.61	91.78	70.97	91.31	93.17
γ (deg)	95.62	87.44	98.27	88.75	88.69
Density (g/cm3)	3.16	2.99	2.87	2.57	2.53
DFT model with van der Waals correction					
ΔH_f (eV/atom)	0.21	0.24	0.32	0.26	-
no. of under-coordinated atoms	3	0	0	0	0
Tersoff model					
Hf (eV/atom)	0.31	0.24	0.14	0.08	0.26
no. of under-coordinated atoms	2	0	0	0	1

[a]Model 1 in Figs. 7 and 8(b). [b]with van der Waals correction [c]UC = undercoordinated atoms

Table 2: Comparison of χ = 0:9. Cells Described with DFT and Tersoff models.

Model:	1	2	3	4	5	6
no. of atoms	100	100	100	100	100	100
Lattice lengths (Å)						
a	10.19	9.43	9.70	10.25	9.26	9.88
b	9.99	9.84	9.90	9.36	10.47	9.06
c	9.31	9.76	9.82	9.37	9.17	9.97
Lattice angles						
α (deg)	83.54	85.44	89.15	87.82	91.47	88.94
β (deg)	91.31	86.84	88.21	94.66	89.61	93.46
γ (deg)	88.75	90.64	91.52	95.59	86.94	89.42
Density (g/cm3)	2.57	2.68	2.56	2.71	2.72	2.71
DFT model[b]						
Hf (eV/atom)	0.26	0.24	0.25	0.24	0.25	0.21
No. of UC atoms[c]	0	0	0	1	1	0
Tersoff model						
Hf (eV/atom)	0.08	0.10	0.09	0.08	0.04	0.04
No. of UC atoms[c]	0	0	0	7	1	0

[a]Models 1-3 are nearly-homogeneous. Models 4-6 present h-BN segregation. All these models were considered in Figs. 7 and 8(b). The unit cells for these models are shown in Fig. 2. [b]with van der Waals correction [c]UC = undercoordinated atoms

3.2. Tersoff Models

We have next investigated these network structures with the Tersoff potential description. The atomic positions were further allowed to relax [29] via energy minimization to the new equilibrium positions. From Tables 1 and 2, it can be seen that the relaxed structures present very few under-coordinated atoms, a feature that is in agreement with the original DFT network structures. The energies of the relaxed structures were used to compute ΔH_f. For consistency, we have used as references $E(Si_3N_4)$ = 38.46 eV and E(h-BN) = 15.13 eV, which are the per-unit energies computed with Tersoff potential. As it can bee seen from Fig. 3 and Tables 1 and 2, the Hf values computed with the Tersoff potential are generally in good agreement with the DFT ones. There is a trend of the Tersoff model to underestimate (overestimate) H_f at large (small).

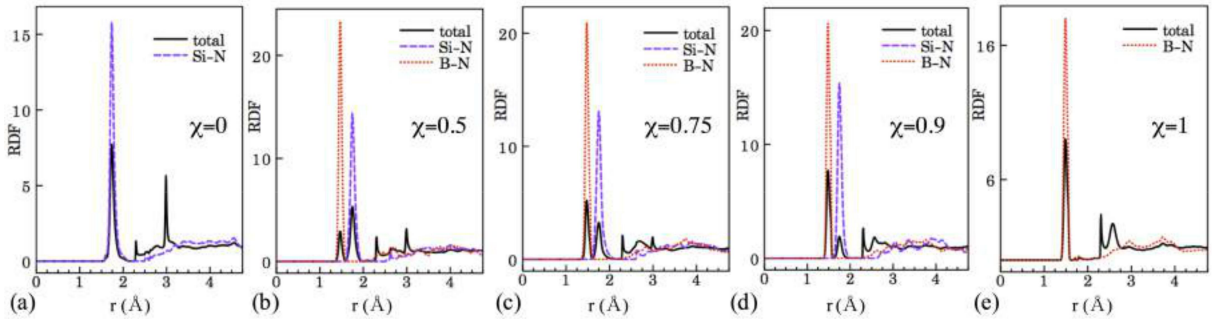

Figure 4: Radial distribution function for a set of a-Si-B-N structures with different χ: (a) a-Si_3N_4, (b) a-Si_3BN_5, (c) a-$Si_3B_3N_7$, (d) a-$Si_3B_9N_{13}$, (e) a-BN.

We have also probed the structural description of the a-Si-B-N networks in the MD context. We have evolved at 300 K for 100 ps our set of a-Si-B-N structures with a velocity Verlet algorithm and a 0.15 fs time step, and characterized the atomistic structure of the homogeneous a-Si-B-N networks by computing the radial distribution function (RDF). RDF describes the likelyhood of finding a neighboring atom in the spherical shell of a central atom. The interatomic potential cut-

off radii in our simulations are 2.62 Å and 1.79 Å for Si-N and B-N interactions, respectively. As shown in Fig. 4, only Si-N and B-N bonds are located within the potential cut-off radius. We note also that for the = 0:75 structure, the RDF peaks at 1.75 Å for Si-N and 1.47 Å for B-N are very close to the experimental values of 1.72 Å and 1.43 Å, respectively.5 This agreement indicates that the short-range order is well described by our classical MD approach.

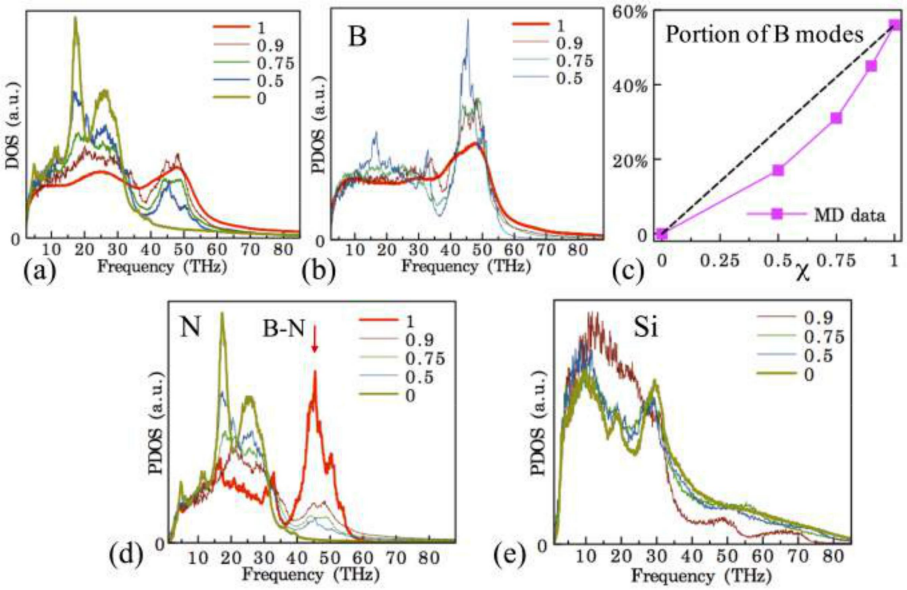

Figure 5: (a) Normalized phonon density of states of a-Si-B-N structures identified in the legend by their χ values (b) Partial phonon density of states of B and (c) portion of B modes with respect to all the phonon modes as a function of the dashed line connecting the values of the end phases is shown for a comparison. Partial phonon density of states of (d) N and (e) Si. In (d) the down arrow points to the B-N stretching model.

The analysis of the MD velocity data for the same set of model structures indicated that the added BN bonds should be thermally active as they show distinct vibrational features in the phonon density of states (DOS) and partial phonon density of states (PDOS). Fig. 5(a) shows that the phonon modes of a-Si_3N_4 are mainly distributed below 35 THz, while the a-BN phonon modes have a broader frequency range (0 - 60 THz) with a distinct peak at

45 THz. With increasing this peak forms and its intensity increases. The PDOS data shown in Figs. 5(b) further reveals that this peak originates in the vibrations of B atoms.

We have compared the area under the un-normalized DOS and PDOS spectra to obtain the proportion of phonon modes in the structure due to the vibrations of different atom types. As shown in Fig. 5(c), we find that the portion of B modes increases monotonically with the BN fraction. Recalling that B forms bonds only with N atoms, it follows that this bond proportion effect concerns the B-N bonds. This interpretation is in agreement with the data presented in Fig. 5(d) and (e), where the 45 THz peak can be identified only in the PDOS of N atoms. Note that a previous MD study,5 also reported the vibrational frequency of B-N stretching mode to be at 45 THz.

4. Properties of a-Si-B-N networks

Having probed the suitability of the Tersoff treatment for simulating a-Si-B-N films via comparison with our DFT and the available experimental and MD data, we now turn our attention to utilizing this description for predicting how the atomistic structure and composition influences thermal and mechanical properties.

4. 1. Thermal conductivity

In our calculations for we have considered only the collection of representative network structures with low enthalpies summarized in Fig. 3. This is because even with the efficient Tersoff Hamiltonian, the evaluation of eq. (3) is still a difficult task. For example, because $j_\alpha(\tau)j_\beta(0)$ exhibits non-ergodic long-time oscillations, averaging over multiple MD runs is required.31 Here, each reported value for a given model represents the average thermal conductivity measured from twenty MD measurement runs, each lasting 100 ps. The error bars represent the standard error based on twenty individual measurements.

We first considered one nearly-homogeneous network model for each and performed MD simulations at room temperature. Supercells with different side lengths were studied by

periodically repeating the optimized cell obtained from aiMD. Fig. 6(a) shows an example of the averaged integral of heat flux autocorrelation function for a-Si_3BN_5 with ~4 nm side length. There is good convergence after τ = 5 ps.

As demonstrated in Fig. 6(b), the accounting for the finite-size effects is important for predicting κ. The simulation cell size dictates the maximum phonon wavelength present in the simulation. For all χ, κ increases with the supercell size as additional long-wavelength phonons become available for heat transport. The crossover behavior observed at ~3 nm suggests that the long wavelength phonons bring a more significant contribution to κ for a-$Si_3B_9N_{13}$ than for a-$Si_3B_9N_{13}$. When κ converges, at side lengths larger than 4 nm, the κ of a-Si_3BN_5, a-$Si_3B_3N_7$, and a-$Si_3B_9N_{13}$ are calculated as 2.3 $\pm$ 0.1 W/mK, 3.0 $\pm$ 0.1 W/mK, and 3.1$\pm$ 0.5 W/mK, respectively. (Each κvalue reported here is the average value of κ_{xx}, κ_{yy} and κ_{zz}).

Fig. 6(c) suggests that the BN addition to a-Si3N4 leads to a monotonic increase in . The increase is weak such that a linear interpolation between the values of the binary compounds overestimates the MD computed κ. This observed trend may be a signature of the fact that h-BN has a larger longitudinal speed of sound than β-Si_3N_4, i.e., 16 km/s [32] vs. 9.9 km/s. [33]

Although a reduction of these values is expected in the amorphous phases, the speed of sound will still depend on the local order and nature of the bonds. [34] [To clarify the connection between κ and the speed of sound, recall that the kinetic theory defines as $(1/3)C_v v_g \Lambda$,where C_v and Λ denote the specific heat and phonon mean-free path, respectively. The phonon group velocity v_g for the heat-conducting long wavelength phonons is approximately the speed of sound. The above relation predicts the minimum thermal conductivity of a material at high temperatures, in which case C_v is close to a -independent constant and approaches the inter-atomic spacing limit. [35,36]

Our further investigations focused on the network-model dependence of κ. Fig. 7 shows that the computed κ values for our collection of nearly-homogeneous models (models 1-3 for each χ) are all contained in the 2.0–3.5 W/mK range. Overall, this plot shows that while κ has a weak

dependence on the network model representation, the variation of κ from different models

is larger than or on the same order like the standard error resulted from the computation by the Green-Kubo method. Thus, to gain an ensemble representation, further averaging of the individual values for the models with the same χ was performed. The obtained values, listed in the first line of Table 3, maintain the already noted trend of a weak increase of κ with χ.

In contrast with the nearly-homogeneous models, the h-BN segregation in $\chi = 0.9$ models has a significant impact on thermal transport. In Fig. 7, it can be seen that the individual values for models 4-6 are above the values obtained for models 1-3. This increase is associated with a significant increase in the anisotropy, which can be seen in Fig. 7. Model 4 provides a good example for observing the anisotropy since the h-BN layers are oriented along x. On one hand, in the y and z directions we obtained κ_{yy}=5.9 $\pm$ 0.3 W/mK and κ_{zz}=5.8 0.4 W/mK. These values are significantly larger than the of a-BN due to the crystallinity of the formed h-BN layers. On the other hand, in the x direction we obtained κ_{xx}=1.0$\pm$0.1 W/mK, a value that falls well below κ_{yy} anf κ_{zz}, and that is comparable with the thermal conductivity across layers in h-BN. [37] For a comparison, the diagonal elements calculated for model 1 with χ = 0:9 are κ_{xx}= 3.6$\pm$0.3 W/mK, κ_{yy} =2.7$\pm$0.3 W/mK, and κ_{zz} =3.0$\pm$0.2 W/mK.

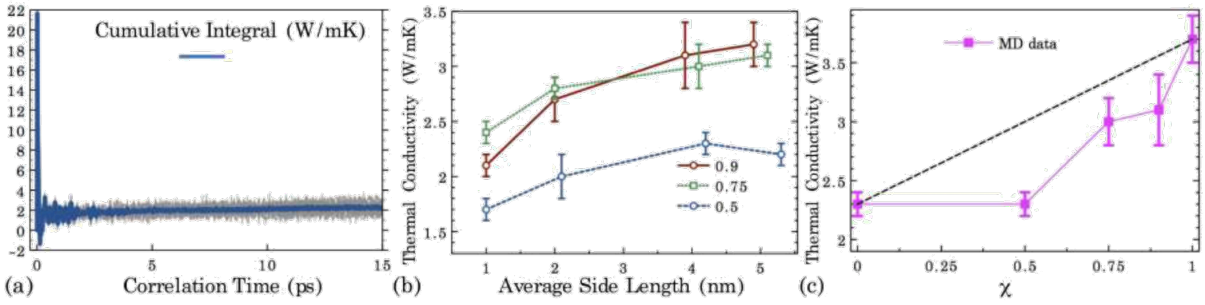

Figure 6: (a) Cumulative integral (blue) of the heat flux autocorrelation function averaged over twenty ensembles (gray) for ~ 4 nm-sized a-Si_3BN_5 (= 0:5); (b) Dependence of on the supercell size; (c) Dependence of on χ. The dashed line connecting the values of the end phases is shown for a comparison. The continuous line connecting the data point is to guide the eye. T ≈ 300 K.

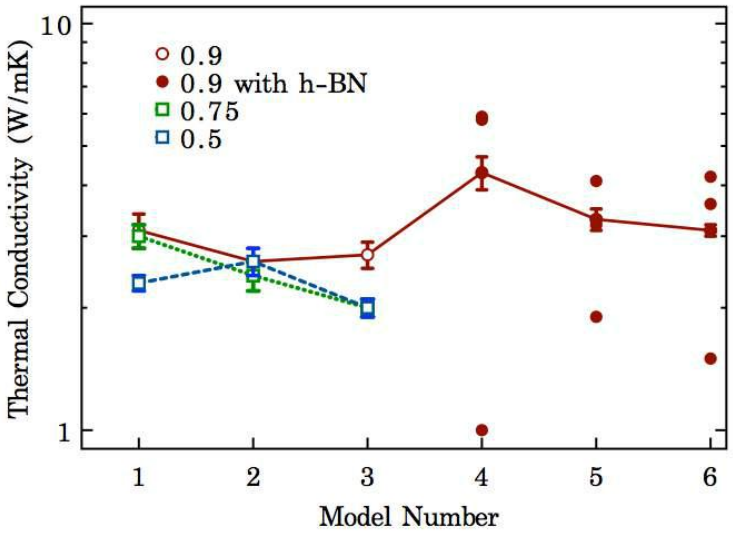

Figure 7: Structure dependence of the thermal conductivity a-Si_3BN_5 (χ = 0.5), a-$Si_3B_3N_7$ (χ = 0.75), and a-Si_3B9N_{13} (χ = 0.9). The horizontal axis refers to the network model number. Lines connect points with same χ. For models 4-6 with χ = 0.9 we have also plotted the values of the diagonal elements of the thermal conductivity matrix.

4. 2. Elasticity

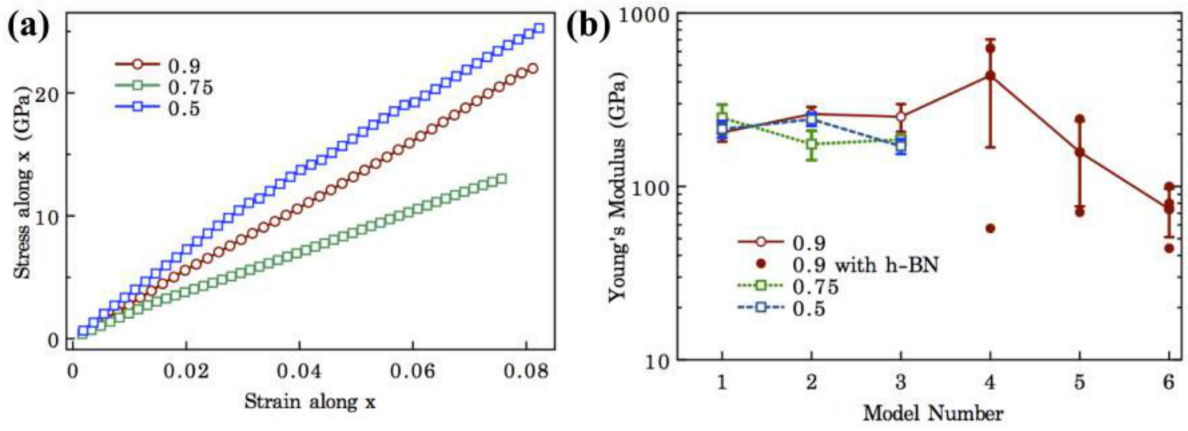

Figure 8: (a) Selected stress-strain curves, and (b) structure dependence of the Young's moduli of a-Si_3BN_5 (χ = 0:5), a-$Si_3B_3N_7$ (χ = 0:75), and a-$Si_3B_9N_{13}$ (χ = 0:9). In (b) the horizontal axis refers to the network model number. Lines connect data points with same χ. For models 4-6 with χ = 0:9 we have also plotted the values of the diagonal elements of the matrix.

We have screened the elastic properties for the same collection of structures. Fig. 8(a) presents the computed stress-strain curves for selected nearly-homogeneous networks with different χ. While different slopes are associated with the different structures, we see that the network elasticity is not increasing monotonically with the concentration of the added stiff B-N bonds. This is likely a signature of the specific structural environment seen by the atoms, a situation causing non-affinity in deformation. As it can be noted from Fig. 8(b), the model-specific Y values fluctuate in the 170–270 GPa interval. The elastic behavior of models 1-3 is isotropic. This transpires from the error bars, which represent the standard error based on the measurements performed in the three Cartesian directions. For a more realistic representation of Y as a function of χ, we have performed averaging of the values given by the different models. The Y values, listed in the second line of Table 3, suggest a weak increase of Y with χ. We also note that the obtained Young modulus for a-$Si_3B_3N_7$ is in very good agreement with the ab initio prediction (~ 200 GPa) given in Ref. [26].

In Fig. 8(b), it can be seen that the h-BN segregation in the χ =0.9 model has a strong effect on Y . For models 4-6, it can be seen that the diagonal components of Y present very different values.

For example, for model 4 in the y and z directions we obtained Y_{yy}=623 GPa and Y_{zz}=628 GPa. Such large large values can be expected along the h-BN layers. On the other hand, in the x direction we obtained Y_{xx}=57 GPa, a value that falls significantly below the Y values computed for the nearly-homogeneous networks. Moreover, we observed that this structure exhibits failure at elongation strains of only 3%, when the covalent bonds connecting the layers break.

Table 3: Model-averaged thermal conductivity and Young's modulus as a function of χ^a. For each models 1-3 have been considered in the averaging.

	$\chi = 0.50$	$\chi = 0.75$	$\chi = 0.90$
κ (W/mK)	2.3 ± 0.2	2.5 ± 0.4	2.8 ± 0.2
Y (GPa)	209 ± 30	203 ± 32	239 ± 25

[a]For each value of χ, models 1–3 have been considered in the averaging.

Conclusions

In summary, a-Si-B-N ceramics with different BN content a-Si_3BN_5, a-$Si_3B_3N_7$, and a-$Si_3B_9N_{13}$ were modeled as chemically-ordered random covalent networks with a computational protocol that involved aiMD simulations. The a-Si-B-N networks obtained this way exhibit very few or no under-coordinated atoms and a weak variation in thermochemical stability. Further, atomistic simulations based on Tersoff potentials were performed to evaluate and the Young's moduli of the network models obtained by the aiMD simulations. For each composition it was necessary to average and Y over different network models. The main finding of this investigation is that thermal and mechanical properties depend weakly on the BN content, as long as the network structure lacks segregation into h-BN layers.

Understanding the relationship between composition and the thermal and mechanical properties is of great importance for developing a-Si-B-N coatings able to provide protection against thermal impact and mechanical loads. The principal conclusion of the presented investigation is that it unworthy to pursue compositions as high as $\chi = 0.9$ (a-$Si_3B_9N_{13}$). This is because large promotes BN layer segregation, an effect that severely weakens the structure in the

cross-layer direction and increases thermal conductivity along the layer direction. Instead, our study identifies $\chi = 0.5$ (a-Si_3BN_5) and $\chi = 0.75$ (a-$Si_3B_3N_7$) as the compositions least prone to segregation into h-BN layers. These compositions exhibit a combination of low thermal conductivity and large mechanical stiffness suitable for coating applications. The methods of investigation used here show promise for studying the composition–structure–properties relationship in more complex quaternary amorphous ceramics. [8] [38–40] Further, the results can be applied in multi-scale simulation frameworks [41, 42] to enable system-scale predictions for the mechanical behavior.

Acknowledgement

Work was supported by the collaborative DMREF NSF 1333158 and 1335502 grants. Computations were performed at the Minnesota Supercomputing Institute.

Notes and References

1. Savino, R.; De Stefano Fumo, M.; Paterna, D.; Serpico, M. Aerothermodynamic Study of UHTC-Based Thermal Protection Systems. Aerosp. Sci. Technol. 2005, 9, 151–160.
2. Paul, A.; Binner, J.; Vaidhyanathan, B. UHTC Composites for Hypersonic Applica-tions. In Ultra-High Temperature Ceramics; Fahrenholtz, W. G., Wuchina, E. J., Lee, W. E., Zhou, Y., Eds.; John Wiley & Sons, Inc., Hoboken, New Jersey, 2014; pp 144–166.
3. Corral, E. L.; Walker, L. S. Improved Ablation Resistance of C-C Composites Using Zirconium Diboride and Boron Carbide. J. Eur. Ceram. Soc. 2010, 30, 2357–2364.
4. Tului, M.; Lionetti, S.; Pulci, G.; Rocca, E.; Valente, T.; Marino, G. Effects of Heat Treatments on Oxidation Resistance and Mechanical Properties of Ultra High Temperature Ceramic Coatings. Surf. Coat. Technol. 2008, 202, 4394–4398.

5. Jansen, M.; Schön, J. C.; van Wüllen, L. The Route to the Structure Determination of Amorphous Solids: A Case Study of the Ceramic $Si_3B_3N_7$. Angew. Chem. Int. Ed. 2006, 45, 4244–4263.
6. Hannemann, A.; Schön, J. C.; Jansen, M. Modeling the Sol-Gel Synthesis Route of Amorphous $Si_3B_3N_7$. J. Mater. Chem. 2005, 15, 1167–1178.
7. Hannemann, A.; Schön, J.; Jansen, M.; Sibani, P. Nonequilibrium Dynamics in Amorphous $Si_3B_3N_7$. J. Phys. Chem. B 2005, 109, 11770–11776.
8. He, J.; Zhang, M.; Jiang, J.C.; Vlček, J.; Zeman, P.; Steidl, P.; Meletis, E.I. Microstructure Characterization of High-Temperature, Oxidation-Resistant Si-B-C-N Films. Thin Solid Films 2013, 542, 167–173.
9. Tang, Y.; Wang, J.; Li, X.; Xie, Z.; Wang, H.; Li, W.; Wang, X. Polymer-Derived SiBN
10. Fiber for High-Temperature Structural/Functional Applications. Chem. Eur. J 2010, 16, 6458–6462.
11. Schön, J.; Hannemann, A.; Sethi, G.; Pentin, V.; Jansen, M. Modelling Structure and Properties of Amorphous Silicon Boron Nitride Ceramics. Process. Appl. Ceram. 2011, 5, 49–61.
12. Lawson, J.W.; Daw. M.S.; Bauschlicher. C.W. Lattice Thermal Conductivity of Ultra High Temperature Ceramics ZrB_2 and HfB_2 From Atomistic Simulations. J. Appl. Phys. 2011, 110, 083507.
13. Kindlund, H.; Sangiovanni, D.; Martinez-de-Olcoz, L.; Lu, J.; Jensen, J.; Birch, J.; Petrov, I.; Greene, J.; Chiritˇa, V.; Hultman, L. Toughness Enhancement in Hard Ceramic Thin Films by Alloy Design. APL Mater. 2013, 1, 042104.
14. Tang, B.; An, Q.; Goddard III, W. A. Improved Ductility of Boron Carbide by Microalloying with Boron Suboxide. J. Phys. Chem. C 2015, 119, 24649–24656.
15. Zhang, K.; Balasubramanian, K.; Ozsdolay, B. D.; Mulligan, C. P.; Khare, S. V.;

16. Zheng, W. T.; Gall, D. Epitaxial NbC_xN_{1-x}(001) Layers: Growth, Mechanical Proper-ties, and Electrical Resistivity. Surf. Coat. Technol. 2015, 277, 136–143.
17. Ni, Y.; Jiang, J.; Meletis, E.; Dumitricˇa, T. Thermal Transport Across Few-Layer Boron Nitride Encased by Silica. Appl. Phys. Lett. 2015, 107, 031603.
18. Griebel, M.; Hamaekers, J. Molecular Dynamics Simulations of Boron-Nitride Nan-otubes Embedded in Amorphous Si-B-N. Comp. Mater. Sci. 2007, 39, 502–517.
19. Ge, K. K.; Ye, L.; Han, W. J.; Han, Y.; Zhao, T. Pyrolysis of Polyborosilazane and Its Conversion into SiBN Ceramic. Adv. Appl. Ceram. 2014, 113, 367–371.
20. Kroll, P. Modelling Polymer-Derived Ceramics. J. Eur. Ceram. Soc. 2005, 25, 163–174.
21. Kresse, G.; Hafner, J. Ab initio Molecular Dynamics for Liquid Metals. Phys. Rev. B 1993, 47, 558–561.
22. Kresse, G.; Hafner, J. Ab initio Molecular-Dynamics Simulation of the Liquid-Metal-Amorphous-Semiconductor Transition in Germanium. Phys. Rev. B 1994, 49, 14251–14269.
23. Kresse, G.; Furthmüller, J. Efficiency of Ab-Initio Total Energy Calculations for Metals and Semiconductors using a Plane-Wave Basis Set. Comp. Mater. Sci. 1996, 6, 15–50.
24. Blöchl, P. E. Projector Augmented-Wave Method. Phys. Rev. B 1994, 50, 17953–17979.
25. Kresse, G.; Joubert, D. From Ultrasoft Pseudopotentials to the Projector Augmented-Wave Method. Phys. Rev. B 1999, 59, 1758–1775.
26. Plimpton, S. Fast Parallel Algorithms for Short-Range Molecular-Dynamics. J. Comput. Phys. 1995, 117, 1–19.
27. Matsunaga, K.; Iwamoto, Y. Molecular Dynamics Study of Atomic Structure and Dif-fusion Behavior in Amorphous Silicon Nitride Containing Boron. J. Am. Ceram. Soc. 2001, 84, 2213–2219.
28. Kroll, P.; Hoffmann, R. Silicon Boron Nitrides: Hypothetical Polymorphs of $Si_3B_3N_7$.
29. Angew. Chem. Int. Ed. 1998, 37, 2527–2530.

30. Dumitricˇa, T.; Yakobson, B. I. Rate Theory of Yield in Boron Nitride Nanotubes. Phys. Rev. B 2005, 72, 035418.
31. Kubo, R. The Fluctuation-Dissipation Theorem. Rep. Prog. Phys. 1966, 29, 255-284 .
32. The stopping tolerance for energy is 1.0 e-8 eV and that for force is 1.0 e-8 eV/Angstrom.
33. Jalowiecki, A.; Bill, J.; Aldinger, F.; Mayer, J. Interface Characterization of Nanosized B-doped Si3N4/SiC Ceramics. Compos. Part A-Appl. S. 1996, 27, 717–721.
34. Esfarjani, K.; Chen, G.; Stokes, H. T. Clarke, D. R. Heat Transport in Silicon From First-Principles Calculations. Phys. Rev. B 2011, 84, 085204.
35. Thermodynamic Properties of Solids: Experiments and Modeling; Chaplot, S.; Mit-tal, R.; Choudhury, N., Eds.; Wiley, Weinheim, Germany, 2010; pp 1-322.
36. Capilla, J.; Olivares, J.; Clement, M.; Sangrador, J.; Iborra, E.; Devos, A. In Characterization of Amorphous Tantalum Oxide for Insulating Acoustic Mirrors. Proceedings of the 2011 IEEE International Frequency Control and the European Frequency and Time Forum Joint Conference, pp 1-6, 2011.
37. Testardi, L.; Hauser, J. Sound Velocity in Amorphous Ge and Si. Solid State Commun. 1977, 21, 1039–1041.
38. Clarke, D. R. Materials Selection Guidelines for Low Thermal Conductivity Thermal Barrier Coatings. Surf. Coat. Technol. 2003, 163, 67–74.
39. Cahill, D. G.; Watson, S. K.; Pohl, R. O. Lower Limit to the Thermal Conductivity of Disordered Crystals. Phys. Rev. B 1992, 46, 6131.
40. Simpson, A.; Stuckes, A. D. The Thermal Conductivity of Highly Oriented Pyrolytic Boron Nitride. J. Phys. C: Solid St. Phys. 1971, 4, 1710-1718.
41. Jäschke, T; Jansen, M. Synthesis and Characterization of New Amorphous Si/B/N/C Ceramics with Increased Carbon Content Through Single-Source Precursors. C. R. Chimie. 2004, 7, 471-482.

42. Zhang, M; Jiang, J.; Houska, J.; Kohout, J.; Vlcek, J.; Meletis, E.I. A Study of the Microstructure Evolution of Hard Zr-B-C-N Films by High-Resolution Transmission Electron Microscopy. Acta Mater. 2014, 77, 212-222.
43. Zhang, M; Jiang, J.C.; Mares, P.; Houska, J.; Vlcek, J.; Meletis, E.I. Effect of the Si Content on the Microstructure of Hard, Multifunctional Hf-B-Si-C Films Prepared by Pulsed Magnetron Sputtering. Appl. Surf. Sci. 2015, 357, 1343-1354.
44. Kalweit, M; Drikakis, D. Multiscale Methods for Micro/Nano Flows and Materials. J. Comput. Theor. Nano. 2008, 5, 1923-1938.
45. Asproulis, N; Kalweit, M; Drikakis, D. A. Hybrid Molecular Continuum Method Using Point Coupling. Adv. Eng. Softw. 2012, 46, 85-92.

Appendix 4:

Introduction:

The previous section includes the published manuscript for the computation of thermal conductivity in a-SiBN models. However, the publication lacks some key points:

- Amorphous SiBN material is targeted towards high temperature applications. However, the paper only discussed thermal conductivity at 300 K.
- The previous publication mostly considers one model for a particular composition of a-SiBN. Therefore computations are mostly dependent on the model chosen (even if that is the lowest energy model). An average over many "low-energy" models will, statistically be closer to the true value.
- The thermal conductivity of a-BN cannot be compared to a-SiBN models as the model has been generated using different means.

In this appendix, I address the aforementioned deficiencies through my individual computations. The Tersoff potential parameters for Si, B, and N are in agreement with published work. [1]

A4.1) Thermal conductivity using Green-Kubo Method:

Each model of a-SiBN optimized within DFT is subjected to the empirical Tersoff Potential in LAMMPS. [2] Energies of these models are then computed by adjusting atom coordinates, keeping the box volume intact. Each structure is equilibrated – first 200 ps in NPT ensemble, next 100 ps in NVT ensemble and then in NVE for another 100 ps. Then the flux is generated under NVE ensemble for 100 ps. The flux-flux auto-correlation is computed using a MATLAB code as a part of the post-processing work. All results are averaged over 20 independent simulations with different initial conditions. For finite-size effects, the box is expanded 4 times in x, y and z directions with box length ~ 4 nm and 6400 – 7168 atoms. In addition, for each composition, I include three independednt models and average the results.

Thermal conductivity (κ) is related to the ensemble average of the flux-flux auto-correlation according to the following equation: [3]

$$\kappa = \frac{1}{Vk_B T^2} \int_0^\infty \langle J(t) \otimes J(0) \rangle dt$$

This infinite integral in the above equation is replaced by summation according to Schelling's approach. [4]

$$\kappa = \frac{\Delta t}{Vk_B T^2} \sum_{m=1}^{M} \frac{1}{(N-m)} \sum_{n=1}^{N-m} J(m+n)J(n)$$

where $\Delta t = 0.15$ fs; N = total length of the simulations, 100 ps; M is the correlation length depending on the convergence criterion; T = Temperature in K and k_B is the Boltzmann constant. For all computations, κ is averaged over 20 independent runs (different initial velocities for atoms) and flux-flux auto-correlation time (τ) is chosen to be 10 ps.

The thermal conductivity is a second rank tensor with 9 matrix elements. The thermal conductivity matrix for an isotropic model comprises of three independent values only, since $\kappa_{11} = \kappa_{22} = \kappa_{33}$, and all remaining elements vanish. The value of thermal conductivity reported is an average of the diagonal elements or the trace, κ_{trace}.

Example of thermal conductivity matrix for a-Si_3N_4 is as follows:

T = 302.9 ± 0.4 K

$$\kappa = \begin{bmatrix} 2.2 \pm 0.3 & 0.1 \pm 0.2 & -0.3 \pm 0.4 \\ -0.1 \pm 0.4 & 2.3 \pm 0.3 & -0.1 \pm 0.4 \\ -0.4 \pm 0.3 & -1.2 \pm 0.3 & 2.4 \pm 0.3 \end{bmatrix}$$

Trace = 2.3 ± 0.2 $Wm^{-1}K^{-1}$

In Figure A4.1, I plot the integrated heat current auto-correlation function (HCACF) recorded for 20 individual MD runs for 4x4x4 super cell of a-Si_3N_4 at 300 K. The flux-flux auto-correlation time (τ) is 16.7 ps. Ideally the HCACF is expected to converge to zero over time. However, it is obvious from Fig. A4.1 that depending on individual runs, or the chosen length of auto-correlation time, thermal conductivity of the sytem varies. For instance, κ_{trace} varies between 7.1 $Wm^{-1}K^{-1}$ and 0.5 $Wm^{-1}K^{-1}$ for τ = 16.7 ps between 20 runs. For a particular run: at τ = 5, κ_{trace} =

4.1 $Wm^{-1}K^{-1}$; at τ = 10 ps, κ_{trace} = 0.5 $Wm^{-1}K^{-1}$; while at at τ = 15 ps, κ_{trace} = 2.0 $Wm^{-1}K^{-1}$. Nevertheless, over 20 runs, at τ = 5, 10 and 15 ps is fairly convergent – with the average κ_{trace} = 2.6, 2.3 and 3.1 $Wm^{-1}K^{-1}$ respectively. Therefore the choice of 20 runs to achieve an average value and τ = 10 ps is justified.

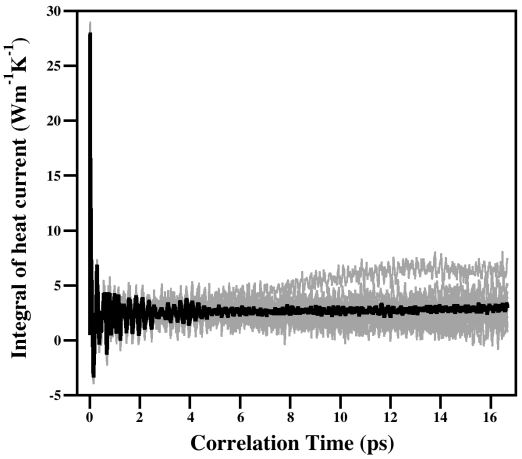

Figure A4.1: Integral of Heat current auto-correlation function (HCACF) for 4x4x4 super cell of a-Si_3BN_4 at 300K using Tersoff potential for 20 independent runs (in grey). The black line represents the average of these 20 runs.

For a-SiBN models we study thermal conductivity, firstly as a function of temperature of the system and secondly as a function of BN content at 300 K. Results are discussed as below:

A4.2) Function of Temperature:

The temperature dependence of the thermal conductivity, precisely κ_{trace}, between 300 and 2100 K is plotted in figure 2. At 300 K, the thermal conductivity is significantly different for different mol% of BN. As the temperature increases from 300 – 2100 K, κ of a-SiBN models exhibit overlapping values within limits of standard error. Moreover at 2100 K, we see a convergence of κ_{trace} at ~ 2.0 $Wm^{-1}K^{-1}$ for all compositions.

However, for the model of layered-$Si_3B_9N_{13}$ κ = 3.4 ± 0.6 $Wm^{-1}K^{-1}$ at 300 K. With increase in temperature, κ for this composition decreases and reaches a minimum at 1200 K. Beyond 1220 K, it again increases and converges to 3.3 ± 1.1 $Wm^{-1}K^{-1}$ at 2100 K. In addition, if standard error

for each composition is taken into account, the thermal conductivity is rather constant over the temperature range. Thus, within the Tersoff potential trends in thermal conductivity of a-SiBN models with temperature is inconclusive.

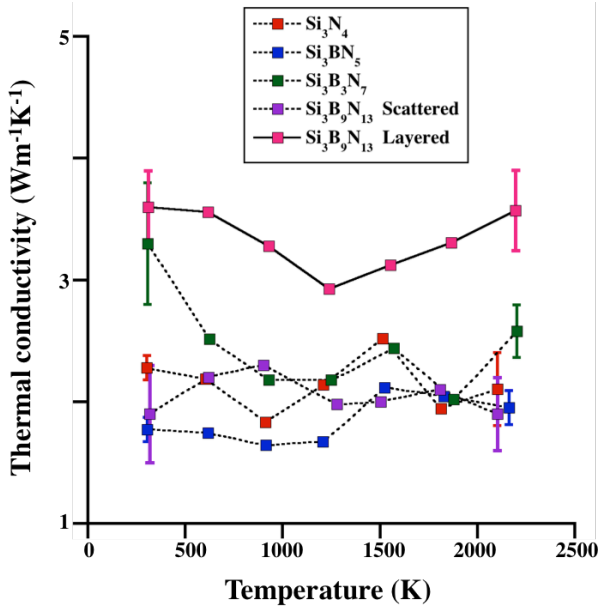

Figure A4.2: Trends in thermal conductivity with temperature for a-SiBN models. Thermal conductivity is distinct for different compositions at 300 K but soon converge to ~ 2 $Wm^{-1}K^{-1}$ at higher temperatures.

A4.3) Function of mol % BN at 300 K:

Figure A4.3 plots the thermal conductivity of our material as a function of the mol % BN present in our models. Adding BN to Si_3N_4 results in an initial drop of κ (for a-Si_3BN_5) and then increases with as mol % BN = 75 and 90 for a-$Si_3B_3N_7$ and a-$Si_3B_9N_{13}$ The structure of a-Si_3BN_5 has small isolated units of BN that act as scattering centers and reduce the phonon mean free path (kinetic theory). This leads to a decrease in thermal conductivity. Even for models with 90 % BN, a-$Si_3B_9N_{13}$ with scattered BN units, has low κ comparable to a-Si_3BN_5. Alternatively, a-$Si_3B_3N_7$ and "layered" a-$Si_3B_9N_{13}$ has long channels of BN units that facilitate the flow of heat, resulting in higher thermal conductivity of the material. The model for a-BN is not included in this discussion as it has been generated from a different approach.

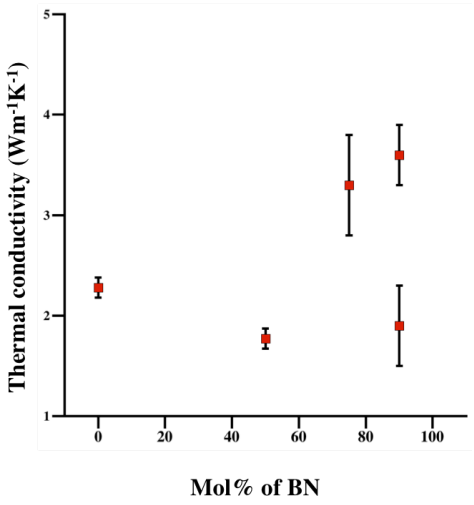

Figure A3.3: Composition dependence of thermal conductivity. The thermal conductivity increases with increasing mol % BN in the material. All computations are done with box lengths of ~ 40 Å and at 300 K.

Conclusions:

The main conclusions from this work are:

- The Tersoff potential provides indecisive trends for temperature and composition effects of thermal condctivity for a-SiBN models.
- Depending on the length of flux-flux auto-correlation, thermal conductivity of the material can vary widely.

Thus the Tersoff potential is not a wise choice of potential to study thermal conductivity of amorphous SiBN material. The next chapter describes my efforts to use a different potential tostudy thermal conductivity of a-SiBN material.

References:

[1] K. Matsunaga, Y. Iwamoto, Molecular dynamics study of atomic structure and diffusion behavior in amorphous silicon nitride containing boron, J Am Ceram Soc 84(10) (2001) 2213-2219.

[2] S. Plimpton, Fast Parallel Algorithms for Short-Range Molecular-Dynamics, J Comput Phys 117(1) (1995) 1-19.

[3] R. Kubo, The fluctuation-dissipation theorem, Reports on Progress in Physics 29(1) (1966) 255.

[4] P.K. Schelling, S.R. Phillpot, P. Keblinski, Comparison of atomic-level simulation methods for computing thermal conductivity, Phys Rev B 65(14) (2002).

Summary:

Amorphous silicon boron nitride (a-SiBN) materials are studied for their potential application as a non-oxide high performance coating material. While the earliest studies on this material date back to 1993, interest in this material is still widespread. [1] In this collaborative project, an effort is made to predict the thermal conductivity and Young's modulus of a-SiBN. The empirical potential of choice is the Tersoff potential. While the parameters for Si are a part of Tersoff's initial proposition, B and N parameters are respectively from Matsunaga and Kroll. Small models are built using the network algorithm approach with increasing mol % of BN in Si_3N_4. The results of the study are straightforward - thermal conductivity and Young's modulus only depend marginally on the BN content of the material. Unless the BN exists in the form of long extended layers as in the crystal structure of hexagonal BN, thermal conductivity of these potential coating materials is low.

However, in an individual effort, I study how well the Tersoff potential performs when applied to the SiBN system. The first concern is coordination defects. Amorphous SiBN models generated for are first optimized within DFT. Afterwards, models are subjected to the Tersoff potential. Care is taken to ensure that the local geometry is not significantly altered when applying the Tersoff potential.

However for computing the thermal conductivity the heat-current auto-correlation curve is not *smooth* and does not decay to zero for long time scales. As a result, the value of thermal conductivity strongly depends on the correlation time. Moreover, the method proves computationally expensive as well, because of the tedious averages required to cancel out fluctuations in the κ value.

Reference:

[1] H.P. Baldus, M. Jansen, O. Wagner, - 89-91 (1993) - 80.

CHAPTER 5

THERMAL CONDUCTIVITY OF AMORPHOUS SILICON BORON NITRIDE: STUDYING IMPACT OF COMPOSITION, DENSITY, AND TEMPERATURE USING DENSITY FUNCTIONAL THEORY CALCULATIONS AND EMPIRICAL POTENTIAL MOLECULAR DYNAMIC SIMULATION[5]

[5] This work is submitted to Journal of American Ceramic Society and is currently under revision.

Scope and Motivation

In this chapter we continue the investigation of thermal conductivity for amorphous silicon boron nitride (a-SiBN) ceramics. As discussed before, these materials find use as applications as oxidation resistant protective coatings and as ceramic fibers. Experimentally bulk synthesis for a-SiBN involves polymeric intermediates, with TADB (tri-chlorosilylaminochloroborane) being most extensively used. Thin films of this material are derived from deposition techniques.

The motivation for this work is consequent from the conclusions of chapters 3 and 4. Chapter 3 establishes that the Marian-Gastreich 2 body (MG2) potential is suited to study systems consisting of Si and N. In the chapter 4 appendix, I establish that the deficiencies the Tersoff potential has modeling SiN systems is also applicable to Si-B-N systems. Models have coordination defects and high enthalpies of formation, indicating unrealistic structures. The Tersoff potential predicts ambiguous trends while studying temperature dependency of κ in these materials. The structure library of a-SiBN was expanded with realistic large-scale models and hypothetical crystalline models of SiBN for comparison. The effects of temperature, density and composition on the thermal conductivity of the material are systematically investigated.

The chapter next includes the submitted manuscript for this project and some additional information in the Appendix.

Thermal Conductivity of Amorphous Silicon Boron Nitride: Studying Impact of Composition, Density, and Temperature using Density Functional Theory Calculations and Empirical Potential Molecular Dynamic Simulations

Atreyi Dasmahapatra[1] and Peter Kroll[1*]

[1] Department of Chemistry and Biochemistry, The University of Texas at Arlington, 700 Planetarium Place, Arlington, Texas 76019, United States.

Abstract

We study thermal conductivity (κ) of amorphous silicon boron nitride (a-SiBN) for different compositions and densities as a function of temperature using density functional theory (DFT) calculations and equilibrium molecular dynamic (MD) simulations. Our library of amorphous structures consists of network models comprising 100 – 200 atoms and large-scale models with up to 57000 atoms generated using the empirical Marian-Gastreich two-body (MG2) potential. Crystalline structures within the Si_3N_4-BN system are considered as well. We use two distinct approaches to compute thermal conductivity of a-SiBN. To estimate κ in the high temperature limit we feed Clarke's phenomenological model with elasticity data obtained by DFT calculations. We further perform equilibrium MD simulations and apply the Green Kubo method. This approach shows decrease of κ with increasing temperature and provides results at high temperatures that agree with results derived within Clarke's model. We find that κ of a-SiBN depends on composition and increases as the BN content in the structure increases. The effect is pronounced at low temperature but almost vanishes at high temperature. Furthermore, thermal conductivity depends on density and porosity, with a linear relation between κ and density.

Introduction

Amorphous silicon boron nitride (a-SiBN) materials are high performance non-oxide refractory ceramics with a degradation temperature of 1800 °C and oxidation resistance up to 1600 °C. [1, 2, 3] Potential applications of a-SiBN include ceramic parts and fibers as well as protective coatings. [4] Recently, Eu^{2+} and Ce^{3+} doped amorphous $Si_3B_3N_7$ ceramics have been proposed as luminescent materials in white LEDs. [5] Synthesis of SiBN ceramic fibers follow the polymer-to-ceramic route. [1, 2, 6] Protective SiBN thin films have been synthesized by plasma enhanced chemical vapor deposition techniques. [7]

Several experimental and computational studies addressed structure and mechanical properties of a-SiBN. [8, 9, 10, 11] Thermal conductivity data, on the other hand, is sparse and usually refers to a material that includes additional carbon, hence SiBNC. Values of 1.1 ± 0.1 $Wm^{-1}K^{-1}$ at 300 K, 3 $Wm^{-1}K^{-1}$ at 1473 K and 0.40 $Wm^{-1}K^{-1}$ at 1773 K were reported for some amorphous SiBNC ceramic fibers ("Siboramic"). [1, 2, 12] In a more systematic study, Göbel et al. reported values of 0.490 $Wm^{-1}K^{-1}$ and 0.76 $Wm^{-1}K^{-1}$ at 300 K and 773 K, respectively. [13] Kousaalya et al. investigated thermal properties of amorphous SiBNC foams at high temperatures. They reported an increase of thermal conductivity from 0.4 to 1.8 $Wm^{-1}K^{-1}$ upon increasing temperature from 300 to 1200 °C. [14] Previous computational studies addressed $Si_3B_3N_7$. Schön and Hannemann performed non-equilibrium MD simulations using the empirical MG2 potential and computed a thermal conductivity of 4 $Wm^{-1}K^{-1}$ between 300 – 500 K. [15, 16, 17] Recently, we reported equilibrium MD simulations of SiBN at 300 K using the Tersoff potential and highlighted the impact of BN content in SiBN on thermal conductivity. [18]

In the present study, we explore thermal conductivity of SiBN using both quantum chemical and empirical methods. First we investigate small a-SiBN models as described in Ref. [18] within DFT, and then expand the structure library with large-scale models (~50000 atoms) generated using the empirical Marian-Gastreich two-body (MG2) potential. [17] We also incorporate hypothetical crystalline models of $Si_3B_3N_7$ and Si_3BN_5. [19] For calculation of thermal conductivity

we employ the phenomenological model of Clarke and the Green Kubo method. [20, 21] We achieve an agreement between the two distinct methods and establish relations between thermal conductivity κ and temperature, density and composition of the material.

Computational Methods

Structure Generation

We generate models of amorphous SiBN with compositions Si_3N_4, Si_3BN_5, $Si_3B_3N_7$ and $Si_3B_9N_{13}$. In the quasi-binary system, Si_3N_4-BN, this corresponds to molar content of BN as 0, 50, 75, 90, and 100% respectively. We follow two different approaches for structure generation, referred to as Set 1 and Set 2. SiBN models of the first set are generated using a combination of network modeling and Density Functional Theory calculations, with details given in Ref 18. [22, 23, 24, 25] Augmenting this work, we included at least one model for each composition with twice as many atoms (up to 224 atoms). Models of Set 1 have densities between 2.7 - 3.0 $g \cdot cm^{-3}$.

Models of Set 2 have been generated via Molecular Dynamic (MD) simulations through a standard melt-and-quench (MQ) procedure. For MD simulations we apply the 2-body empirical Marian-Gastreich potential (MG2) (details further below), which we implemented in the LAMMPS code. [17 26] Taking advantage of the faster empirical simulation technique, we place 51200 to 57344 atoms randomly in a simulation box of length ~ 9 nm. The exact number of atoms and cell volume depend on composition and density of a model, respectively. First we heat the system within 20 ps to 5000 K (heating rate of $2.35 \cdot 10^{14}$ $K \cdot s^{-1}$) to obtain a "melt-like" state. At 5000 K we "hold" the system briefly for 5 ps. In this "melt-like" form of the structure, we monitor the diffusion of atoms as well as the coordinating neighbors to confirm that no memory of the original configuration is retained. The "quenching" procedure starts by cooling the system within 50 ps to 3000 K (quenching rate of $4.0 \cdot 10^{14}$ $K \cdot s^{-1}$), followed by a hold at 3000 K for 5 ps. Cooling continues to 2000 K in 50 ps ($2.0 \cdot 10^{14}$ $K \cdot s^{-1}$), and thereafter to 300 K in 500 ps ($3.4 \cdot 10^{12}$ $K \cdot s^{-1}$). The total simulation time for the melt-quench procedure is 630 ps. Our heating and

cooling rates are comparable to Hannemann et al.. [27] At all times during the simulations, we keep the volume constant and use a time step of 0.1 fs for the integration of the equations of motion. Structures obtained after melt-and-quench are subjected to final energy minimization in LAMMPS by optimizing atom positions. We choose two densities, 2.1 and 3.2 $g \cdot cm^{-3}$, for every composition of our models in Set 2. The only exception to this is a-$Si_3B_3N_7$ for which we generate models with densities ranging from 1.6 $g \cdot cm^{-3}$ to 3.2 $g \cdot cm^{-3}$, in steps of 0.2 $g \cdot cm^{-3}$. For all our models in Set 2, we generate three (3) models per density but choose the lowest energy model for further work.

Therefore, our structure library consists of small models (100 – 224 atoms) – referred to as "Set 1" and large-scale models (51200 – 57344 atoms) – belonging to "Set 2".

Furthermore, with β-Si_3N_4, h-BN and the mixed phases α-3-Si_3BN_5 and β-1-$Si_3B_3N_7$ we consider crystalline structures including hypothetical ternary SiBN phases. [19] Thus, our complete structure library consists of small network models of Set 1, large-scale models of Set 2 generated via melt-quench simulations, and crystalline SiBN models. For crystalline SiBN structures we compute DFT energies of β-Si_3N_4 and h-BN as -58.69 eV/f.u. and -17.89 eV/f.u., respectively. Enthalpies of formation (ΔH_f) for the mixed crystals are 0.085 eV/atom for α-3-Si_3BN_5 and 0.118 eV/atom for and β-1-$Si_3B_3N_7$. The latter value is in agreement with previous results. [19] Using the MG2 potential we obtain, 35.76 eV/f.u. and -11.57 eV/f.u. for β-Si_3N_4 and h-BN, respectively and ΔH_f of 2.03 eV/atom for α-3-Si_3BN_5, and 0.22 eV/atom for β-1-$Si_3B_3N_7$. [17]

Calculation of Thermal Conductivity, κ:

a. Applying Clarke's phenomenological model using DFT computed data

For all network models of Set 1 that are generated using the empirical/quantum-chemical approach we calculate elastic constants c_{ij} via the strain-stress relationship given by Hooke's Law. We determine bulk modulus (B), Young's modulus (E), and shear modulus (G) for each structure within the approximations of Voigt, Reuss and Hill. [28, 29, 30] Lattice thermal conductivity at high temperatures is estimated using Clarke's model: [20]

$$\kappa_{\min} = 0.87 k_B N_A^{2/3} \frac{m^{2/3} \rho^{1/6} E^{1/2}}{M^{2/3}}$$

where E is the Young's modulus, M is the total mass of the system, m is the number of atoms in the system, k_B the Boltzmann constant, and N_A Avogadro's number. Clarke's model is valid only in the high temperature limit, when heat capacity reduces to the Dulong-Petit value.

b. Applying the Green-Kubo method using equilibrium MD simulations

For SiBN network models of Set 1 we build 3x3x3 (for 200 - 224 atoms in the unit cell) and 4x4x4 (for 100 - 112 atoms in the unit cell) super-cells to achieve simulation boxes with cell parameters larger than 40 Å in each direction. We compute thermal conductivity (κ) of models via equilibrium MD simulations using the Green-Kubo method. [21] Thermal conductivity (κ) is given by the integral over the flux-flux auto-correlation function:

$$\kappa = \frac{1}{V k_B T^2} \int_0^\infty \langle J(t) J(0) \rangle$$

where J(0) is the initial heat flux at time t = 0 and J(t) is the heat flux at time t. V is the volume of the system, T is the temperature in Kelvin and k_B is the Boltzmann constant. To evaluate the integral we follow the approach by Schelling. [31] For models of Set 1, we perform MD simulations: first in an isobaric-isothermal ensemble (NPT) for 400 ps, followed by equilibration for 200 ps in canonical ensemble (NVT), and finally in a micro-canonical ensemble (NVE) for 200 ps. Time integration is performed with Nose-Hoover style non-Hamiltonian equations of motion that generate positions and velocities sampled from the NPT, NVT and NVE ensembles. Our time step for the integration of the equations of motion is 0.1 fs. After this equilibration, we stay in the NVE ensemble for another 100 ps and compute the heat flux **J**. This data is used to compute thermal conductivity (κ). The total time for each simulation, including equilibration and recording of heat flux, is 900 ps. The procedure agrees with Ref. [18] except for the different empirical potential. Applying the Green-Kubo method to compute thermal conductivity yields the full second-rank tensor κ via auto-correlation of heat flux, with matrix elements κ_{ij} ~

$J_i(t)J_j(0)$. For each model we calculate an average tensor κ_{ij} from five (5) independent simulations with different initial velocities for atoms. The error margin refers to the standard error of the data. In practice, we find that off-diagonal elements of κ are consistently smaller than the margin of error. For an isotropic system, the only independent quantity is the trace of κ. Anisotropy among the diagonal elements is present in crystalline phases and in "layered" structures of $Si_3B_9N_{13}$ (Set 1).

Models of Set 2 comprise of five to eight times more atoms than the supercells of Set 1. Hence, cell parameters are large enough (70 - 90 Å) to prevent finite size effects while computing thermal conductivity. Initially, we followed the same MD procedure as described above. However, in course of our study we noticed a much faster equilibration of the system when using the MG2 potential in comparison to using the Tersoff approach of Ref. [18]. Taking advantage of this, we use shorter simulation times: 20 ps in NPT, 20 ps in NVT and 20 ps in NVE to equilibrate the system. The heat flux is recorded for 90 ps within the NVE ensemble. The total simulation time is reduced to 150 ps, which is a significant cost saving for amorphous models. Crystalline models, on the other hand required significantly longer simulation times while recording the heat-flux under NVE conditions. For example, for β-Si_3N_4, the flux-flux auto-correlation at 300 K decays significantly slower compared to any amorphous system. For all crystalline models, simulations have been repeated ten (10) times and the data is averaged.

Marian-Gastreich empirical two-body potential (MG2) [17]

The Marian-Gastreich potential (MG2) is a two-body potential with Morse-type Si-N and B-N interactions; repulsive terms for N-N, B-B, B-Si and Si-Si interaction; and additional dispersion terms for N-N interactions. The latter stabilize the layered structures of crystalline hexagonal and rhombohedral BN. Details for the potential can be found in Ref. [17]. Hitherto, the MG2 potential was only available as a part of the GULP or the TREMOLO-X packages. [32, 33, 34] In this work, we implemented the MG2 potential into the LAMMPS package and performed all computations within LAMMPS. [26]

In a recent comparative study on empirical potential simulations of amorphous Si_3N_4, we indicate that models obtained using the MG2 potential contain only few coordination defects. By contrast, several different parameterizations of the Tersoff potential produce far higher proportions of over- and under-coordinated atoms, especially 3-coordinated Si atoms. [35] We gain similar experience while modeling amorphous SiBN, for which we previously used a Tersoff potential. [9, 18] The MG2 potential produces "low defect" models that are close to a DFT local energy minimum, while Tersoff models contain many coordination defects and require substantial additional optimization. Moreover, the MG2 potential has a performance advantage due to its nature of a two-body potential, despite the longer cut-off. The CPU time needed using MG2 potential is only 60% of that of the Tersoff potential during MD simulations. Overall, we find that the MG2 potential is better suited for modeling amorphous SiBN than the Tersoff potential.

Results and Discussions

1) Structure and Enthalpy of formation

SiBN network models of Set 1 have been characterized previously. [18] In brief, network models optimized in DFT exhibit SiN_4-tetahedra, BN_3-triangels, and mixed NSi_nB_{3-n} triangular environments. Only few defects are present, and on average less than 1% of Si atoms appear under-coordinated. In models with high BN content (e.g.: $Si_3B_9N_{13}$) we observe either predominantly "layered" structures, in which BN sheets are bridged by Si atoms, or "dispersed" structures without apparent layers.

Taking SiBN models of Set 1 that are optimized within DFT and subjecting them to local optimizations using the MG2 potential, requires only few optimization steps to converge forces and stresses. Reversely, the adopted MG2 local ground state structure requires only few optimization steps in DFT to converge back to the initial configuration. This behavior indicates close proximity of the local ground states of empirical MG2 potential with DFT ground state. By

contrast, DFT-optimizations of SiBN models, which have been generated using the Tersoff potential first, yield significant structural distortions including bond ruptures. [18] Figures of small network models of Set 1 are included with Ref [18]. In Figure 1, we present large models from Set 1 and models from Set 2.

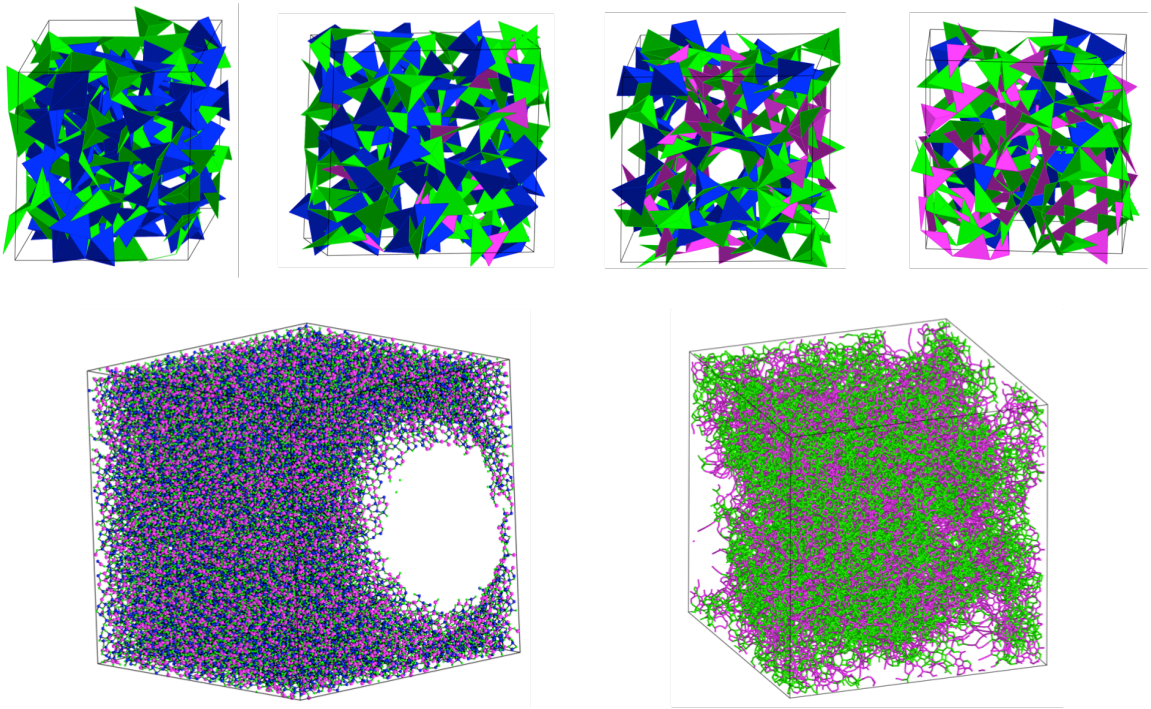

Figure 1: (Top) Representative models of amorphous SiBN (Set 1). From left to right: a-Si_3N_4 (Si_3N_4: BN = 1:0, 224 atoms); a-Si_3BN_5 (Si_3N_4: BN = 1:1, 216 atoms); $Si_3B_3N_7$ (Si_3N_4: BN = 1:3, 208 atoms) and $Si_3B_9N_{13}$ (Si_3N_4: BN = 1:9, 200 atoms). (Bottom): Representative models of a-$Si_3B_3N_7$ (53248 atoms) from Set 2. These models are generated from the MG2 potential using a melt-and-quench scheme. (Left): Model with density = 1.6 g·cm^{-3} shows formation of large "voids". Color-coding: Si – Blue tetrahedra/sphere, B – pink triangle/sphere and N – green spheres (Right): a-$Si_3B_3N_7$ (density = 1.8 g·cm^{-3}) showing population of Si-N (green) and B-N bonds (pink)

The enthalpy of formation, ΔH_f, of models of Set 1 is computed relative to crystalline β-Si_3N_4 and h-BN. For the lowest energy model of each composition we obtain (DFT value stated; MG2 result in parentheses) ΔH_f = 0.21 (0.17) eV/atom for a-Si_3N_4, 0.25 (-0.02) eV/atom for a-Si_3BN_5, 0.33 (-0.04) eV/atom for a-$Si_3B_3N_7$, and two values for a-$Si_3B_9N_{13}$, 0.25 (-0.04) eV/atom and 0.17 (-0.06) eV/atom, depending on whether the model is "dispersed" or "layered". Obviously, the

MG2 potential favors a mixing of Si_3N_4 and BN in the amorphous state, thus preferring mixed a-SiBN models to models comprising regions of segregated a-Si_3N_4 and a-BN. We find the same bias towards mixed a-SiBN in large-scale models produced by the melt-quench method. Experimentally, however, quite the opposite is observed with a-SiBN segregating into SiB-rich and BN-rich regions. [36] Previous computational work does not address this deficiency of the MG2 potential. Since this bias in structure simulations may have significant implications for simulations of thermal conductivity, we propose a simple modification to the MG2 potential. Increasing the repulsion between Si and B slightly (e.g. by increasing the parameters A and ρ by 6 %) produces models of a-SiBN with modest but visible segregation (see Fig.1, bottom right). The modification does not change elastic constants or vibrational frequencies computed of Si_3N_4 or BN structures, which were part of the original training set of the potential. [17] This increased repulsion only affects the modeling of amorphous SiBN structures.

2) Thermal conductivity using Clarke's phenomenological model

Once the elastic constants of SiBN models of Set 1 are computed within DFT, it is straightforward to calculate the lattice thermal conductivity in the high temperature limit, κ_{min}, according to Clarke's model. [20] For each composition we compute κ_{min} for 2–5 independent models, and show averages together with standard errors in Table 1. κ_{min} shows only a slight increase with increasing BN content. However, the trend is barely exceeding the margin of error.

Composition	Mol % BN	κ_{min} ($Wm^{-1}K^{-1}$)
Si_3N_4	0	2.3 ± 0.1
Si_3BN_5	50	2.4 ± 0.2
$Si_3B_3N_7$	75	2.5 ± 0.1

"dispersed" $Si_3B_9N_{13}$	90	2.6 ± 0.2
"layered" $Si_3B_9N_{13}$	90	2.7 ± 0.1

Table 1: Lattice thermal conductivity (κ_{min}) of Si-B-N models computed with Clarke's Model. Uncertainties in the values arise from multiple amorphous models considered for the same composition.

ii) Thermal conductivity applying the Green-Kubo method using equilibrium MD simulations

In Figure 2 we plot the heat current (z-component, $\mathbf{J}_z$) auto-correlation function (HCACF) for a-Si_3BN_5 (55296 atoms) averaged over five independent MD simulations at 300 K for a correlation time of 100 ps. The HCACF is "smooth" and converges to zero after approximately 5 ps (inset in Fig. 2). By contrast, using the Tersoff potential required 20 ps of simulation time to achieve similar convergence. [18]

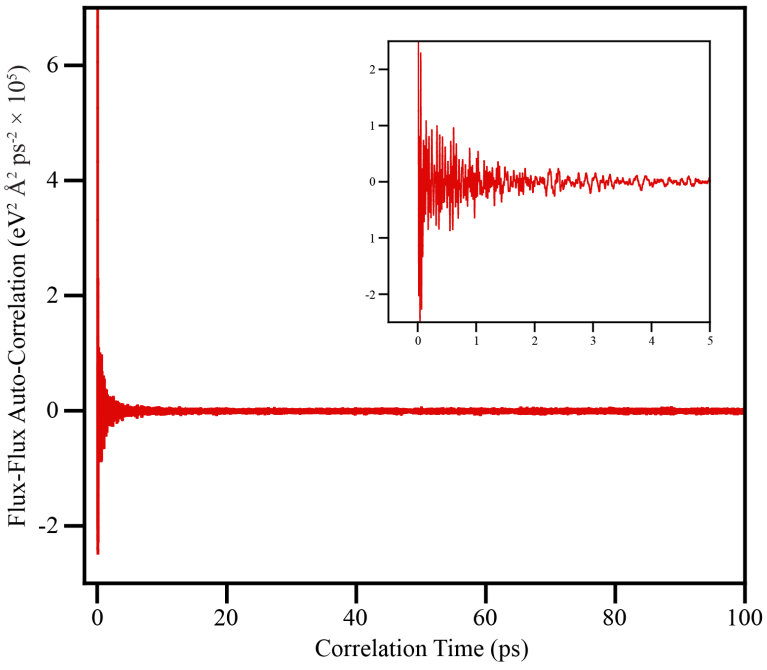

Figure 2: Heat current auto-correlation function (HCACF) at 300 K for a-Si_3BN_5 averaged over five independent MD simulations using different starting conditions (initial velocities of atoms). This model from Set 2 comprises of 55296 atoms. (Inset) A magnified portion of the same auto-correlation function plotted to 5 ps.

Crystalline structures

Table 2 lists the diagonal components of the thermal conductivity tensor for crystalline SiBN compounds at room temperature and 2100 K. We also include the data obtained by Clarke's phenomenological model using elastic contacts computed by DFT.

	300 K			2100 K			Clarke's Models
Composition	κ_{xx}	κ_{yy}	κ_{zz}	κ_{xx}	κ_{yy}	κ_{zz}	κ_{min}
β-Si_3N_4	21.8 ± 1.4	24.3 ± 1.9	55.6± 2.9	3.3 ± 0.2	4.1 ± 0.3	5.3 ± 1.0	2.5
α-3-Si_3BN_5	9.8 ± 0.6	8.9 ± 0.8	17.7 ± 0.9	2.4 ± 0.2	2.4 ± 0.1	3.8 ± 0.3	2.7
β-1-$Si_3B_3N_7$	10.3 ± 0.5	8.8 ± 0.4	29.0 ± 2.1	2.0 ± 0.2	1.8 ± 0.1	2.8 ± 0.2	2.3
h-BN	374.5 ± 21.3	387.5 ± 19.2	1.3 ± 0.4	24.2 ± 0.6	27.5± 0.1	0.5± 0.0	2.4

Table 2: Thermal conductivity of crystalline phases of SiBN compositions (β-Si_3N_4, α-3-Si_3BN_5, β-1-$Si_3B_3N_7$ and h-BN). Standard errors are obtained from 5 independent simulations for each model. All values are in units of $Wm^{-1}K^{-1.}$

Crystalline models show a pronounced anisotropy with $\kappa_{xx} = \kappa_{yy} \neq \kappa_{zz}$, reminiscent of the procedure to generate them from Si_3N_4 polymorphs. [19] However, the computed thermal conductivity of β-Si_3N_4 is lower than experimental data. For example, at 300 K single-crystal β-Si_3N_4 has a thermal conductivity of 69 and 180 $Wm^{-1}K^{-1}$ along a- and c-direction, respectively. [37] At 1400 K, sintered polycrystalline β-Si_3N_4 still exhibits $\kappa \sim 28$ $Wm^{-1}K^{-1}$. [37] On the other hand, our data for h-BN at room and high temperature is in excellent agreement with reference data. Room temperature measurements for bulk h-BN shows its basal plane thermal conductivity (κ_{xx} and κ_{yy} in our case) to be ~ 400 $Wm^{-1}K^{-1}$. [38] At 1273 K, κ is measured between 24 – 28 $Wm^{-1}K^{-1}$ for hot pressed h-BN. [39] Data from Clarke's model clearly has its limitation, apparent when

comparing κ_{min} with our simulations or with experimental data. Nonetheless, at 2100 K, MD results for α-3-Si_3BN_5 and β-1-$Si_3B_3N_7$ are within 10% of their Clarke's model values, exhibiting convergence in empirical simulations and DFT methods.

Thermal Conductivity of network models (Set 1) by equilibrium MD simulations

The temperature dependence of κ_{trace} of network models (Set 1) is plotted in Fig. 3 for each composition. At 300 K, κ of a- Si_3N_4 is 2.3 ± 0.1 $Wm^{-1}K^{-1}$, while for 90 % BN-rich $Si_3B_9N_{13}$ κ is 4.7 ± 0.1 $Wm^{-1}K^{-1}$ and 6.9 ± 0.2 $Wm^{-1}K^{-1}$, depending on whether the model is "dispersed" or "layered". Thus, at room temperature thermal conductivity depends significantly on composition and increases with increasing mol % of BN. At elevated temperatures, however, the impact of composition on κ is lower. At 2100 K we find κ between 1.9 ± 0.1 $Wm^{-1}K^{-1}$ for Si_3N_4 and 2.4 ± 0.1 $Wm^{-1}K^{-1}$, for "layered" $Si_3B_9N_{13}$. These high temperature values match those listed in Tab. 1, which were computed using first-principles elastic constant calculations together with Clarke's formula. The excellent agreement between empirical potential simulations and DFT results in the high temperature limit also provides confidence in the computational approach. In the intermediate temperature range, κ of each composition decays almost exponentially. One may speculate that a major reduction of κ happens between 300 K and 1200 K, while the composition dependence remains pronounced. Above 1200 K, however, only marginal composition dependence is visible and a temperature variation of κ occurs only for BN-rich $Si_3B_9N_{13}$.

Experimentally, a value of about 2 W $m^{-1}K^{-1}$ at 300 K was suggested for thin films of a-Si_3N_4, independent of film thickness. [40, 41, 42] This agrees with our calculations (see Fig 3 and Tab. 1). Computational studies by Schön et al. for a-$Si_3B_3N_7$ using the MG2 potential together with non-equilibrium MD simulations suggested a thermal conductivity κ of 4.0 ± 1.0 $Wm^{-1}K^{-1}$ at 300 K and 4.0 ± 0.1 at 500 K for models with a density of 2.7 to 2.8 gcm^{-3}. [43] Our data is very close to these values, as we compute 3.7 ± 0.1 $Wm^{-1}K^{-1}$ at 300 K and 2.9 ± 0.1 $Wm^{-1}K^{-1}$ at 600 K.

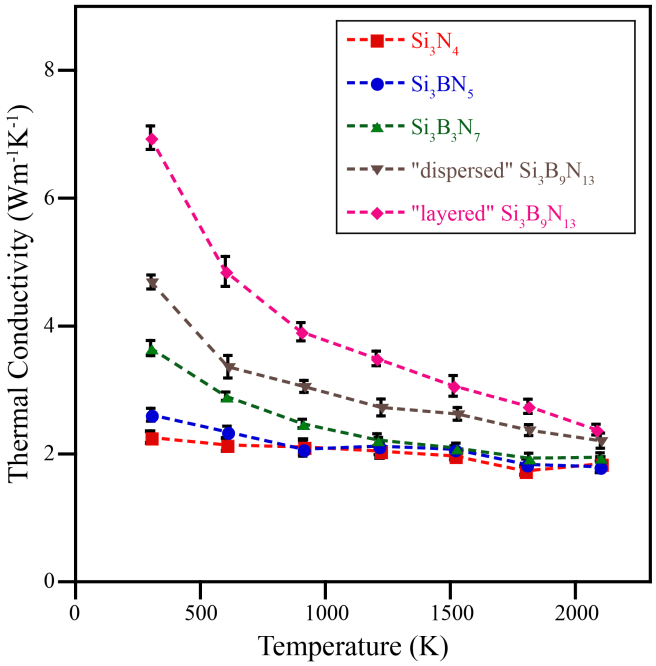

Figure 3: Thermal conductivity as a function of temperature in MD simulations for small a-SiBN models of Set 1. Thermal conductivity is distinct for different compositions at 300 K but soon converge to 2.1–2.7 $Wm^{-1}K^{-1}$ at higher temperatures.

A decrease in thermal conductivity of amorphous SiBN materials at elevated temperatures, as shown in Fig. 3, has not been reported before. Göbel et al. reports the thermal conductivity of amorphous $SiBN_3C$, a material that contains additional carbon, ceramic to be 0.490 ± 0.042 $Wm^{-1}K^{-1}$ at 300 K increasing to 0.726 ± 0.063 $Wm^{-1}K^{-1}$ at 773 K. Generally, an increase of κ above ~30 K is characteristic for most amorphous solids, e.g. a-Si, a-Ge, and silica glasses. This phenomenon is often explained by an increase in the population of vibrational modes that can transport heat current. [44, 45] On the other side, modeling studies of a-Si by Lee et al. show a decrease of thermal conductivity between 400 − 800 K due to an increasing number of coordination defects. [46] A similar effect does not apply for a-SiBN models, as we observe only minor coordination changes (< 1%) during simulations, even after 100 ps at 2100 K. Possible future work may involve modal contributions to thermal conductivity to analyze the temperature dependence of κ in more detail. [47]

Thermal conductivity of large-scale SiBN models

The previous section established a strong agreement between first-principles calculations and empirical potential simulations using the MG2 potential. Encouraged by this, we seek a more systematic analysis of thermal conductivity of SiBN materials. We explore an impact of composition and one of density, which relates to porosity of a structure. The network models exhibit densities between 2.8 and 3.0 $g \cdot cm^{-3}$. A typical experimental density of polymer-derived a-$Si_3B_3N_7$ is 1.9 $g \cdot cm^{-3}$. [48] In previous simulations of a-SiBN a density of 2.5 $g \cdot cm^{-3}$ was adopted. [49] While this is lower than a weighted average of β-Si_3N_4 (ρ = 3.20 $g \cdot cm^{-3}$) and h-BN (ρ = 2.34 $g \cdot cm^{-3}$), it is still larger than the experimental density. [50, 51] Since we can easily set a target density for large-scale SiBN models, we investigated densities of 2.1 and 3.2 g cm^{-3} for every composition. For the composition a-$Si_3B_3N_7$ we consider a range of models with densities between 1.6 $g \cdot cm^{-3}$ and 3.2 $g \cdot cm^{-3}$.

The dependence of κ on composition is depicted in Fig. 4 (left) at low (300 K) and high temperature (2100 K). The data shows clearly that κ increases with increasing BN content. The effect is stronger at room temperature than at high temperatures. Moreover, for dense models, the effect of composition is more pronounced than for models with low density. Figure 4 (Left) repeats the results of low thermal conductivity of a-SiBN materials in the high-temperature limit. At 2100 K, κ_{trace} varies between 2.0 (a-Si_3N_4) and 2.9 (a-$Si_3B_9N_{13}$) $Wm^{-1}K^{-1}$ for density = 3.2 $g \cdot cm^{-3}$ and between 1.1 (a-Si_3N_4) and 2.0 (a-$Si_3B_9N_{13}$) $Wm^{-1}K^{-1}$ in models with density = 2.1 $g \cdot cm^{-3}$.

The impact of density on thermal conductivity is shown more systematically for large models of a-$Si_3B_3N_7$ in Fig. 4 (Right). Comparing 300 K and 2100 K, κ varies by more than a factor of 2 for densities between 1.6 and 3.2 $g \cdot cm^{-3}$. A linear fit to the data according to $\kappa = \alpha[T] \cdot \rho$ yields a temperature-dependent constant, α [T]. We find values for α[T] of 1.4 $Wm^{-1}K^{-1}g^{-1}cm^3$ and 0.7 $Wm^{-1}K^{-1}g^{-1}cm^3$ at 300 K and 2100 K, respectively. It is generally observed that in ceramics the fraction of "open voids and pores" determines thermal conductivity. [52, 53] Voids and surfaces act

as scattering centers, effectively reducing the phonon mean free path and constraining thermal transport. Our data aligns with this observation: a dense structure of a-$Si_3B_3N_7$ with low "porosity" has higher κ in comparison to the open structure. We can use the fit and our data and estimate the value of thermal conductivity of polymer-derived a-$Si_3B_3N_7$ with density of 1.9 g·cm^{-3} and receive 2.7 Wm^{-1}K^{-1} at 300 K and 1.4 Wm^{-1}K^{-1} at 2100 K.

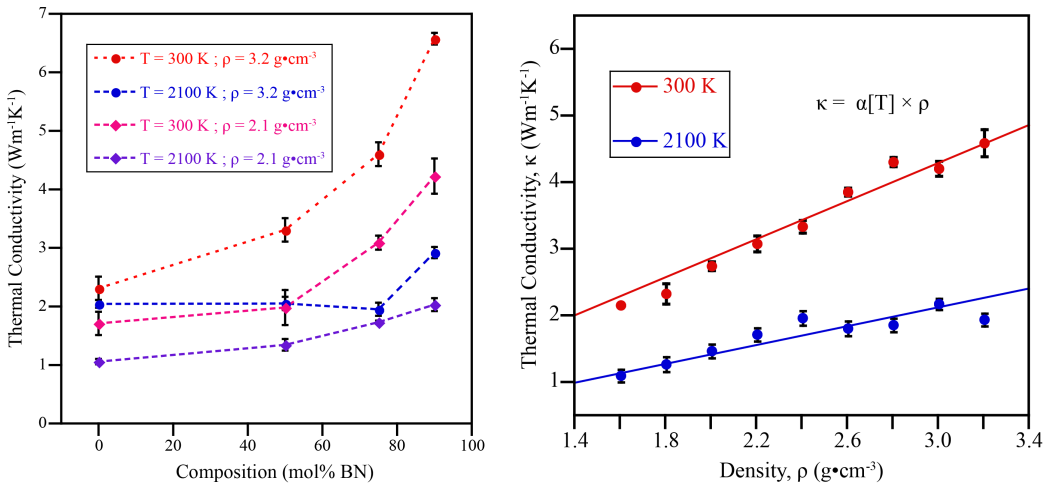

Figure 4: (Left) Thermal conductivity, κ, as a function of composition of large-scale a-SiBN models of Set 2. Graphs are for densities 2.1 g·cm^{-3} (red line for 300 K and blue line for 2100 K) and 3.2 g·cm^{-3} (pink line for 300 K and purple line for 2100 K). The dotted lines are a guide to the eye only. (Right) Thermal conductivity (κ_{trace}) of a-$Si_3B_3N_7$ models of Set 2 plotted as a function of density for 300 K and 2100 K. The straight line is a linear fit ($\kappa = \alpha[T]\cdot\rho$) to the data.

Summary and Conclusions

We characterize thermal conductivity of amorphous SiBN ceramics and its dependency on composition, density, and temperature. We apply both Density Functional Theory (DFT) calculations as well as molecular dynamic (MD) simulations using the empirical two-body Marian-Gastreich potential (MG2). We consider the compositions Si_3N_4:BN = 1:0 (Si_3N_4), 1:1 (Si_3BN_5), 1:3 ($Si_3B_3N_7$), and 1:9 ($Si_3B_9N_{13}$). Different types of a-SiBN models are investigated: small models (100 – 224 atoms) created via a network approach as well as large-scale models (51200 – 57344 atoms) generated using standard melt-quench simulations. For comparison and

reference, we include crystal structures of Si_3N_4 and BN, and hypothetical crystalline models of Si_3BN_5 and $Si_3B_3N_7$.

At high temperatures, the thermal conductivity of SiBN models is 2.3 – 2.7 $Wm^{-1}K^{-1}$ and depends only slightly on composition. Investigating small a-SiBN models, we find close agreement between first-principles calculations, which uses the Clarke's model to estimate thermal conductivity in the high-temperature limit through calculations of elastic constants, and equilibrium MD simulations, which compute thermal conductivity using the Green-Kubo approach. MD simulations show that the thermal conductivity decays almost exponentially when temperature is increased from 300 K to 2100 K. While a definitive cause for this decrease is beyond the scope of this paper, it serves as potential topic for future research.

A systematic investigation of large-scale amorphous SiBN models shows that thermal conductivity increases with increasing BN content. The impact of composition is stronger at low temperatures compared to high temperatures and more pronounced in dense models than in open models. Studying a-$Si_3B_3N_7$ in more detail, we find a linear relation between thermal conductivity and density, with a slope dependent on temperature.

Based on this investigation of thermal conductivity of SiBN ceramics, we can make a hypothesis about thermal conductivity of SiBNC fiber materials, which display additional carbon in the structure. Solid-state NMR of SiBNC shows that after annealing at 1673 K the material comprises segregated graphite-like carbon embedded within an amorphous SiBN matrix. [54, 55] We expect that thermal conductivity of this composite will depend on the amount and extent of each constituent, as well as on their structural relation.

References

1. H. P. Baldus and M. Jansen, "Novel high-performance ceramics - Amorphous inorganic networks from molecular precursors," *Angew Chem Int Edit,* 36[4] 329-43 (1997).

2. P. Baldus, M. Jansen, and D. Sporn, "Ceramic fibers for matrix composites in high-temperature engine applications," *Science,* 285[5428] 699-703 (1999).

3. R. Riedel, A. Kienzle, W. Dressler, L. Ruwisch, J. Bill, and F. Aldinger, "A silicoboron carbonitride ceramic stable to 2,000 degrees C," *Nature,* 382[6594] 796-98 (1996).

4. H. P. Baldus and G. Passing, "Studies on SiBN(C)-ceramics: Oxidation- and Crystallization Behavior Lead the Way to Applications," *MRS Proceedings,* 346 (1994).

5. H. Cakmak and M. Jansen, "Amorphous Si3B3N7 Ceramic as a Versatile Host for Inorganic Phosphor Activators," *Adv Funct Mater,* 24[4] 460-64 (2014).

6. H. P. Baldus, M. Jansen, and O. Wagner, "New Materials in the System Si(N-C)B and Their Characterization," *Key Engineering Materials,* 89-91 75-80 (1994).

7. M. Maeda and T. Makino, "Low Dielectric-Constant Amorphous Sibn Ternary Films Prepared by Plasma-Enhanced Deposition," *Jpn J Appl Phys 1,* 26[5] 660-65 (1987).

8. R. M. Hagenmayer, U. Muller, C. J. Benmore, J. Neuefeind, and M. Jansen, "Structural studies on amorphous silicon boron nitride Si3B3N7 : neutron contrast technique on nitrogen and high energy X-ray diffraction," *J Mater Chem,* 9[11] 2865-70 (1999).

9. K. Matsunaga and Y. Iwamoto, "Molecular dynamics study of atomic structure and diffusion behavior in amorphous silicon nitride containing boron," *J Am Ceram Soc,* 84[10] 2213-19 (2001).

10. N. B. Liao, W. Xue, and M. Zhang, "Molecular dynamics investigation of Si-B-N ceramics: effects of boron content," *Model Simul Mater Sc,* 20[3] (2012).

11. M. Griebel and J. Hamaekers, "Molecular dynamics, simulations of boron-nitride nanotubes embedded in amorphous Si-B-N," *Comput Mater Sci,* 39[3] 502-17 (2007).

12. V. Drach, H. P. Ebert, and J. Fricke, "Noncontact determination of the thermal conductivity of fibres," *High Temp-High Press,* 32[3] 337-46 (2000).

13. A. Gobel, F. Hemberger, H. P. Ebert, M. Jansen, and J. Wilfert, "Thermophysical properties of an amorphous polymer-derived Si/B/N/C ceramic," *Thermochim Acta,* 520[1-2] 20-24 (2011).

14. A. B. Kousaalya, R. Kumar, and B. T. N. Sridhar, "Thermal conductivity of precursor derived Si-B-C-N ceramic foams using Metroxylon sagu as sacrificial template," *Ceram Int,* 41[1] 1163-70 (2015).

15. J. C. Schon, A. Hannemann, and M. Jansen, "Modeling the synthesis of amorphous Si3B3N7 via a sequence of dynamically well-separated steps," *J Phys Chem B,* 108[7] 2210-17 (2004).
16. A. Hannemann, J. C. Schon, and M. Jansen, "Modeling the sol-gel synthesis route of amorphous Si3B3N7," *J Mater Chem,* 15[11] 1167-78 (2005).
17. C. M. Marian, M. Gastreich, and J. D. Gale, "Empirical two-body potential for solid silicon nitride, boron nitride, and borosilazane modifications," *Phys Rev B,* 62[5] 3117-24 (2000).
18. J. Al-Ghalith, A. Dasmahapatra, P. Kroll, E. Meletis, and T. Dumitrică, "Compositional and Structural Atomistic Study of Amorphous Si–B–N Networks of Interest for High-Performance Coatings," *J Phys Chem C,* 120[42] 24346-53 (2016).
19. P. Kroll and R. Hoffmann, "Silicon boron nitrides: Hypothetical polymorphs of Si3B3N7," *Angew Chem Inter Ed,* 37[18] 2527-30 (1998).
20. D. R. Clarke, "Materials selection guidelines for low thermal conductivity thermal barrier coatings," *Surf Coat Tech,* 163 67-74 (2003).
21. R. Kubo, "The fluctuation-dissipation theorem," *Reports on Progress in Physics,* 29[1] 255 (1966).
22. P. Kroll, "Modelling polymer-derived ceramics," *J Eur Ceram Soc,* 25[2-3] 163-74 (2005).
23. G. Kresse and J. Furthmüller, "Efficiency of ab-initio total energy calculations for metals and semiconductors using a plane-wave basis set," *Comput Mater Sci,* 6[1] 15-50 (1996).
24. G. Kresse and J. Hafner, "Ab initio molecular dynamics for liquid metals," *Phys Rev B,* 47[1] 558-61 (1993).
25. G. Kresse and J. Hafner, "Ab initio molecular-dynamics simulation of the liquid-metal amorphous-semiconductor transition in germanium," *Phys Rev B,* 49[20] 14251-69 (1994).
26. S. Plimpton, "Fast Parallel Algorithms for Short-Range Molecular-Dynamics," *J Comput Phys,* 117[1] 1-19 (1995).
27. A. Hannemann, J. C. Schon, M. Jansen, H. Putz, and T. Lengauer, "Modeling amorphous $Si_3B_3N_7$: Structure and elastic properties," *Phys Rev B,* 70[14] (2004).

28. A. Reuss, "Berechnung der Fließgrenze von Mischkristallen auf Grund der Plastizitätsbedingung für Einkristalle," *ZAMM - Journal of Applied Mathematics and Mechanics / Zeitschrift für Angewandte Mathematik und Mechanik,* 9[1] 49-58 (1929).

29. W. Voigt, "Lehrbuch der Kristallphysik." B. B. Teubner: Leipzig, (1928).

30. R. Hill, "The Elastic Behaviour of a Crystalline Aggregate," *Proc Phys Soc A,* 65[5] 349 (1952).

31. P. K. Schelling, S. R. Phillpot, and P. Keblinski, "Comparison of atomic-level simulation methods for computing thermal conductivity," *Phys Rev B,* 65[14] (2002).

32. J. D. Gale, "GULP: A computer program for the symmetry-adapted simulation of solids," *J Chem Soc Faraday T,* 93[4] 629-37 (1997).

33. J. D. Gale and A. L. Rohl, "The General Utility Lattice Program (GULP)," *Mol Simulat,* 29[5] 291-341 (2003).

34. M. Griebel, Knapek, Stephan, Zumbusch, Gerhard, "Numerical Simulation in Molecular Dynamics," pp. 476 Vol. 5, (2007).

35. A. Dasmahapatra and K. Peter, "Modeling amorphous Silicon Nitride: A comparative study of empirical potentials," *Submitted to Comput Mater Sci* (2017).

36. L. van Wullen, U. Muller, and M. Jansen, "Understanding intermediate-range order in amorphous nitridic ceramics: A Si-29{B-11} REDOR/REAPDOR and B-11{Si-29} REDOR study," *Chem Mater,* 12[8] 2347-52 (2000).

37. N. Hirosaki, S. Ogata, C. Kocer, H. Kitagawa, and Y. Nakamura, "Molecular dynamics calculation of the ideal thermal conductivity of single-crystal alpha- and beta-Si_3N_4," *Phys Rev B,* 65[13] (2002).

38. E. K. Sichel, R. E. Miller, M. S. Abrahams, and C. J. Buiocchi, "Heat-Capacity and Thermal-Conductivity of Hexagonal Pyrolytic Boron-Nitride," *Phys Rev B,* 13[10] 4607-11 (1976).

39. A. Lipp, K. A. Schwetz, and K. Hunold, "Hexagonal boron nitride: Fabrication, properties and applications," *J Eur Ceram Soc,* 5[1] 3-9 (1989).

40. B. L. Zink and F. Hellman, "Specific heat and thermal conductivity of low-stress amorphous Si-N membranes," *Solid State Commun,* 129[3] 199-204 (2004).

41. S. M. Lee and D. G. Cahill, "Heat transport in thin dielectric films," *J Appl Phys,* 81[6] 2590-95 (1997).

42. C. H. Mastrangelo, Y. C. Tai, and R. S. Muller, "Thermophysical Properties of Low-Residual Stress, Silicon-Rich, Lpcvd Silicon-Nitride Films," *Sensor Actuat a-Phys,* 23[1-3] 856-60 (1990).

43. J. C. Schön, A. Hannemann, G. Sethi, V. I. Pentin, and M. Jansen, "Modelling structure and properties of amorphous silicon boron nitride ceramics," *Processing and Application of Ceramics,* 5[2] 49-61 (2011).

44. D. G. Cahill and R. O. Pohl, "Thermal-Conductivity of Amorphous Solids above the Plateau," *Phys Rev B,* 35[8] 4067-73 (1987).

45. C. Kittel, "Interpretation of the Thermal Conductivity of Glasses," *Phys Rev,* 75[6] 972-74 (1949).

46. Y. H. Lee, R. Biswas, C. M. Soukoulis, C. Z. Wang, C. T. Chan, and K. M. Ho, "Molecular-Dynamics Simulation of Thermal-Conductivity in Amorphous-Silicon," *Phys Rev B,* 43[8] 6573-80 (1991).

47. W. Lv and A. Henry, "Direct calculation of modal contributions to thermal conductivity via Green-Kubo modal analysis," *New J Phys,* 18 (2016).

48. J. T, "Hochtemperaturstabile Si/B/N/C-Keramiken aus neuen Einkomponentenvorläufern ". in, Vol. Ph.D. University of Bonn, 2002.

49. M. Doerr and C. M. Marian, "Reverse Monte Carlo modelling of amorphous $Si_3B_3N_7$ using scattering and N-15 NMR data," *J Phys-Condens Mat,* 19[5] (2007).

50. O. Mishima and K. Era, "Science and Technology of Boron Nitride." in Electric Refractory Materials**.** CRC Press, 2000.

51. C. M. Wang, X. Q. Pan, M. Ruhle, F. L. Riley, and M. Mitomo, "Silicon nitride crystal structure and observations of lattice defects," *J Mater Sci,* 31[20] 5281-98 (1996).

52. J. Francl and W. D. Kingery, "Thermal Conductivity: IX, Experimental Investigation of Effect of Porosity on Thermal Conductivity," *J Am Ceram Soc,* 37[2] 99-107 (1954).
53. E. Y. Litovsky and M. Shapiro, "Gas Pressure and Temperature Dependences of Thermal Conductivity of Porous Ceramic Materials: Part 1, Refractories and Ceramics with Porosity below 30%," *J Am Ceram Soc,* 75[12] 3425-39 (1992).
54. J. Schuhmacher, F. Berger, M. Weinmann, J. Bill, F. Aldinger, and K. Muller, "Solid-state NMR and FT IR studies of the preparation of Si-B-C-N ceramics from boron-modified polysilazanes," *Appl Organomet Chem,* 15[10] 809-19 (2001).
55. S. Sarkar, Z. H. Gan, L. N. An, and L. Zhai, "Structural Evolution of Polymer-Derived Amorphous SiBCN Ceramics at High Temperature," *J Phys Chem C,* 115[50] 24993-5000 (2011).

Appendix 5:

In this section, I include supplementary information on investigation of thermal conductivity of a-SiBN models using the MG2 potential. [1]

A5.1) Coding the Flux-flux auto-correlation using MATLAB: Thermal conductivity using Green-Kubo Method:

A code is written in MATLAB to calculate thermal conductivity. As is shown in the article, the Green-Kubo (G-K) formalism for thermal conductivity is as follows: [2]

$$\frac{1}{Vk_BT^2}\int_0^\infty \langle J(0)J(t)\rangle\, dt$$

where t, T, V and J are respectively time, temperature, volume and heat current. The G-K method relates the thermal conductivity to the integral of heat current auto-correlation function (HCACF). A majority of the G-K formula is straightforward however more detail is necessary to define the ensemble average of the HCACF.

Autocorrelation is a measure of similarity between a time dependent function and itself at a different time. It shows how similar a function is to itself at a different/later time. To plot the HCACF, J(t) must be compared to J(0) and time lag between them be progressively increased. In this code, I use the signal processing definition of autocorrelation:

$$\mathrm{HCACF}(\tau) = \sum_n \mathrm{J}(0)\mathrm{J}(0+\tau)$$

The above formula can be simply defined as the dot product of two matrices. MATLAB is a matrix oriented calculation program. Snippets of the code is as follows:

Variable definition: k = time-lag of auto-correlation; corr_length = length of correlation time; a1x is a variable for J(0) and a2x is J(t); corrax is the auto-correlation product.

```
...
for k=0:corr_length
   a1x = Jx(k+1:nab);
```

```
    a2x = Jx(1:nab-k);
...
corrax(k+1) = a1x * a2x';
...
```

The more correlated the heat current is the longer it will take to decay to zero (it must decay eventually as no material has an infinite thermal conductivity). Given the longer decay time the value of the integral will be increased thus yielding a greater thermal conductivity

Auto-correlation curves computed within the MG2 potential appear "smoother" and decay rapidly (within 5 ps) to zero as compared to that of Tersoff potential (see Fig. A5.1). Moreover, only 5 averages are necessary to achieve convergence in κ values as compared to 20 for the Tersoff potential. It should be noted that negative autocorrelation is a possibility. Autocorrelation is an indication of how the function will behave compared to an original function. Negative autocorrelation indicates that the function is behaving in the opposite manner. In terms of thermal conductivity, negative autocorrelation indicates that heat flow reversing direction.

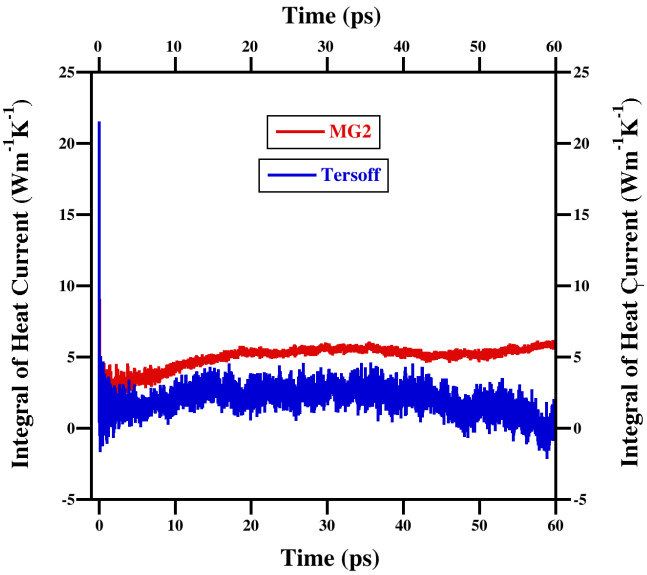

Figure A5.1: Integral of Heat current autocorrelation function (HCACF) for 4x4x4 super cell of a-Si_3BN_5 at 300K using Tersoff potential (blue) and MG2 potential (in red). The number of independent simulations considered is 20 for Tersoff while for MG2 potential it is only 5.

A5.2) Modeling a-$Si_3B_3N_7$ with repulsion:

Increasing the repulsion between Si and B by increasing the parameters A and ρ by 6 % produces a-$Si_3B_3N_7$ models segregation. The choice of 6 % comes by trial and error. In Figure A5.2 I show three a-$Si_3B_3N_7$ models with 832 atoms that have 3 and 10 % increase in A and ρ. While the model with 3 % increase doesn't show ant segregated BN regions, 10 % increase in potential parameters leads to two separated phases – Si_3N_4 interspersed between BN.

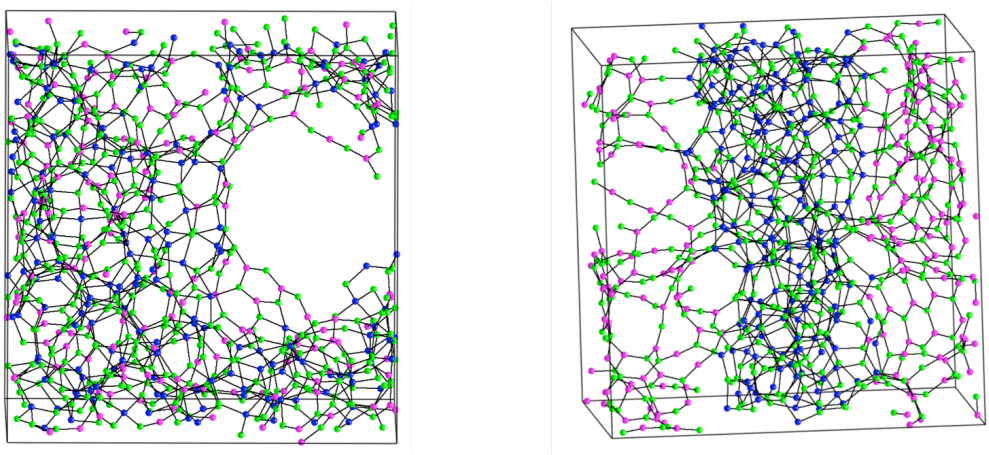

Figure A5.2: Models of a-$Si_3B_3N_7$ consisting of 832 atoms with (left) 3 % increase and (right) 10 % in Si-B repulsion. Both models have density 1.8 g•cm^{-3} and show the presence of pores and voids.

Although regions of clustered BN are formed as a result of modifying the parameters, thermal conductivity of these "modified potential" models compared to "original potential" models do not change with varying density. (See Fig. A5.3). Therefore, it can be inferred that "long extended BN units" are necessary for increased thermal conductivity in a-SiBN systems.

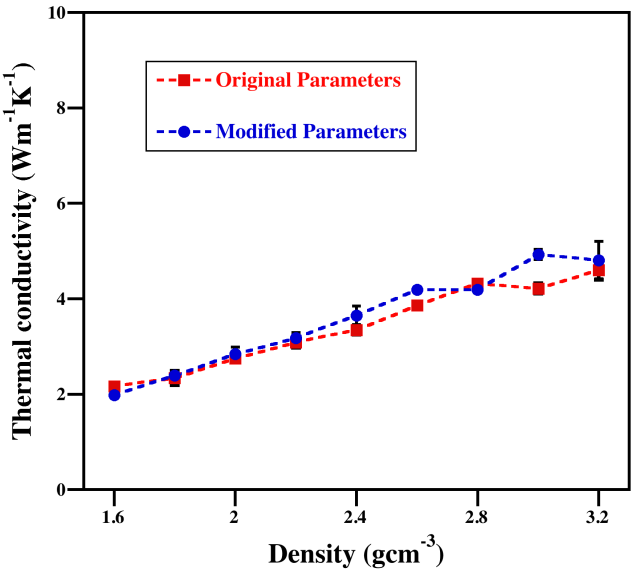

Figure A5.3: Thermal conductivity of a-$Si_3B_3N_7$ models (with 53248 atoms, Set 2) plotted as a function of their density. The plot consists of models with (red) original parameters and (blue) modified parameters. The dotted line is a guide to the eye and connects data points for the models generated with identical potential parameters. Standard errors arise from 3 models of the same density.

A5.2) Porosity and thermal conductivity: At 300 K

A popular concept in amorphous systems is to define thermal conductivity as a function of the porosity of the models. [3, 4] Porosity is defined as:

$$\phi = \frac{\text{Volume of voids}}{\text{Total volume}} = 1 - \frac{\rho \text{ of the amorphous SiBN model}}{\rho \text{ of crystalline } Si_3B_3N_7}$$

Density of crystalline β-2-$Si_3B_3N_7$ = 2.65 g/cm^3. [5] It is assumed that the crystalline model is 100 % dense. However, in this approach, models for which calculated density exceeds the crystalline model are excluded, as that leads to negative porosity, which is unrealistic. Alternatively, it can also be assumed that the amorphous model with density = 3.2 g/cm^3 is 100 % dense. In Table A5.1, I include porosity (ϕ) data from both approaches against the density. Density of a-SiBN is calculated as an average from 5 independent models. Linear fits to both approaches show that κ increases as porosity of the model decreases as a function of the equation: κ = (3.6 ± 0.1)[1-ϕ] for porosity calculated from assumption 1 and κ = (4.4

± 0.1) [1−ϕ] for porosity caluclated from assumption 2. Thus if ϕ is 0, i.e. for the most dense, least porous model, the κ is obtained. Thus from the slope of the linear fit, κ of β-2-$Si_3B_3N_7$ is 3.6 $Wm^{-1}K^{-1}$ and for a-$Si_3B_3N_7$ (ρ = 3.2 g•cm^{-3}) is 4.4 $Wm^{-1}K^{-1}$.

Density (g•cm^{-3})	1− ϕ (from crystalline model)	1− ϕ (from dense amorphous model)	κ ± standard error
1.649	0.62	0.53	2.2 ± 0.0
1.85	0.70	0.60	2.3 ± 0.1
2.06	0.78	0.66	2.7 ± 0.1
2.27	0.85	0.73	3.1 ± 0.1
2.49	0.94	0.80	3.3± 0.1
2.67	1.00	0.86	3.9 ± 0.1
2.81	-	0.91	4.3 ± 0.0
2.96	-	0.95	4.22± 0.1
3.20	-	1.00	4.60± 0.1

Table A5.1: Porosity (ϕ) v/s thermal conductivity (κ) of a-$Si_3B_3N_7$ models. The porosity is computed from two approaches – 1) assuming the crystalline $Si_3B_3N_7$ is the most dense phase and 2) assuming that a-$Si_3B_3N_7$ with ρ = 3.2 g•cm^{-3} is the most dense. In both cases the thermal conductivity increases linearly with the density of the model.

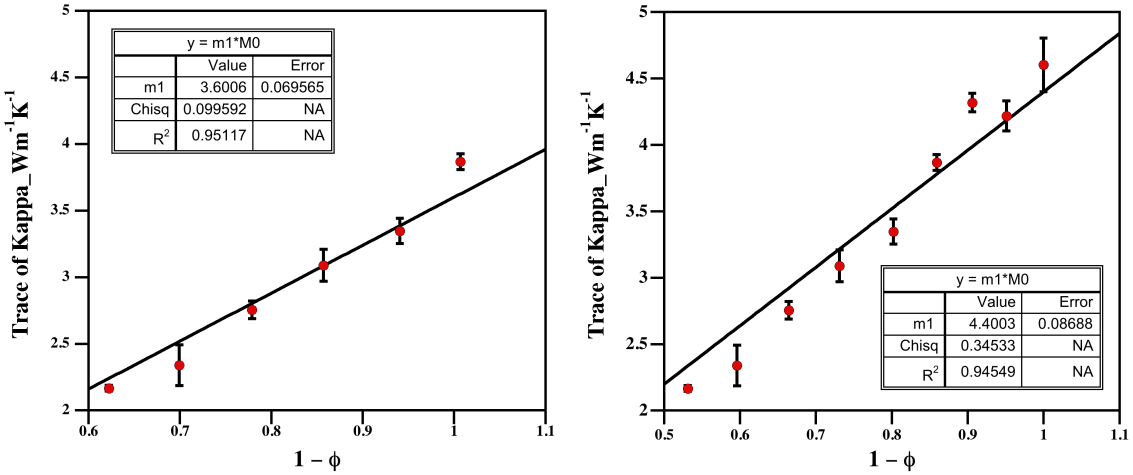

Figure A5.4: (Left) Porosity v/s thermal conductivity (κ) assuming crystalline β-2-$Si_3B_3N_7$ is the least porous system. (Right) Porosity v/s κ if amorphous $Si_3B_3N_7$ with density 3.2 g•cm^{-3} is considered to be least porous and most dense.

References:

[1] C.M. Marian, M. Gastreich, J.D. Gale, Empirical two-body potential for solid silicon nitride, boron nitride, and borosilazane modifications, Phys Rev B 62(5) (2000) 3117-3124.

[2] R. Kubo, The fluctuation-dissipation theorem, Reports on Progress in Physics 29(1) (1966) 255.

[3] A.L. Loeb, Thermal Conductivity: VIII, A Theory of Thermal Conductivity of Porous Materials, Journal of the American Ceramic Society 37(2) (1954) 96-99.

[4] J. Francl, W.D. Kingery, Thermal Conductivity: IX, Experimental Investigation of Effect of Porosity on Thermal Conductivity, Journal of the American Ceramic Society 37(2) (1954) 99-107.

[5] P. Kroll, R. Hoffmann, Silicon boron nitrides: Hypothetical polymorphs of Si3B3N7, Angew Chem Int Edit 37(18) (1998) 2527-2530.

Summary:

This chapter continues the investigation of thermal conductivity of amorphous silicon boron nitride material. I use an "improved" potential and arrive at major conclusions:

1. The thermal conductivity of a-SiBN is strongly dependent on the density and composition of the material at 300 K.

2. Temperature dependence of thermal conductivity suggests an increasing trend that is contrary to popular belief regarding amorphous systems.

3. With increasing temperature, thermal conductivity trends toward constant value, which strongly agrees with the predicted Clarke's value. Thus, an agreement is achieved between quantum and classical mechanics methods.

4. The Marian-Gastriech two-body potential enables the generation of large-scale realistic models of a-SiBN which echo the κ of smaller models.

5. The first investigation of κ for crystalline structures of SiBN.

6. The MG2 potential wrongly predicts a mixture of Si_3N_4 and BN to be more stable than the crystalline analogues. This work takes a step to correct this deficiency by proposing a slight modification to the potential.

Thus, using the MG2, thermal conductivity of a-SiBN is correctly studied. Future research is to investigate model contributions to thermal conductivity to investigate why it decreases with increasing temperature.

CONCLUSIONS

Conclusions:

Amorphous materials have manifold applications in today's world. Computational modeling of amorphous materials and glasses are key to understanding the microstructure which is reflected in the macroscopic properties of the material. The work in this thesis aims to highlight the modeling of both oxide and non-oxide ceramics using density functional theory (DFT) as well as classical molecular dynamics (MD). Models are constructed using the melt-and-quench method in the domain of ab-initio MD or classical MD. Thereafter models are annealed for significant a time to remove any structural defects. This procedure of structure generation is a mimic of experimental techniques. After the structures are optimized for their atom positions, various physical and chemical properties are computed. Some of these properties are:

1) Local geometry od atoms
2) Site-site distance pair correlation function or g(r) – Information about the bonding statistics is obtained from this property computation. The first peak in a g(r) plot usually gives information about the most prevalent bond in the material. For instance in a-Si_3N_4, the first peak occurs at 1.7 A, which is the length of the Si-N bond.
3) Vibrational Spectra – Force constants are computed that in turn provide information about the phonon density of states and Infrared spectra.
4) Mechanical properties – The bulk, shear and Young's modulus gives information about the mechanical strength of the material.
5) Thermal conductivity – Thermal conductivity for the amorphous systems are computed using phenomenological models as well as the equilibrium Green Kubo method.

Using the abovementioned structure generation and property computation techniques, I studied a variety of systems. The first chapter highlighted the modeling of hafnia-silica (HfO_2-SiO_2) glass. These glasses are generated by insertion of 1-4 HfO_2 units in a network of SiO_2 glass. Although

small in size (box length ~ 11 Å), these models showed that at even at low concentrations (10 mol %) of HfO_2 dissolved in SiO_2 clustering of HfO_x units occurred.

In chapter 2, Zr-Si-B-C-N amorphous composites are investigated. Modeling techniques involved a melt and quench (MQ) technique followed by simulated annealing. The total simulation time for MQ was ~100 ps. Two or three cycles of annealing (each cycle is ~200 ps) revealed nucleation of ZrC(N) units inside the amorphous models. However, with increasing mol % of Si_3N_4 in the models, the amorphous phase becomes prevalent leading to loss in mechanical hardness of the material.

The third chapter is in the region of empirical potentials. Si_3N_4 is commonly modeled using the Tersoff potential or Vashishta potential. However, my research in the comparative study of modeling amorphous Si_3N_4 using 9 different empirical potential showed that the MG2 and the SG potential are reliable. While the Vashishta potential produced "semi-crystalline" 448 atom models, the Tersoff models had high enthalpy of formation and coordination defects. The Marian-Gastreich 3 body potential produced over-coordinated Si atoms. As a part of this project, the MG2 potential was implemented in to LAMMPS MD code, for the first time.

The fourth and fifth chapter, both dealt with the thermal conductivity of amorphous SiBN models. In amorphous SiBN material, thermal conductivity was found to weakly depend on the BN content if Tersoff potential is used as the choice of empirical potential. However, as emphasized in the chapter appendix, the Tersoff potential proved to be a poor choice. Long, computationally expensive simulations were necessary for convergence of κ values. A better empirical potential (the MG2 potential) produces reliable data. In addition, due to the availability of MG2 potential in LAMMPS simulations of large-scale models with 50000 atoms can be genarated that highlighted that k in these materials was a function of their density, composition and the temperature of the study.

Thus, this work proposes realistic modeling of amorphous systems and glasses with convincing property calculations. Major acheivements include establishment of a recipe for genration of amorphous models that enables one to examine nucleation phenomenon in these

models, if any. Moreover, the MG2 potential is successfully implemented in LAMMPS. In addition, for computation of thermal conductivity of any system using Green-Kubo method, comprising of Si, B and N the choice of MG2 empirical is a must.